

**ASSESSMENT OF OXIDATION IN CARBON FOAM**

A Dissertation

by

SEUNG MIN LEE

Submitted to the Office of Graduate Studies of  
Texas A&M University  
in partial fulfillment of the requirements for the degree of

DOCTOR OF PHILOSOPHY

May 2010

Major Subject: Mechanical Engineering

# **ASSESSMENT OF OXIDATION IN CARBON FOAM**

A Dissertation

by

SEUNG MIN LEE

Submitted to the Office of Graduate Studies of  
Texas A&M University  
in partial fulfillment of the requirements for the degree of

DOCTOR OF PHILOSOPHY

Approved by:

Chair of Committee,	Ozden O. Ochoa
Committee Members,	Terry Creasy
	Xinlin Gao
	Ramesh Talreja
Head of Department,	Dennis O'Neal

May 2010

Major Subject: Mechanical Engineering

## ABSTRACT

Assessment of Oxidation in Carbon Foam. (May 2010)

Seung Min Lee, B.S., Korea Military Academy;

M.S., Korea Advanced Institute of Science and Technology (KAIST)

Chair of Advisory Committee: Dr. Ozden O. Ochoa

Carbon foams exhibit numerous unique properties which are attractive for light weight applications such as aircraft and spacecraft as a tailorable material. Carbon foams, when exposed to air, oxidize at temperatures as low as 500-600°C. The research objectives of this study are to assess the degree of oxidation of carbon foam by experimental and computational methods and evaluate the degradation in stiffness of the bulk foam as a function of oxygen concentration profile, time and temperature. In parallel to simulation, oxidation tests are conducted to observe changes in morphology and to calculate the apparent activation energy. Degradation patterns in the carbon foam microstructure are categorized through optical microscopy (OM) images post oxidation. The influence of microstructure and temperature on the oxygen concentration profile is investigated in parametric models with varying porosity. The degradation in bulk foam stiffness is found to be strongly dependent on the temperature and non-uniform oxygen concentration profile. The overall results enhance the design of experiments for high temperature and oxidative environments, illustrating the relationship between foam microstructure and oxygen concentration in porous media.

*To my lovely wife, Seung Hee, and my sons, Jin Woo, Jin Jae*



## **ACKNOWLEDGEMENTS**

I would like to thank my advisor, Dr. Ozden O. Ochoa, who has given me guidance and encouragement in this work. I would also like to express my thanks to Dr. Terry Creasy, Dr. Xinlin Gao, and Dr. Ramesh Talreja for sharing their valuable insight as committee members. I am especially grateful for the discussion and support of my group members, classmates and ROK military officers at Texas A&M.

Finally, I would like to express my gratitude to my family's continuous encouragement and support. Without their effort and love, this would not be possible.

## TABLE OF CONTENTS

	Page
ABSTRACT .....	iii
DEDICATION .....	iv
ACKNOWLEDGEMENTS .....	v
TABLE OF CONTENTS .....	vi
LIST OF FIGURES .....	ix
LIST OF TABLES .....	xv
1. INTRODUCTION.....	1
1.1 Rationale and Objectives.....	1
1.2 Literature Review .....	3
1.2.1 Oxidation Assessment .....	3
1.2.2 Analytical Models .....	7
1.3 Overview of the Study.....	10
2. EXPERIMENTAL APPROACH AND OXIDATION PROCESS .....	12
2.1 Carbon Foam Microstructure .....	12
2.1.1 Morphological Features in a Single Cell.....	12
2.1.2 Bulk Foam Representation with Multiple Cells.....	18
2.2 Carbon Oxidation .....	20
2.2.1 Carbon Reaction Rate.....	20
2.2.2 Oxygen Mass Balance .....	23
2.3 TGA Experiments .....	24
2.3.1 Test Overview and Sample Preparation .....	24
2.3.2 Mass Loss.....	27
2.4 Furnace Exposure Test .....	30
2.4.1 Test Overview .....	30
2.4.2 Microscopy Observations Post Oxidation.....	31
2.4.2.1 Exposed Surfaces .....	31
2.4.2.2 Bottom Protected Surface.....	36
2.5 Remarks.....	40
3. COMPUTATIONAL APPROACH .....	41

	Page
3.1 Overview .....	41
3.2 Oxygen Concentration Profile: Diffusion Analysis .....	42
3.2.1 Model Description .....	42
3.2.2 Initial and Boundary Conditions .....	43
3.2.3 Time Dependent Oxygen Concentration Observation .....	45
3.3 Influence of Porosity on Oxygen Concentration Profile .....	50
3.3.1 Model Description .....	50
3.3.2 Results and Discussion .....	51
3.4 Effect of Temperature on Oxygen Concentration .....	54
3.4.1 Model Description .....	55
3.4.2 Results and Discussions .....	56
3.4.3 Evaluating Mass Loss during Oxidation .....	60
3.5 Remarks .....	69
4 EVALUATING OF CARBON FOAM MATERIAL PROPERTIES .....	70
4.1 Overview .....	70
4.2 Compressive Response of Carbon Foam .....	70
4.2.1 Problem and Model Description .....	70
4.2.2 Boundary and Loading Conditions .....	72
4.2.3 Effective Modulus .....	73
4.2.4 Impact of Cell Number on Effective Modulus .....	74
4.2.5 Impact of Foam Porosity on Effective Modulus .....	79
4.3 Thermal Conductivity of Carbon Foam Microstructure .....	80
4.3.1 Problem and Model Description .....	80
4.3.2 Element Properties and Boundary Condition .....	82
4.3.3 Evaluation of Effective Thermal Conductivity .....	83
4.3.4 Impact of Pore Conductivity on Effective Thermal Conductivity .....	84
4.4 Coupled Thermo-Mechanical Behavior .....	87
4.4.1 Problem and Model Description .....	87
4.4.2 Element Properties and Boundary Conditions .....	88
4.4.3 Coefficient of Thermal Expansion (free expansion at isothermal condition) .....	89
4.4.4 Isothermal with Displacement .....	91
4.5 Remarks .....	96
5. CARBON FOAM REPRESENTATIVES: OXIDATION EFFECT .....	98
5.1 Overview .....	98
5.2 Evaluation of Oxygen Concentration Profile and Porosity .....	98
5.2.1 Oxygen Concentration Profiles in Bulk Foam .....	98
5.2.2 Change of Foam Porosity Due to Oxygen Concentration .....	103

	Page
5.3 Time Dependent Compression Response of Bulk Foam .....	105
5.3.1 Problem and Model Description .....	105
5.3.2 Mesh Creation and Time Dependent Properties.....	106
5.3.3 Boundary and Loading Conditions .....	108
5.3.4 Reaction Force and Stress Distribution .....	109
5.3.5 Evaluation of Degradation in Bulk Stiffness.....	123
5.4 Remarks.....	125
6. CONCLUSIONS.....	127
REFERENCES.....	129
APPENDIX A BINARY DIFFUSION COEFFICIENT .....	134
APPENDIX B UMAT CODE (600°C) .....	136
VITA .....	141

## LIST OF FIGURES

FIGURE	Page
2.1 Morphological features of carbon foam (a) SEM image and (b) Micro-CT X-ray scan image [2, 37], and (c) single cell of idealized tetrakaidecahedron .....	13
2.2 The ligament thickness variation along to ligament axis: (a) ligament configuration, (b) effective thickness .....	16
2.3 Porosity and relative density: (a) vs. ligament thickness and (b) vs. % relative density .....	18
2.4 Multiple cell representation: (a) single cell and (b) multiple cells with packing of single cells (3 x 3 x 3) .....	19
2.5 Schematic of mass balance of oxygen at an infinitesimal interface.....	23
2.6 TGA test equipment (SDT Q 600) .....	25
2.7 Percent mass loss as a function of time at three different temperatures (600, 700, 800 °C) .....	27
2.8 Plot of normalized mass rate ( $\overline{\dot{m}}''$ ) vs. temperature .....	28
2.9 Photograph of the furnace (Cress Mfg. Co.) used in the oxidation test .....	31
2.10 Representative images at S1 surface: (a) before exposure and (b) after 100 minutes of exposure .....	32
2.11 Microscopical investigation of oxidation process of carbon fibers: (a) weight loss 31 % and (b) weight loss of 72 %.....	33
2.12 Representative OM images of “ligament thickness reduction and disconnection”: (a) at S1 surface, (b) at S1 surface, and (c) at S2 surface .....	34
2.13 Representative OM images of “pore merge”: (a) at S4 surface and (b) S2 surface .....	35
2.14 Representative OM images of “pore creation”: (a) at S1 surface and (b) S4 surface .....	36

FIGURE		Page
2.15	Low magnification OM images sites in contact with furnace bottom: (a) before oxidation and (b) post oxidation .....	38
2.16	High magnification OM images sites in contact with furnace bottom: (a) before oxidation and (b) post oxidation .....	39
3.1	Illustration of quarter foam model .....	42
3.2	Schematic of 10-node quadratic tetrahedron element .....	43
3.3	Boundary conditions .....	44
3.4	Contour plot of oxygen concentration as a function of time .....	46
3.5	The process of three-dimensional plot of oxygen concentration: (a) layer description, (b) original plot from FEA analysis (c) constructed image about xy plane, and (d) full 3D profile .....	47
3.6	Representatives of oxygen concentration profile throughout foam with respect to time increase: (a) 16.7 min, (b) 266.7 min, and (c) 300 min at three different locations, $y/H=0.5, 0.7$ , and $0.9$ .....	49
3.7	Three different foam representations for a quarter model: (a) 83% porosity, (b) 90% porosity, and (c) 95% porosity .....	50
3.8	Contour plot of oxygen concentration of section view at three different foam porosities: (a) 83% porosity, (b) 90% porosity, and (c) 95% porosity. ....	52
3.9	Illustration of coordinates and normalized layer description .....	53
3.10	Comparison of oxygen concentration at normalized layer 0.5, 0.7, and 0.9 after 16.7 minutes exposure: (a) 83% porosity, (b) 90% porosity, and (c) 95% porosity .....	54
3.11	Carbon reaction rate vs. temperature.....	55

FIGURE	Page
3.12 Contour plot of oxygen concentration with increase of exposure time: (a) at 600°C, (b) at 700°C, and (c) at 800°C .....	57
3.13 Comparison of oxygen concentration profile at normalized layer (y/H) of 0.5 with the increase of exposure time: (a) 3.3 minutes (b) 23.3 minutes, and (c) 46.7 minutes .....	58
3.14 Comparison of reaction rate at normalized layer 0.5 as a function of time: (a) 3.3 minutes (b) 23.3 minutes, and (c) 46.7 minutes.....	59
3.15 Ligament geometry and cross-section definition .....	60
3.16 Oxygen concentration vs. time: (a) description for location, (b) nodal oxygen concentrations of single cell at x/L: 0.4~0.8 and z/L: 0~0.4 (600oC) at y=0.....	62
3.17 Comparison of change in ligament thickness at three different zones of outer, middle, and inner zone of the cell. Note that the location (x/L) of outer, middle and inner zones are 0.0~0.4, 0.4~0.8, and 0.8~1, respectively .....	63
3.18 Comparison of TGA result to calculation with Equation 3.12 (600°C) .....	64
3.19 Plot of FEA results (dot data) and exponential expression (red line) of oxygen concentration profile (temperature: 700°C) of foam: (a) at outer (x/L: 0 ~0.4), (b) at middle(x/L: 0.4 ~0.8), and (c) at inner zone(x/L: 0.8 ~1).....	65
3.20 Plot of FEA results (dot data) and exponential expression (red line) of oxygen concentration profile (temperature: 800°C) of foam: (a) at outer (x/L: 0 ~0.4), (b) at middle(x/L: 0.4 ~0.8), and (c) at inner zone(x/L: 0.8 ~1).....	66
3.21 Ligament thickness change at three different zones: (a) 700 °C, (b) 800 °C .....	68
3.22 Comparison of TGA results to calculation with Equation 3.12 at 700°C and 800 °C. ....	68
4.1 Representations of foam models: (a) 3 x 3 x 3 (b) 5 x 5 x 3, and (c) 7 x 7 x 3.....	71

FIGURE	Page
4.2 Schematic of displacement boundary conditions. Three displacements of -0.042 mm and zero are applied on +y and -y surfaces, respectively ...	72
4.3 Illustration of periodic boundary condition on single cell. The nodes applied to periodic boundary conditions are highlighted by yellow color .....	73
4.4 Impact of single cell number on effective modulus .....	75
4.5 Contour plot of the x- and z- displacement output fields: (a) single cell, (b) 7 x 7 cell, and (c) single cell with periodic boundary condition .....	76
4.6 Plot of lateral strain ( $\epsilon_{xx}$ ) as a function of number of cells .....	77
4.7 Contour plot of stress distributions (MPa) of single cell with periodic boundary condition: (a) $\sigma_{yy}$ and (b) $\sigma_{xx}$ .....	78
4.8 Effective modulus vs. relative density .....	80
4.9 Illustration of foam model composed 5 x 5 x 3 cells .....	82
4.10 Illustration of temperature boundary conditions on foam model .....	83
4.11 Contour plot of temperature distribution and heat flux: (a) w/o air conduction, (b) with air conduction .....	86
4.12 Contour plot of temperature gradient and heat flux in single cell at middle layer: (a) w/o air conduction and (b) with air conduction .....	87
4.13 Illustration of bulk foam model (5 x 5 x 3) .....	88
4.14 Temperature and boundary conditions .....	89
4.15 Contour plot of the x- and z- expansion (mm). Note that the expanded values in the x- and z- directions are approximately same: (a) $\Delta T=575K$ , (b) $\Delta T=675K$ , and (c) $\Delta T=775K$ .....	90
4.16 Comparison of deformation in x-direction at the temperature of 600°C: (a) free expansion and (b) boundary condition on +y-surface ( $u_y=0$ ) .....	91



FIGURE	Page
4.17 Contour plots of $\sigma_{yy}$ stress distribution (MPa): (a) $\Delta T = 575K$ , (b) $\Delta T = 675K$ , and (c) $\Delta T = 775K$ .....	93
4.18 Contour plots of $\sigma_{xx}$ stress distribution (MPa): (a) $\Delta T = 575K$ , (b) $\Delta T = 675K$ , and (c) $\Delta T = 775K$ .....	94
4.19 Contour plots of nodal reaction force ( $RF_2$ ): (a) $\Delta T = 575K$ , (b) $\Delta T = 675K$ , and (c) $\Delta T = 775K$ .....	96
5.1 Model schematic .....	100
5.2 Contour plot of oxygen concentration distribution at 50 minutes elapse at $600^\circ C$ .....	101
5.3 Plot of time history of oxygen concentration profile: (a) contour plot of oxygen concentration, (b) nodal concentration distribution of cell at the location of $x/L1=0\sim0.2$ , (c) average oxygen concentration of cell at the location of $x/L1=0\sim0.2$ (d) average oxygen concentrations at each location.....	102
5.4 Plot of change in pore volume fraction of single cell as a function of time .....	105
5.5 Model description of idealized foam.....	106
5.6 Comparison of FEA results to Equation 5.4 with $k_I$ of 1.52 .....	107
5.7 Illustration of boundary conditions .....	108
5.8 Displacement output fields: (a) $u_y$ , (b) $u_x$ , and $u_z$ .....	109
5.9 Normal stress (MPa) contours in the y-direction as a function of exposure time .....	111
5.10 Plot of normal stress in y-direction of each normalized location ( $x/L$ ) at $z=0$ as a function of time. The plot with marks is the stress vs. time curve with neglecting thermal expansion at the temperature of $600^\circ C$ .....	113
5.11 Representatives of 3-D plot of resultant nodal reaction force at the temperature of $600^\circ C$ : (a) after 11.2 minutes, (b) after 39.2 minutes, (c) after 218.3 minutes, and (d) after 318.3 minutes .....	115

FIGURE		Page
5.12	Average oxygen concentration profiles of cells as a function of time (700°C) .....	116
5.13	Comparison of normal stress (MPa) in the y-direction as a function of time. left figure at 600°C and right figure at 700°C: (a) initial, (b) time 8.5 minutes, (c), time 17.5 minute, (c) 34.2 minutes, (d) 44.6 minutes, and (f) 69.2 minutes .....	118
5.14	Plot of normal stress in y-direction of each normalized location (x/L) at z=0 as a function of time. Dash red line represents the time of degradation initiation at the center cell at 700°C. ....	120
5.15	Representatives of 3-D plot of nodal reaction force as a function of time: right figure is 600°C and left figure is 700°C .....	122
5.16	Plot of variation in normalized effective modulus as a function of time ...	124
5.17	Change in normalized stiffness vs. time at 600 and 700°C as a function of time .....	125

## LIST OF TABLES

TABLE	Page
2.1 The porosity representations of cell structures [31] .....	15
2.2 Product data sheet [45] .....	25
2.3 Dimension and initial mass of TGA samples .....	26
2.4 Calculated activation energy at each mass loss % .....	29
2.5 Sample dimension and mass .....	30
3.1 Temperature dependent material properties [44, 47] .....	56
4.1 Total number of single cells and ligaments.....	71
4.2 Total reaction force in different number of single cell.....	74
4.3 Effective thermal conductivities with and w/o air conductivity, $W/m-K$ ...	84
5.1 List of total reaction forces and decrease % in total reaction forces as a function of time for bulk foam (600°C) .....	116
5.2 Total reaction forces for temperature of 600 and 700°C at each time exposure .....	123

## 1. INTRODUCTION

### 1.1. Rationale and Objectives

Even though polymers foam are most common, current technology offers many opportunities to fabricate foams using metals, ceramics, and glasses [1-2]. Carbon foams were first developed in the 1960's as reticulated vitreous carbon (RVC) foam, which is an open cell foam material composed of vitreous carbon [3]. RVC foams are produced by carbonizing thermoset polymer foams through a simple heat treatment. They have been used as the template for many of the metal and ceramic foams currently used in industry. Significant research was conducted on using different precursors in an attempt to modify properties and reduce costs. In 1990's, mesophase pitch-derived graphite foams were pioneered at the Wright Patterson Air Force Base Materials Laboratories, to reduce expensive 3-D woven fiber preforms in polymer composites and as potential replacement for the honeycomb [4, 5]. Their work was centered on developing lightweight and high specific strength carbon foams.

In addition, researchers at West Virginia University developed a method that used coal as a precursor for high strength foams with thermal insulation properties to reduce manufacturing costs [6, 7]. Later, Klett, J. at the Oak Ridge National Laboratory (ORNL) reported that the first graphite foams with high bulk thermal conductivities (greater than 40 W/m-K) were made by a heat treatment and changing of precursors. Recently, conductivities up to 180 W/m-K have been measured [8, 9].

---

This dissertation follows the style of *Journal of Composite Materials*.

Carbon foam with thermal conductivity of a weight ratio of greater than 200 (compared to 45 for copper), presents a unique opportunity to change the approach to solving many heat transfer problems [10]. Carbon foam was shown to exhibit numerous unique properties that make it an attractive material for use in many industrial, commercial and military fields. Carbon foam is generally stiffer than other foams of the same density. For instance, although carbon foam stiffness is in the range of engineering polymers such as polyethylene, its low density leads to a significantly higher specific stiffness [11].

Beside these properties, one of the unique features is the tailorability of carbon foam properties. The parameters during the production process, such as temperature, pressure, and precursor types, affect the topology and material properties. For example, heat treatment on the carbon foam altered its thermal conductivity. As the heat treatment temperature increased, more order was developed in the carbon molecular structure, increasing the thermal conductivity [3]. Precursors such as coal tar, petroleum pitch, and synthetic mesophase pitch can also affect the mechanical properties of carbon foam allowing them to be tailored to meet specific design specifications.

Beyond these structural and thermal features, other applications take advantage of the topological characteristics of carbon foam. The open cell nature makes it a candidate for filtration and catalyst beds, as well as for noise reduction applications [11]. Other research is focusing on EMI (electro-magnetic interference) and radar-selective shield applications in stealthy aircraft [12]. In addition, carbon foam is under investigation in many biomedical applications such as dentistry and orthopedics [13].

The research objectives of this dissertation were *to assess the oxidation degree of*

*carbon foams by experimental/computational approaches and evaluate the degradation in effective modulus of bulk foam coupled with oxygen concentration distribution as a function of time and temperature.* In pursuit of this goal, the following research tasks were undertaken:

- Exposure tests to investigate the degree of oxidation and to identify degradation patterns.
- Computational models to understand the influence of microstructures and temperature on carbon foam oxidation.
- Evaluate the effective moduli of bulk foam in the coupled thermo-mechanical field as a function of foam porosity.
- Evaluation of degradation in effective modulus of bulk foam coupled with oxidation rate as a function of time and temperature for a set porosity.

## **1.2. Literature Review**

### **1.2.1. Oxidation Assessment**

It is well known that carbon-based materials have been studied much for thermomechanical applications in aerospace [2, 11]. They offer excellent thermal stability coupled with high mechanical performance in an inert atmosphere or in a vacuum [14, 15]. Nevertheless, like other carbon materials, when exposed to air, carbon materials oxidize at temperatures as low as 500-600°C leading to degradation of its properties [16-18]. Thus, understanding the oxidation behavior of carbon remains an active area of research, especially improving oxidation resistance and broadening their

applications as high temperature structural materials in an oxidizing environment [19-21].

Carbon foam is a likely candidate to be used as a core in carbon/carbon sandwich composites. Especially in the aerospace industry, sandwich structures are well-known and widely adopted because of their high specific stiffness, and low thermal expansion. A sandwich structure typically consists of two thin and stiff skins separated by a thick core material, which increases the second moment of inertia to achieve a high bending stiffness. From the thermal standpoint, the air craft/space craft must be able to undergo the high temperature exposure during the atmosphere penetration into space or upon its return. When exposed to an oxidizing atmosphere at high temperatures, both carbon-carbon skin and foam may experience degradation of its original properties [22].

Generally the oxidation of carbon exhibits three different regimes [23]. At a low temperature (600-800°C), it is controlled by a chemical reaction. At an intermediate temperature (700-900°C), it is controlled by a chemical reaction and gaseous diffusion. At high temperatures (greater than 900°C), it is controlled by gaseous diffusion. Literature data on carbon oxidation has shown that experimental values of reactivities under similar conditions may differ by the factors; the causes of the discrepancy are well known [24]: catalytic effects, different thermal treatments of a same material, experiment variations (gas velocity, quality of air). Consequently, the reactivity measurements must be conducted with special attention focused on the experimental conditions, such as the air flow rate, the heating rate, and the gas control during heating.

The oxidation of carbon resulted in the formation of gaseous carbon oxides at a

high temperature in the atmospheric condition [21, 23-25]. Thus, this gasification reaction causes weight loss and geometrical change. Numerous studies have been undertaken to assess the carbon oxidation by measuring mass loss and microscopy investigation of morphological change post oxidation [14-29].

The thermal gravimetric analysis (TGA) test has been accepted as a useful technique to study the kinetics of solid state thermal reactions such as dehydration and decomposition of inorganic material, oxidation of carbon materials. TGA is performed on samples to measure mass in relation to change in temperature [25]. In addition, the apparent kinetic parameters can be determined by using TGA test results. For example, Weiming et al. investigated 2D-C/C composite by thermogravimetric analysis in the temperature range of 745-900°C and calculated the activation energy from TGA results [14]. At lower temperatures (745-800°C), the oxidation is only controlled by the surface reaction between carbon and oxygen, and the corresponding activation energy is about 195-208kJ/mol. They also showed that carbon matrix is oxidized much more rapidly than the carbon fibers. As a result, the fibers exhibited reduction of diameter, their ends became sharp. At a higher temperature (850-900°C), the chemical reaction rate is higher, and the interior of composite is filled with product (CO, CO<sub>2</sub>). The oxidation was controlled by the chemical reaction and gaseous diffusion. Thus, oxygen must diffuse through the gas layer to react with carbon, and the transfer of reactant and product plays an important role for oxidation.

These heterogeneous reaction (solid + gas → gas) caused volumetric changes in solid carbon and resulted in degradation of its origin properties [26, 27]. F. Lamouroux



[28] reported the oxidation effects on tensile properties of 2D woven C/SiC composites between 700°C and 1400°C for durations corresponding to a maximum of 6% relative mass loss. According to their experimental results, oxidation mechanisms have been correlated with three main degradation modes of carbon reinforcement. First, at a low temperature ( $<800^{\circ}\text{C}$ ), uniform oxidation degradation resulted in the simultaneous degradation of the carbon fibers and interface all over the composite material. Non-uniform degradation at an intermediate temperature ( $800 < T < 1100^{\circ}\text{C}$ ) results in a high consumption of oxygen by the first carbon plies. Thus, a non-uniform degradation mode led to the premature rupture of the more intensively degraded at first plies upon loading. This sudden rupture of the first plies induced an overloading effect on the inner plies which caused a break. Superficial degradation occurring at high temperatures ( $> 1100^{\circ}\text{C}$ ) induces the composite premature rupture by a combined notch/overloading effect from the outer fiber tows.

Lachaud J. et al.[29] reported on the mean pore effect on oxidation of carbon fiber bundle to study intrinsic oxidation reactivity of C/C composites. Here, several samples, fiber bundle and matrix, were tested at a single temperature (898K). The oxygen concentration profile throughout the fiber bundle was calculated by applying oxygen consumption rate at fiber surface without considering the transient effect. According to their results, the carbon reaction rate was strongly correlated to the temperature and the porosity. When mean pore size increased, total amount of inlet oxygen concentration flux increased because the total flux of oxygen was proportional to pore size at the exposed surface. As a result, oxygen consumption rates at the carbon

surface also increased. In this scenario, the outlet oxygen concentration also increased because the total amount of inlet of oxygen, which was affected by diffusion coefficient of oxygen in air was much larger than the consumption rate of oxygen at carbon surface. However, how far oxygen can penetrate was dependent on not only the mean pore size but also the oxygen consumption rate at the carbon surface. Although there was difference in reaction rate between carbon fiber bundle and carbon foam, their finding in the oxygen concentration profile in the fiber bundle and evaluation approaches were valuable in helping to understand the oxidation phenomena in foam.

#### 1.2.2. Analytical Models

In addition to experiments, computational models have been utilized to assess carbon oxidation. Most work has focused on the mass loss of carbon and was not extended to evaluate property degradation during the oxidation process. As mentioned earlier, mass loss by oxidation has a direct correlation with volumetric change in carbon material, thus its original properties can be affected. The carbon reaction rate is a function of temperature and oxygen concentration [27, 29]. For example, F. Larmouroux et al [28] showed the effect of the oxygen content on morphological changes. Decreasing the oxygen content modified the distribution of the degraded zones mainly through a decrease of reactivity of the carbon phases. Therefore, notch-like attack of the carbon fibers appear to be less extended in air than in pure oxygen since the decrease of the oxygen content lowers the oxygen gradient and consequently the oxygen diffusion flux through the microcracks.

In the pursuit of assessing and predicting oxidation, several analytical models without considering the transient effect but with assumed linear oxygen concentration profile have been reported [27-30]. Jean Lachaud [27] developed analytical models to predict the composite behavior of two different scales during oxidation: microscopic (fiber and matrix) and macroscopic scale (composite). The physical basis is a general model for receding surfaces under a gasification process coupled to mass transfer. The models were solved analytically in steady state conditions considering a 1-D mass transfer perpendicular to the overall surface. Assuming a vertical concentration gradient and steady state, oxidation velocity was a function of diffusion velocity. It was found that oxidation behavior was divided into two regimes. The diffusion velocity was higher than the reactivity; the regime was reaction-limited. Hence, the concentration of oxygen was equal to the exposure surface in the full fluid phase. In the converse case, the regime was diffusion-limited. Oxidation rate was controlled by the oxygen concentration profile.

In addition, in order to identify the intrinsic reaction rates of fiber, the fiber bundles were modeled considering diffusion of the oxidant throughout the mean pore of fiber bundle in combination with the reaction on the fiber surface [29]. It was found that the intrinsic geometrical oxidation rate of fibers was as a function of the mean pore size and of the effective oxidation rate of the bundle, which was strongly related to temperature.

As noted, significant work was on the oxidation of C/C composite, offering insight to oxidation mechanisms. However, carbon foam has not been studied and reported extensively. The oxidation in carbon foam will be dependent on its micro-

structure. Analytical models of cellular materials provide a good starting point. The simultaneous oxidation which depends on the oxygen concentration can be expected at individual ligaments leading to reduction of its cross section. Though most of work does not involve degradation coupled with thermal oxidation, research showed the relationships between effective properties and parameters: micro structure, foam porosity, ligament shape.

Gibson and Ashby [31] assumed a cubic single cell of struts where the cross section was square and constant along the ligament length to represent foam microstructure. Most important structural characteristic of foam was its relative density,  $\bar{\rho} = \rho^* / \rho_s$  (or porosity,  $\Phi = 1 - \rho^* / \rho_s$ ). In order to remove the geometric constants, the second moment inertia and the foam porosity were assumed proportional to the ligament dimension relationship. By fitting experimental results, they reported that an effective modulus was proportional to the porosity.

In the pursuit to evaluate effective material properties, several finite element analysis (FEA) models, with a different single cell configuration, have been undertaken [32-36]. Christensen focused on finding the effective property relationships in both open and closed cell foams [32]. In the case of open cell foams, the effective Poisson's ratio was found to be independent of the material property while the effective modulus was expressed as a linear function of the relative foam density. Warren and Kraynik [33, 34] used a polyhedral single cell known as a tetrakaidecahedron. By assuming the constant cross section struts, equilibrium analyses were performed to evaluate forces, moments and displacements at the strut midpoints with several different cross sectional shapes.

This model gave good estimates of the effective modulus, but their results showed a constant a Poisson's ratio, which was higher than the value suggested by Gibson and Ashby's experimental results. Similarly, the compressive modulus was predicted using the Kelvin model where the energy method was employed in the formulation [35, 36]. The strut properties were assumed to be isotropic with a constant cross sectional area along the length. They used Castigliano's second theorem to calculate deformation of each ligament. Further elastic behaviors of foam were investigated with three different loading modes: loading on the square plane, hexagon plane and vertices of Kelvin model.

Sarzynski M.D. investigated the mechanical and thermal response in the multi-scale model of carbon foam (ligament, single pore, multiple pore scale), where images of the carbon foam morphology were obtained from high resolution micro-CT X-ray tomography [11]. The anisotropic properties were assigned to individual ligaments in the finite element model to study the mechanical and thermal responses. In addition, coating layers were included in the model to assess the impact on multi-field responses.

### 1.3. Overview of the Study

In pursuit of the research objective stated in Section 1.1, the degree of carbon foam oxidation was studied experimentally and computationally as a function of time and temperature. In Section 2, the oxidation mechanism and thermogravimetric analyzer test (TGA) are described. Three different temperatures were introduced to investigate temperature effect on the oxidation of carbon foam. Those results were used to determine the apparent activation energy of the sample and the mass transfer coefficient

for the computational model. In addition, morphological investigations were undertaken with the help of microscopy images to study the degradation pattern post oxidation.

The computational models developed to assess the oxidation of carbon foam are presented in Section 3. Carbon foam models with different porosity, 95, 90, and 83 % were employed to evaluate the effect of the microstructure on the oxygen concentration profile and on the oxidation rate and as a function of temperature.

Section 4 introduces the finite element (FE) models utilized to study the influence of foam microstructure under compressive mechanical and thermal loads. The effect of utilizing different number of foam cells and porosity values were studied to predict an effective modulus and determine the overall size of a representative volume element (RVE) to simulate the bulk foam behavior. The pore and ligament volumes were generated to investigate the influence of pore conductivity on the distribution of temperature and heat flux, as well as effective thermal conductivity. In addition, the relationship between foam porosity and the effective modulus in coupled thermal-mechanical field was described at the temperature of 600, 700, and 800°C.

The degradation of stiffness of the carbon foam due to oxidation was explained in Section 5. The activation energy of carbon foam as calculated in section 2 as well as the oxidation models developed in Section 3 were used to represent the oxidation rate as a function of exposure of time. The cell porosity-exposure time and the effective modulus-foam porosity relationships developed in Section 3 and 4 respectively were utilized to express the time-dependent constitutive response of bulk foam as a function of time and temperature.

## 2. EXPERIMENTAL APPROACH AND OXIDATION PROCESS

### 2.1. Carbon Foam Microstructure

#### 2.1.1. Morphological Features in a Single Cell

The most important structural characteristic of a cellular solid is its relative density,  $\rho^*/\rho_s$  (the ratio of the density,  $\rho^*$  of the foam to that of the solid phases,  $\rho_s$ ) since bulk properties are directly proportional to it [31-36]. The fraction of pore space can be expressed as  $\Phi = 1 - \rho^*/\rho_s$ . In order to achieve the objectives of this present research, it is important to understand the microstructure of the foam presented in Figure 2.1. Based on the minimum surface energy during the foaming process, the microstructure takes on a tetrakaidecahedral configuration where the ligaments are oriented approximately  $109^\circ$  to each other [2]. Tetrakaidecahedron has 8 hexagonal faces and 6 square faces comprised of 36 ligaments and 24 vertices in a single cell [31].

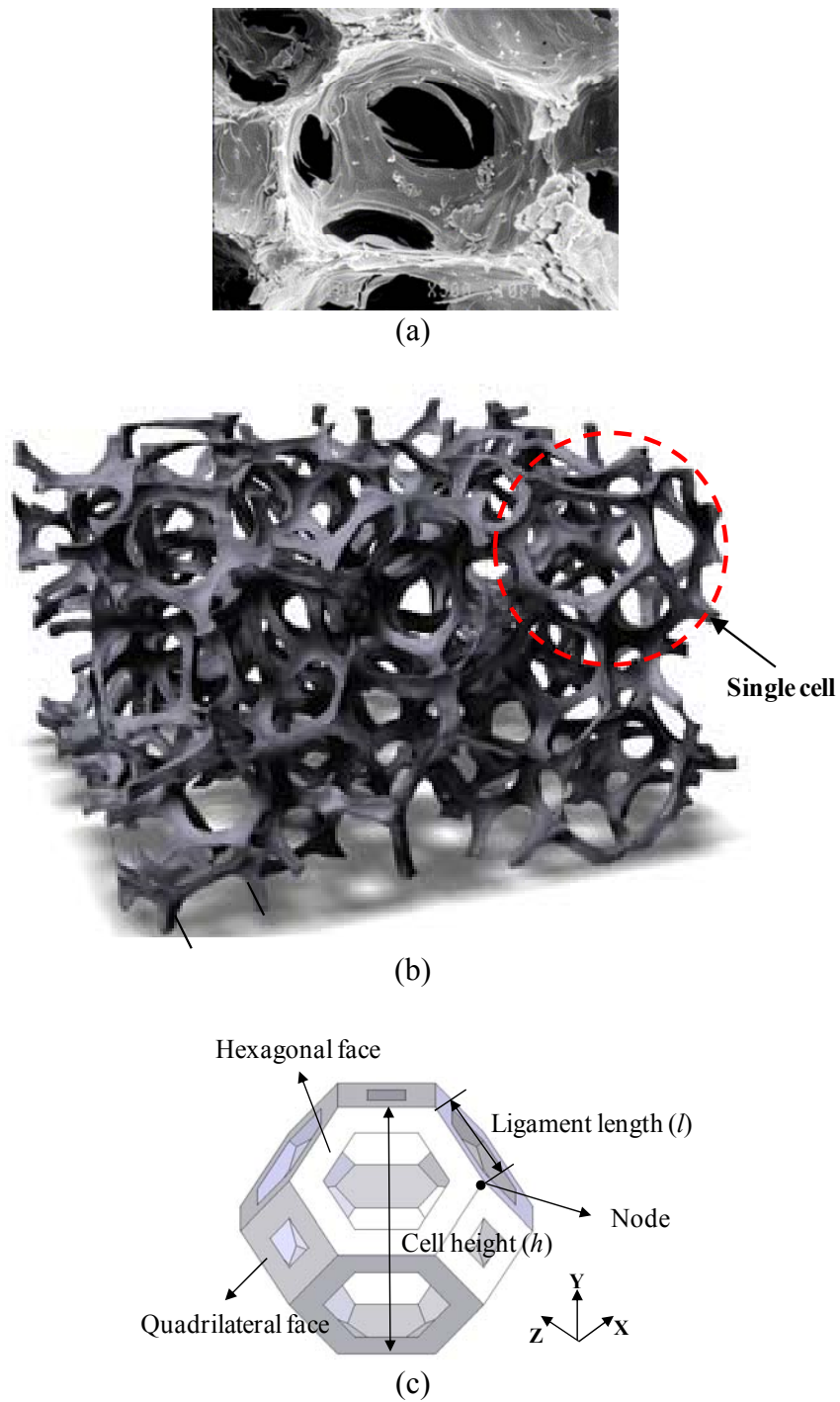


Figure 2. 1. Morphological features of carbon foam (a) SEM image, (b) Micro-CT X-ray scan image [2, 37], and (c) single cell of idealized tetrakaidecahedron. (Reprinted with Permission of Elsevier.)



In view of the complexity of the carbon foam microstructure, it is advantageous to consider a simplified representation such as the single cell of Figure 2.1 (c). As depicted in Figure 2.1, the foam porosity depends on the cell structure. Gibson and Ashby suggested approximate relationships to introduce ligament thickness and porosity in open-cell foams [9], if the ligament length is  $l$  and the ligament thickness is  $a$ , as follows;

$$1 - \frac{\rho^*}{\rho_s} = 1 - C_l \left( \frac{a}{l} \right)^2 \quad (2.1)$$

In this relationship, the porosity is calculated in terms of ligament thickness ( $t$ ) and ligament length ( $l$ ) and has a single numerical constant  $C_l$ . Typical cell configurations and corresponding porosity expressions are listed in Table 2.1 [9].

Warren W.E. and K. Li et al. suggested the porosity representation below for ligaments with triangular cross sections [33-36],

$$1 - \frac{\rho^*}{\rho_s} = 1 - \frac{3A}{2\sqrt{2}l^2} \quad (2.2)$$

\*  $a$  and  $l$  is the ligament thickness and the length, respectively.  $A_r$  is the aspect ratio of  $h$  (*height*) and  $l$ .

Table 2. 1. The porosity representations of cell structures [31]

Cell structure	Porosity equation
Triangular prisms	$1 - \frac{2}{\sqrt{3}} \frac{a^2}{l^2} \left( 1 + \frac{3}{A_r} \right)$
Square prisms	$1 - \frac{a^2}{l^2} \left( 1 + \frac{2}{A_r} \right)$
Hexagonal prisms	$1 - \frac{4}{3\sqrt{4}} \frac{a^2}{l^2} \left( 1 + \frac{3}{2A_r} \right)$
Rhombic dodecahedra	$1 - 2.87 \frac{a^2}{l^2}$
<b>Tetrakaidecahedra</b>	$1 - 1.06 \frac{a^2}{l^2}$

The shortcomings of equations (2.1) and (2.2) are that porosity is calculated neglecting the overlapping volume of the ligament at nodes. Therefore, it is necessary to drive accurate expression for porosity in a single cell. Basically the total volume of a single cell has the following simple relationship,

$$V = A_{effective} \times l_{ligament} \times N_{ligament} \quad (2.3)$$

where  $A_{effective}$  is the effective cross section area of the ligament,  $l$  and  $N$  are the ligament length and number of ligament in a single cell, respectively. As shown in Figure 2.2, the effective cross section area of the ligament can be expressed as follows, when an equilateral triangle cross section is assumed.

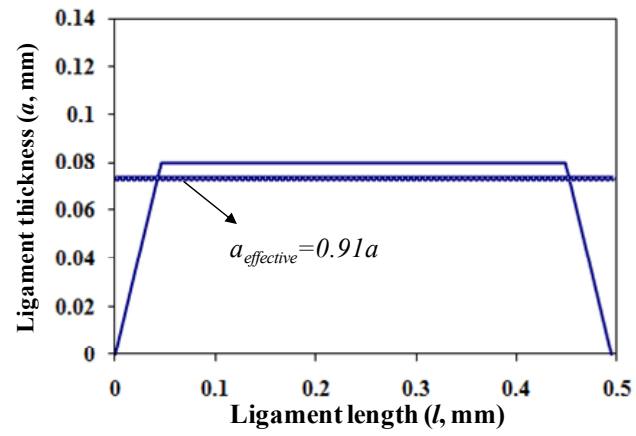
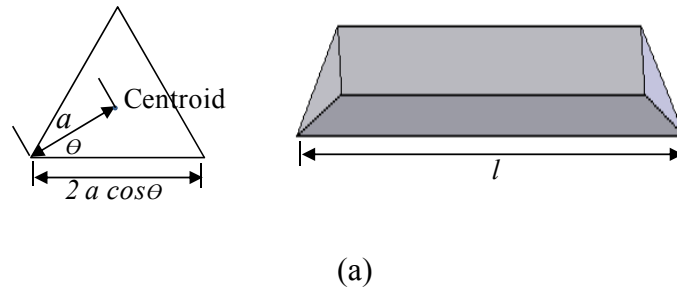


Figure 2. 2. The ligament thickness variation along to ligament axis: (a) ligament configuration, (b) effective thickness.

The calculated effective ligament thickness ( $a_{effective}$ ) is 91% of the original ligament thickness ( $a$ ). Substituting effective ligament thickness in Equation 2.3, the total volume of ligaments in a single cell can be expressed as follows,

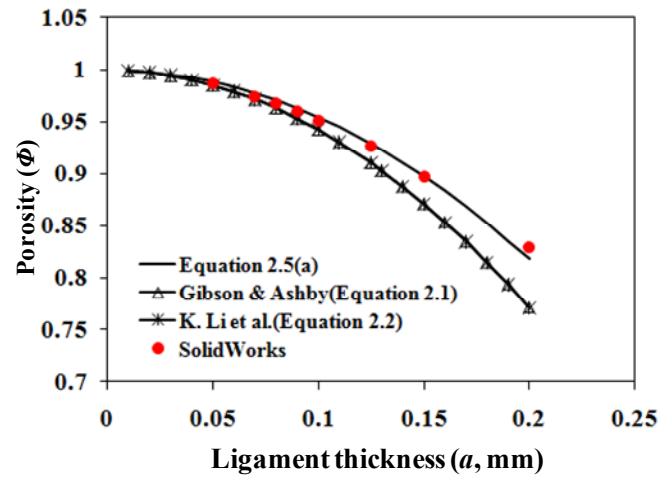
$$V_l = (a_{effective})^2 \sin\theta \cos\theta l_{ligament} N_{ligament} \quad (2.4)$$

The porosity of single cell (or relative density) can be expressed as follow,

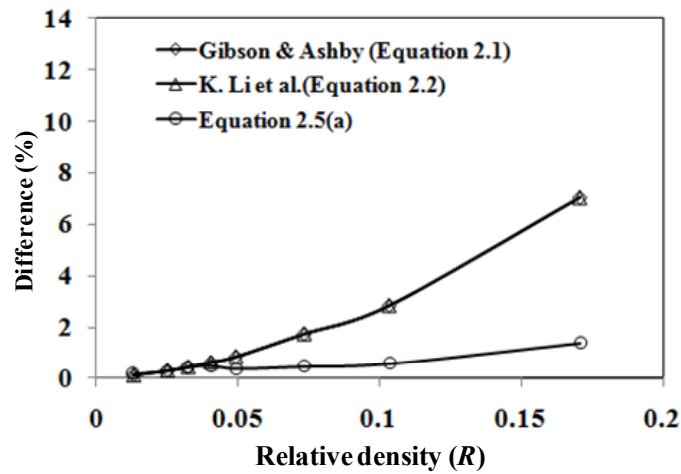
$$\Phi = 1 - \frac{V_{ligaments}}{V_{cell}} = 1 - \frac{(0.91a)^2 \times \sin(\theta) \cos(\theta) \times l \times N_{ligament}}{V_{cell}} \quad (2.5a)$$

$$R = 1 - \Phi = \frac{(0.91a)^2 \times \sin(\theta) \cos(\theta) \times l \times N_{ligament}}{V_{cell}} \quad (2.5b)$$

Note that the red points in Figure 2.3 (a) are the values calculated by SolidWorks software from the image, which has an algorithm for volume and surface area measurements. For example, with the ligament thickness ( $a$ ) of 0.08 mm and length ( $l$ ) of 0.5 mm, the total volume of ligaments in the idealized single cell of Figure 2.1(c) from SolidWorks is 0.06754 mm<sup>3</sup>. With this ligament volume and cell volume ( $V_{cell}$ ) of 1.372 mm<sup>3</sup>, the porosity ( $\Phi$ ) is calculated to be 0.95077. The porosity calculated with Equation 2.5 (a) is 0.9544. Although other models from the literature [34, 35] show a large difference when the relative density increases (or porosity decreases), the result from Equation 2.5a matches well with 0.5% difference for all the porosity level seen in Figure 2.3 (b).



(a)



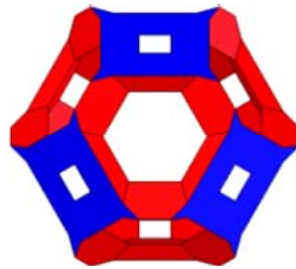
(b)

Figure 2. 3. Porosity and relative density: (a) vs. ligament thickness and (b) vs. % relative density.

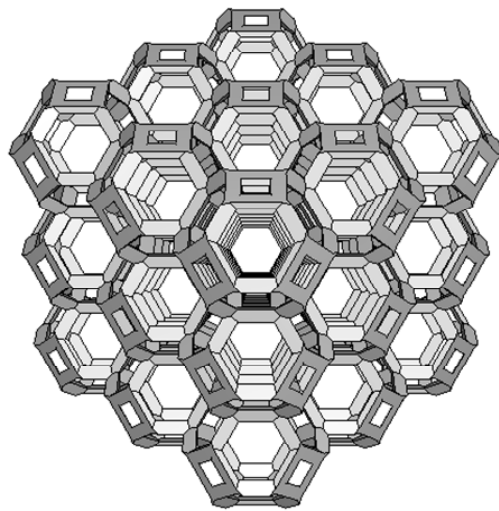
### 2.1.2. Bulk Foam Representation with Multiple Cells

The carbon foam microstructure is assumed to be comprised of periodic tetrakaidecahedra single cells, as mentioned before in the literature [31-36]. The tetrakaidecahedra cell, formally known as the Kelvin cell, consists of 36 ligaments

arranged in 6 planar quadrilateral faces and 8 hexagonal faces as illustrated in Figure 2.4. In the single cell shown in Figure 2.4 (a), the ligaments highlighted by blue color are shared with the adjacent cells, where only a half cross section is modeled. For example, 3 x 3 x 3 configuration of Figure 2.4 (b) is created by assembling of 27 single cells.



(a)



(b)

Figure 2. 4. Multiple cell representation: (a) single cell and (b) multiple cells with packing of single cells (3 x 3 x 3).

## 2.2. Carbon Oxidation

### 2.2.1. Carbon Reaction Rate

The reaction rate is dependent on the chemical reactions that take place during oxidation. The effective diffusion coefficients of the gaseous products will be different, due to their transport phenomena of chemical species by a flowing gas (Stefan flow). Ecekl et al. [38] have reported that the deviation caused by the two systems,  $C-CO_2$  and  $C-CO$ , is limited to about 5%. Therefore in this study only oxygen is considered as the reactant with carbon. The oxidation of carbon results in the formation of gaseous carbon dioxide as,



Based on this chemical reaction mode, the carbon reaction rate is expressed as [30, 39, 40],

$$\dot{m}_C'' = k(T)(MW_C)[O_2] \quad (2.7)$$

where

$\dot{m}_C''$ : Carbon reaction rate (kg/m<sup>2</sup>-sec)

$k(T)$ : Kinetic reaction rate (m/s)

$MW_C$ : Molecular weight of carbon (kg/mol)

$[O_2]$ : Molar concentration of oxygen (mol/m<sup>3</sup>)

The molar concentration is expressed as fraction of oxygen by utilizing the ideal gas law [39].  $R$  is gas constant ( $\text{m}^3\text{-Pa/K-mol}$ ),  $T$  is absolute temperature (K),  $C_{O_2}$  is oxygen concentration

$$[O_2] = \frac{MW_{mix}}{MW_{O_2}} \frac{P}{RT} C_{O_2} \quad (2.8)$$

By substituting Equation 2.8 into 2.7, the carbon reaction rate can be expressed as,

$$\dot{m}_C'' = \frac{MW_C MW_{mix}}{MW_{O_2}} \frac{P}{RT} k(T) C_{O_2} \quad (2.9)$$

where

$\dot{m}_C''$ : Carbon reaction rate ( $\text{kg/m}^2\text{-sec}$ )

$MW$ : Molecular weight species ( $\text{kg/mol}$ )

$MW_{mix}$ :  $0.79MW_{N_2} + 0.21MW_{O_2}$  ( $\text{kg/mol}$ )

$P$ : Pressure (Pa)

$R$ : Gas constant ( $\text{m}^3\text{-Pa/K-mol}$ )

$T$ : Absolute temperature (K)

$k(T)$ : Kinetic reaction constant ( $\text{m/s}$ )

$C_{O_2}$ : Oxygen concentration

The temperature dependence of the kinetic reaction constant is usually described by the Arrhenius equation [14],



$$k(T) = A \exp \left[ -\frac{E_A}{R T} \right] \quad (2.10)$$

Where  $A$  (the pre-exponential factor, which indicates how many collisions occur to lead to producing products) and  $E_A$  (the activation energy) are the Arrhenius parameters and  $R$  is the gas constant. Kinetic reaction constant (m/s) is dependent on the type and crystalline of carbon [40, 41]. It is reported that crystallinity or graphitic carbon is less susceptible to oxidation. Carbon material derived from polyacrylonitrile (PAN) is more crystalline in the interior than the edge carbon fiber. Thus, the interior of carbon fiber is more oxidation resistant than the edge [41]. Substituting Equation 2.10 into 2.9, the carbon reaction rate can be expressed as,

$$\dot{m}_C'' = \frac{MW_C MW_{mix}}{MW_{O_2}} \frac{P}{RT} A \exp \left[ -\frac{E_A}{R T} \right] C_{O_2}(x, y, z, t) \quad (2.11)$$

In Equation 2.11, the carbon reaction rate is a function of temperature and oxygen concentration which is in turn function of time and location. In past studies of oxidation assessment of C/C composite, constant or linear gradient of oxygen concentration is assumed to simplify Equation 2.11 [28, 29]. However, the time and location dependent oxygen concentration are accounted for in this study to assess the local oxidation due to foam microstructures. Also, it should be noted that temperature is a dominant factor in oxidation since it exponentially increases with temperature.

### 2.2.2. Oxygen Mass Balance

Carbon foam oxidation is characterized as a heterogeneous reaction. In order to identify the oxygen concentration profile, two volumes are considered simultaneously: one is the ligament volume and the other is air volume. The approach here is similar to that used by other investigators [42-44]. As shown in Figure 2.5, the mass balance of oxygen in an infinitesimal element at time  $t$  is defined as '*Inlet oxygen concentration flux – outlet oxygen concentration flux = oxygen concentration flux at carbon surface*'.

$$J_{O_2}^{Inlet}(z) - J_{O_2}^{Outlet}(z + dz) = J_{O_2}(z) \quad (2.12)$$

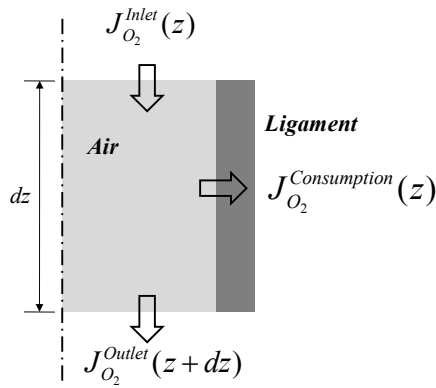
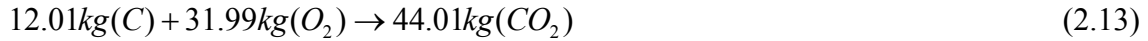


Figure 2. 5. Schematic of mass balance of oxygen at an infinitesimal interface.

The right hand side term is the oxygen flux at the boundary between air and the ligament surface, which is directly correlated to the carbon reaction rate in the form of Arrhenius expression. The stoichiometric balance in this reaction model is [39]:



On a per-kilogram-of carbon basis,  $1kg(C) + \beta kg(O_2) \rightarrow (\beta + 1)kg(CO_2)$ ,

the mass stoichiometric coefficient ( $\beta$ ) is,

$$\beta = \frac{32kg(O_2)}{12kg(C)} = 2.67$$

(2.14)

Therefore, the oxygen flux has the following relationship,

$$J_{O_2}^{Consumption} = 2.67\dot{m}_C \quad (2.15)$$

## 2.3. TGA Experiments

### 2.3.1. Test Overview and Sample Preparation

Thermogravimetric analysis (TGA) has been widely accepted for studying the kinetics of solid-state thermal reactions, such as decomposition of inorganic material and oxidation of carbon materials since it reports a continuous *in situ* measurement of mass during the test [25]. Thus this approach is selected to investigate the oxidation behavior of carbon foam as well [14, 23]. The mass loss rates at different temperatures (600, 700, and 800°C) are compared to investigate the effect of temperature on the oxidation of carbon foam. The mass loss at these temperatures is utilized to determine the apparent activation energy of carbon foam. Figure 2.6 shows the test equipment (SDT Q600 simultaneous thermal analyzer) used for this work.

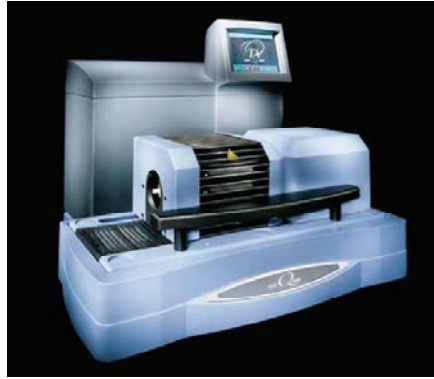


Figure 2. 6. TGA test equipment (SDT Q 600).

The carbon foam used in this study is provided by Touchstone Research Ltd [45]. With the volume of sample of  $22.0 \times 24.4 \times 38.3 \text{ mm}^3$  and mass of 3.342 g, the bulk density ( $\rho^*$ ) of the foam is calculated to be  $0.306 \text{ g/cm}^3$ . The porosity of the foam is then given by Gibson and Ashby [31] as  $\Phi = 1 - \rho^* / \rho_s$  (where  $\rho_s$  is the density of solid carbon,  $1800 \text{ kg/m}^3$ ) and is calculated to be 0.829, 82.9%. Table 2.2 presents the product data sheet, which is provided by Touchstone Research Ltd.

Table 2. 2. Product data sheet [45]

Properties	Touchstone CFOAM
Density	$0.32 \text{ g/cm}^3$
Max. operational use temperature	600 °C in Air 3000 °C in Inert
Compressive Modulus	620 MPa
Compressive Strength	8.3 MPa
Tensile Strength	2.2 MPa
Coefficient of Thermal Expansion	5 ppm/°C

This block was cut into the size for TGA test. Each sample is placed in a silica pan after calibration of mass. The dimensions and initial masses are given Table 2.3.

Table 2. 3. Dimension and initial mass of TGA samples

		600°C	700°C	800°C
Sample set #1	Dimension (mm)	7.0 x 7.0 x 6.4	7.0 x 7.0 x 0.64	7.0 x 7.0 x 0.64
	Mass(mg)	102.3 mg	102.6 mg	103.1 mg
Sample set #2	Dimension (mm)	7.0 x 7.0 x 6.5	7.0 x 7.0 x 6.6	7.0 x 7.0 x 6.6
	Mass(mg)	104.1 mg	106.1 mg	106.3 mg
Sample set #3	Dimension (mm)	7.0 x 7.0 x 6.7	7.0 x 7.0 x 6.8	7.0 x 7.0 x 6.9
	Mass(mg)	108.3 mg	109.1 mg	110.2 mg
Average mass		104.9 mg	105.9 mg	106.5 mg

In order to prevent samples from oxidizing during heating, the carbon foam samples (initial mass of 105.8 mg, 2.9 Std Dev) were heated to the desired temperature in flowing nitrogen (99.99%, 50 ml/min). Note that the carbon is not oxidized up to a temperature of 3000°C in inert gas (nitrogen) [14]. When the desired temperature was reached, the gas was switched from nitrogen to air (flowing rate of air: 50 ml/min). The mass of sample during oxidation was monitored as a function of time at each test set of 600, 700, and 800 °C.

### 2.3.2. Mass Loss

From in situ measurement of mass, the percent mass loss is defined as,

$$\% \text{ Mass Loss} = \frac{m_o - m_t}{m_o} \times 100 \quad (2.16)$$

where  $m_o$  is initial mass and  $m_t$  is mass at exposure time  $t$ . The percent mass loss of each specimen at a specific temperature is presented in Figure 2.7. As temperature increases, it is obvious that the mass loss also increases. It is also seen that the mass loss is a linear function of time is 0-50% and non-linear is over 50%. These results match well with previous research findings in carbon-carbon oxidation. They reported that linear region is 0-60% and non-linear is over 60% [14, 46].

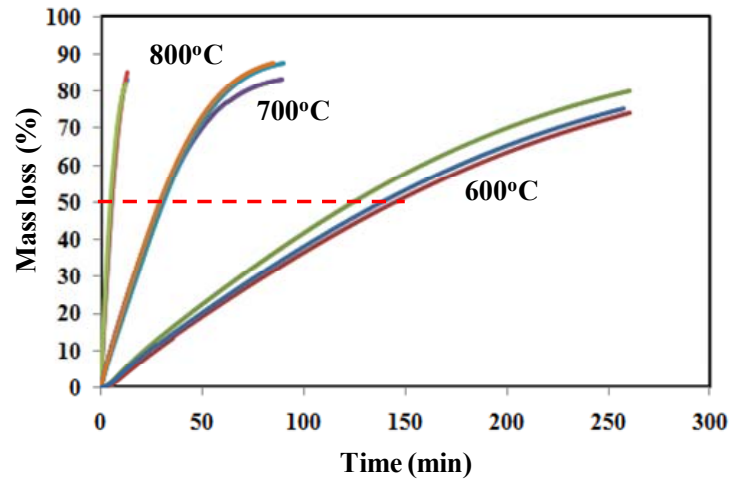


Figure 2. 7. Percent mass loss as a function of time at three different temperatures (600, 700, 800 °C).

In addition to the mass loss using Equation 2.16, the normalized mass rate ( $\bar{\dot{m}}$ ) can be expressed as [14, 46],

$$\bar{\dot{m}} = \frac{dm}{dt} \frac{1}{m_o} \quad (2.17)$$

where  $m_o$  is initial mass of carbon. At temperature of 600°C, the average value of  $\bar{\dot{m}}$  is 6.25e-5 kg/kg-sec (4.48e-5 Std Dev). At temperature 700°C and 800°C, the average values of  $\bar{\dot{m}}$  are 2.74e-4 kg/kg-sec (1.32e-5 Std Dev) and are 1.70e-3 kg/kg-sec (1.39e-4 Std Dev), respectively. Note that the mass loss rate of carbon foam also exponentially increases as a function of temperature seen in Figure 2.8.

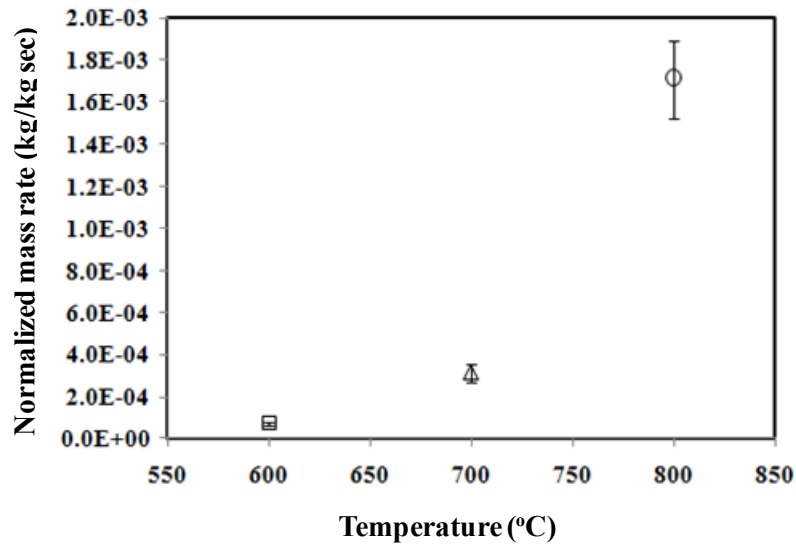


Figure 2. 8. Plot of normalized mass rate ( $\bar{\dot{m}}$ ) vs. temperature.

The activation energy is a term introduced in 1889 by the Swedish scientist Svante Arrhenius, that is defined as the energy that must be overcome in order for a chemical reaction to occur [47]. In other words, activation energy may be also defined as the minimum energy required for initiating a chemical reaction. The apparent activation

energy of a sample can be determined by a progress degree of the reaction (mass loss) and the suggested equation is as follows [14, 46].

$$\ln t_{\alpha,i} = -\ln\left(\frac{A}{\alpha}\right) + \frac{E_A}{RT} \quad (2.18)$$

where,  $\alpha$  is mass loss  $((m_o - m_t)/m_o)$ ,  $A$  is pre-exponential factor,  $E_A$  is activation energy,  $R$  (8.314 J/mol K) is gas constant, and  $T$  is the absolute temperature. According to Equation 2.18, the apparent activation energy ( $E_A$ ) is the slope of the plot  $\ln t_i$  against  $T_i^{-1}$ . The value of  $E_A$  and the coefficient of determination ( $r^2$ ) are summarized in Table 2.4. The average activation energy in this temperature range (600-800°C) is 123.12 kJ/mol (2.05 Std Dev) and average coefficient determination ( $r^2$ ) is 0.9933. According to the literature data [50], the activation energy of pitch based carbon fibers vary from 112 kJ/mol to 205 kJ/mol.

Table 2. 4. Calculated activation energy at each mass loss %

Time (min)			Mass loss (%)	$E_A$ (kJ/mol)	$r^2$
600°C	700°C	800°C			
24.25	5.47	0.98	10	123.86	0.9902
48.99	9.68	2.04	20	121.23	0.9977
76.07	15.10	3.17	30	120.93	0.9976
105.73	24.11	4.15	40	125.57	0.9889
137.96	29.93	5.67	50	123.70	0.9934
Average				123.12	0.9933



## 2.4. Furnace Exposure Test

### 2.4.1. Test Overview

Microscopy studies were undertaken to document the morphological changes observed in the samples post oxidation. Before the temperature exposure tests, the carbon foam samples images were taken in the optical microscopy (OM) and then they were placed in the center of furnace where sample was in contact with furnace bottom. The ramp temperature (500-800°C) subjected to each sample. The dimensions of carbon foam samples and initial mass are given in Table 2.5. Pictured in Figure 2.9 is the furnace (Cress Mfg. Co.) used to perform the oxidation test (maximum temperature: 1230°C, furnace volume: 0.025m<sup>3</sup>). The sample was placed at the center of furnace and the temperature was controlled by the thermocouple which is located at back wall of the furnace.

Table 2. 5. Sample dimension and mass

	Length (mm)	Width (mm)	Thickness (mm)	Mass (g)	Volume ratio ( $V_{sample}/V_{furnace}$ )
Sample # 1	22.4	13.8	8.9	0.87	0.0001
Sample # 2	22.1	19.1	13.1	1.69	0.0002
Sample # 3	30.4	16.5	14.9	2.29	0.0003
Sample # 4	30.4	22.4	29.1	6.06	0.0008

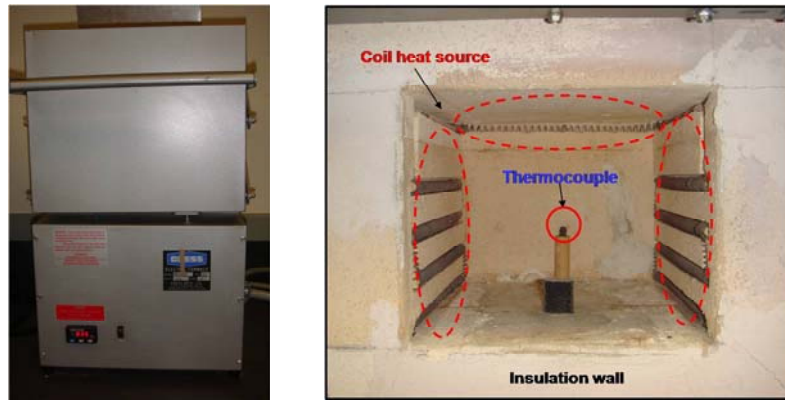


Figure 2. 9. Photograph of the furnace (Cress Mfg. Co.) used in the oxidation test.

#### 2.4.2. Microscopy Observations Post Oxidation

Morphological changes of the ligaments were investigated at five exposed surfaces as well as the protected surface. Optical microscopy (Olympus SXZ 16) at 5x and 10x images before and after about 100 minutes of were taken to identify any morphological change at the same locations. The OM images were taken by controlling the position adjustment of the stage and the coordinates were recorded (10 images at each surface). The images at the identical position (before and post oxidation) are compared to each other.

##### 2.4.2.1. Exposed Surfaces

The representative images are compared in low magnification (5x) as seen in Figure 2.10. Here it is seen that protrusions around the pore are removed (pointed by arrow A) and pore is enlarged (pointed by arrow B and C), as indicated by arrows. In addition, pore dimension increased by the formation of carbon monoxides and dioxides.

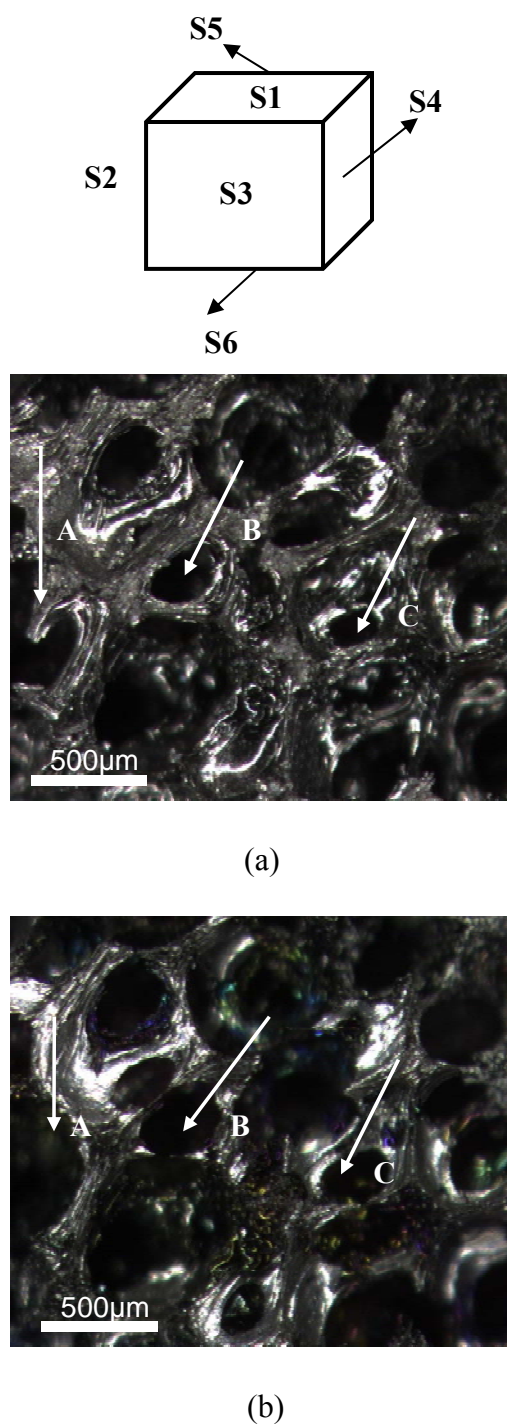


Figure 2. 10. Representative images at S1: (a) before exposure and (b) after 100 minutes of exposure.

A similar phenomenon has been observed by Guo W. [14] during the microscopic inspection of oxidation of carbon fiber. They reported that carbon fibers exhibited a reduced diameter compared to the fibers before oxidation, and there were many micro-depressions running parallel to the fiber axes in the initial stage. However, in the later stages of oxidation, the surface of the fibers became ‘glossy’ as seen in Figure 2.11.

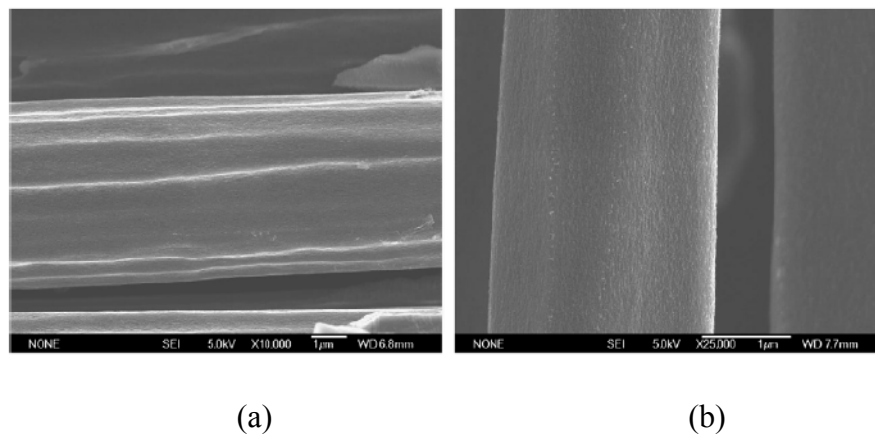


Figure 2. 11. Microscopical investigation of the oxidation process of carbon fibers: (a) weight loss 31 % and (b) weight loss of 72 % [14]. (Reprinted with Permission of Elsevier.)

These representative features are then categorized as ligament disconnection, pore merge and pore creation and presented in Figures 2.12-2.14. First, it was seen that the ligament thickness is reduced, leading to the increase in pore size. Oxygen attack on relatively thin ligaments leads to the ligament disconnection as seen in Figure 2.12 where three different locations are presented before and after oxidation. Note that the first distinct degradation mode was reduction of ligament thickness, which was observed in the overall image and caused disconnection at the relatively thinner ligaments as indicated by the arrows in Figure 2.12.

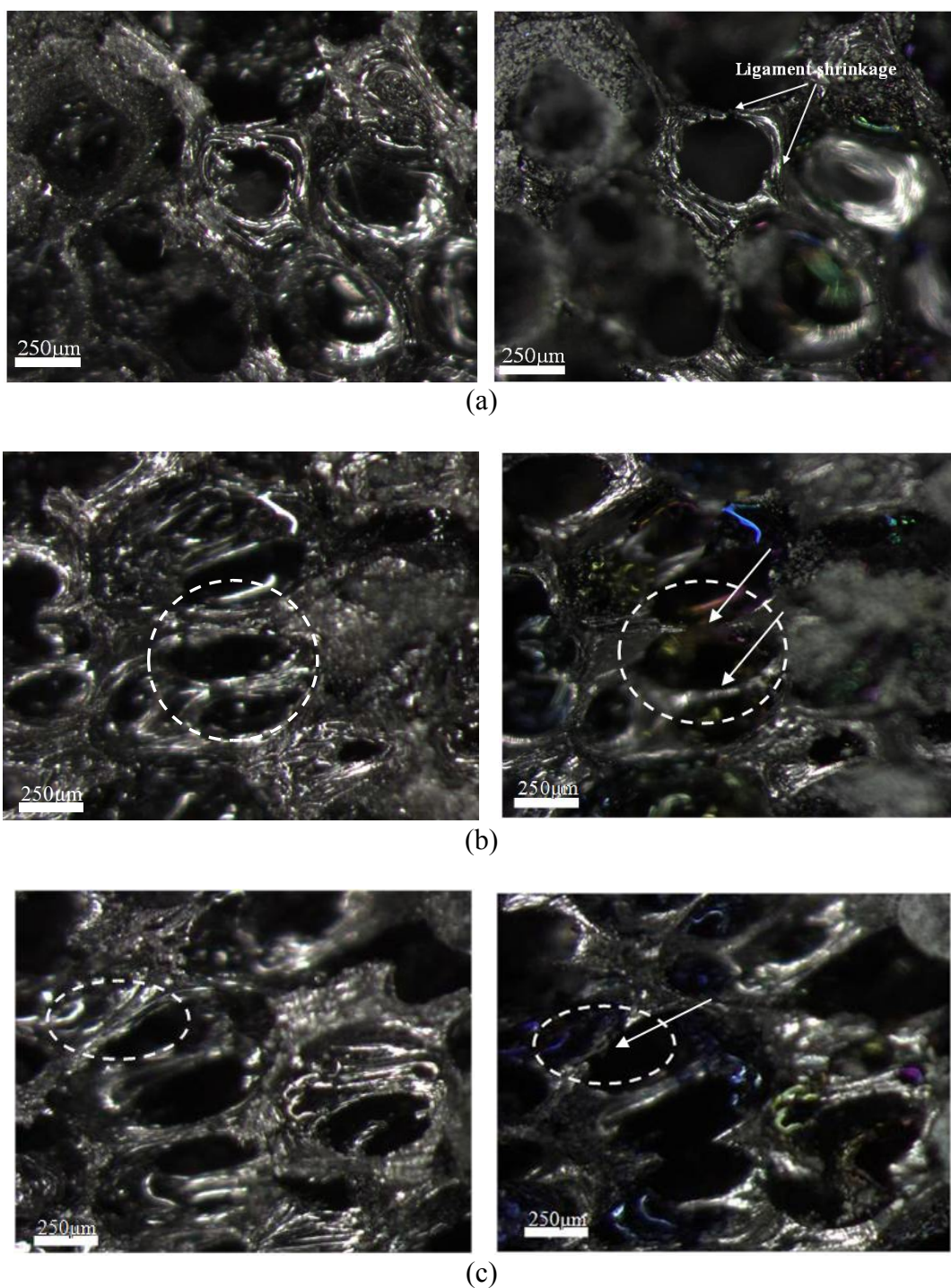


Figure 2. 12. . Representative OM images of “ligament thickness reduction and disconnection”: (a) at S1 surface, (b) at S1 surface, and (c) at S2 surface.



Second degradation pattern is merging of pore to create a larger pore as indicated by the arrows in Figure 2.13. Initial oxidation of the thinner ligament resulted in disconnection and further oxidation at the disconnected tip of the ligament formed the larger pore.

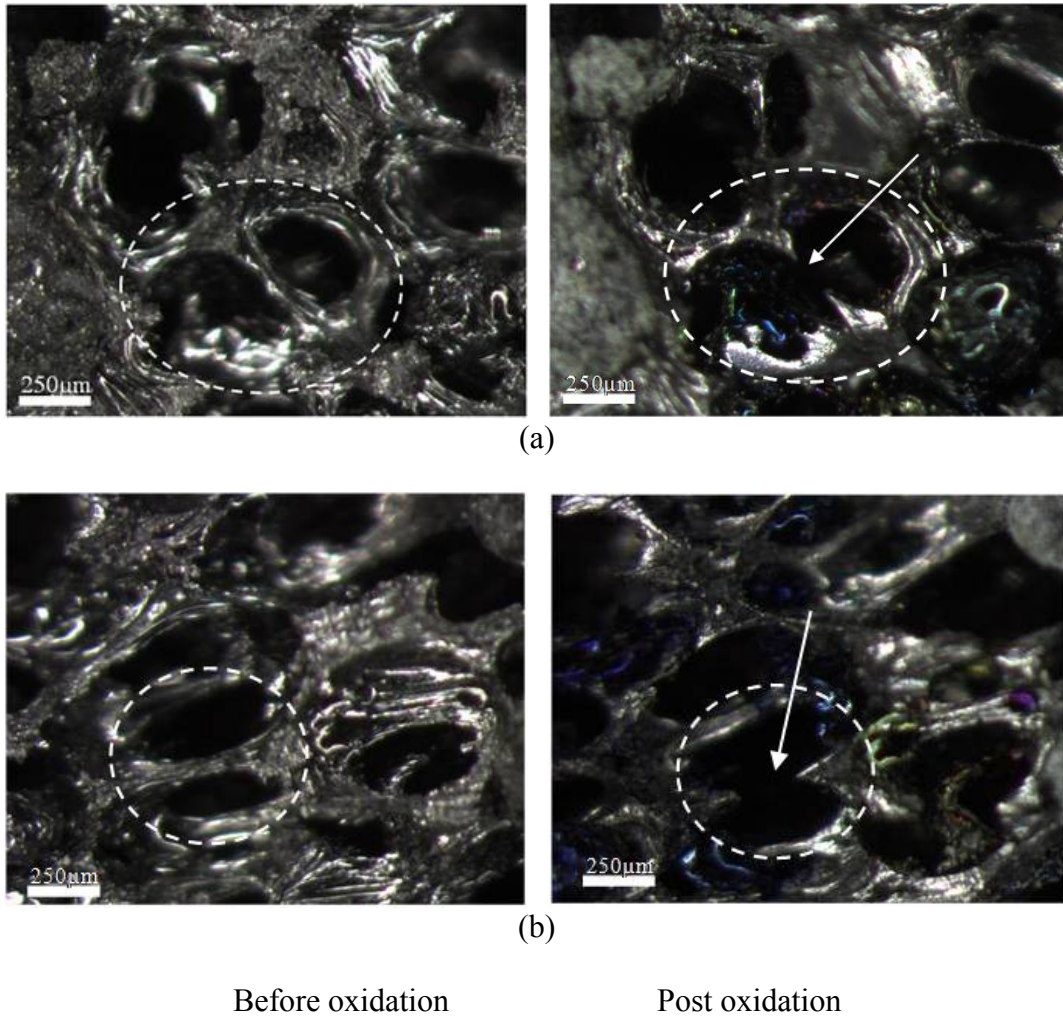


Figure 2. 13. Representative OM images of “pore merge”: (a) at S4 surface and (b) S2 surface.

The third representative change in morphology is the creation of a new pore. The partially closed surface in the cell (thin membrane or micro crack), which may have

formed during the manufacturing process by irregularity and imperfection of the pore as seen in Figure 2.14(left images) is then attacked by oxygen creating a small pore and then subsequently enlarged by the oxidation process.

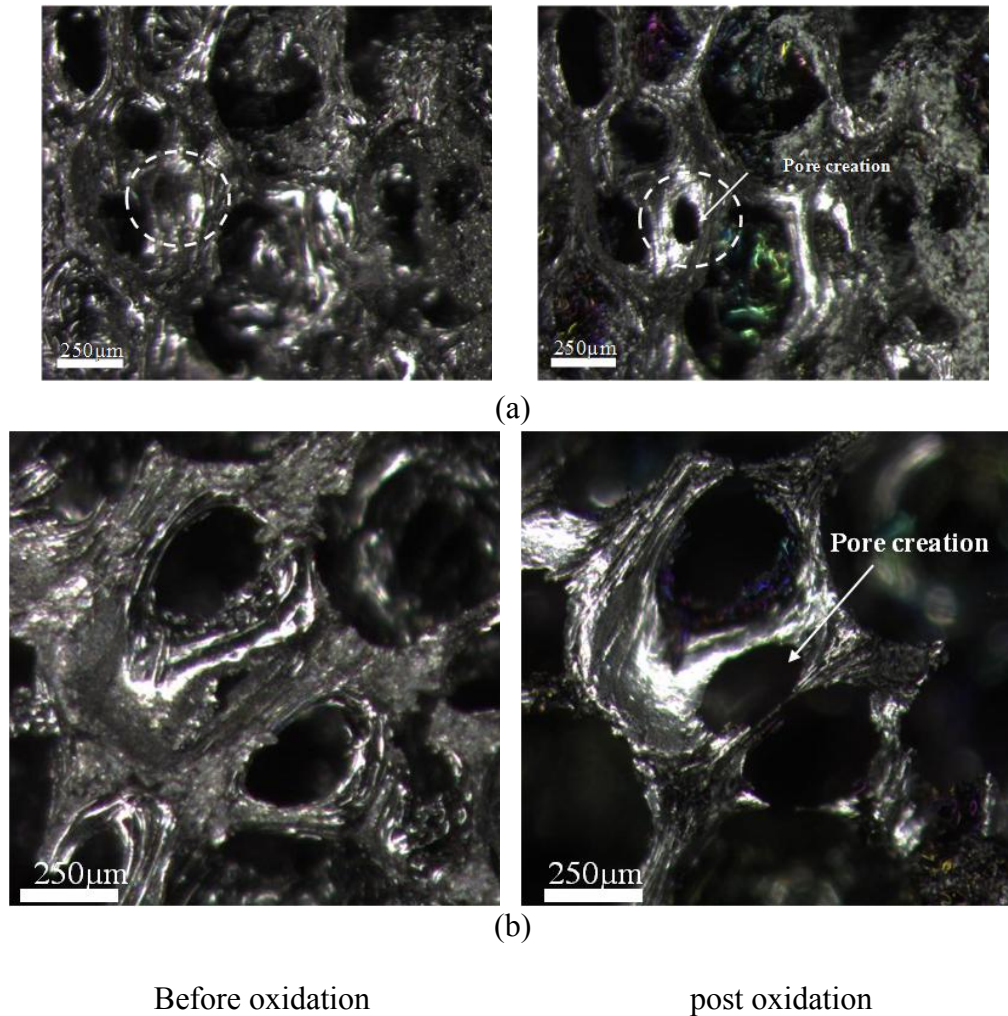


Figure 2. 14. Representative OM images of “pore creation”: (a) at S1 surface and (b) S4 surface.

#### 2.4.2.2. Bottom Protected Surface

As mentioned in Section 2.2.1, carbon reaction rate is a function of oxygen

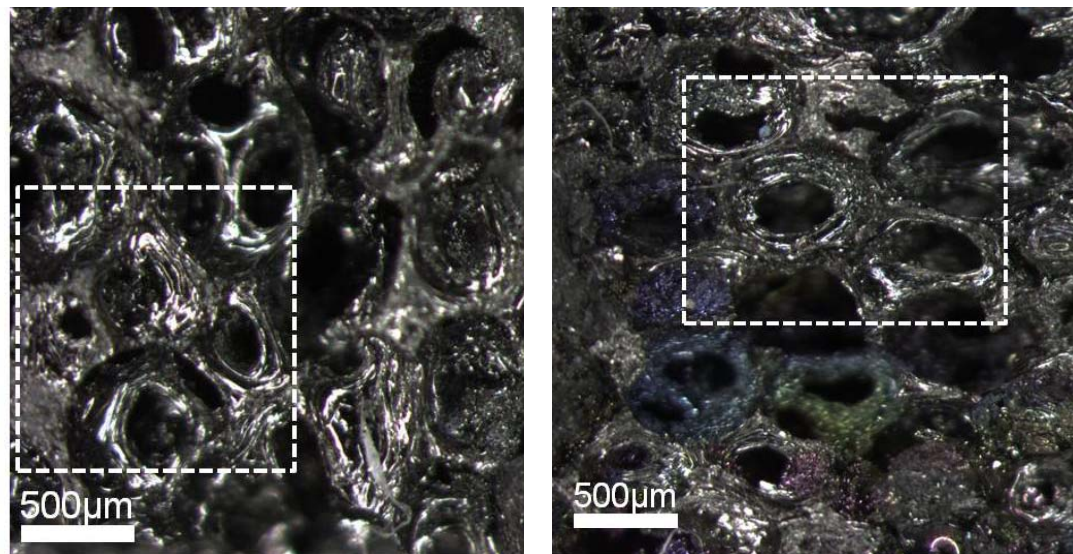
concentration. The three degradation features reported by the OM image analysis in the previous section are attributed to high oxygen concentration (similar to an atmospheric condition), since the observed surfaces were directly exposed to air without any barrier wall. Similarly, low magnification (5x) of OM images of the surfaces which were in contact with furnace bottom were also taken in Figure 2.15. In addition, high magnification (10x) images as highlighted by boxes in Figure 2.15 were compared to each other in Figure 2.16.

First, note that no distinct change in ligament thickness and pore size were observed as seen in Figure 2.15. However, the glossy area became larger and uniform compared to the highlighted zone (rectangular box) after oxidation, even though OM images were taken under the same lighting condition. Larger glossy area indicated that the removal of the micro protrusion on the surface resulted in the reduction of surface roughness. Therefore, more uniform light reflection was observed after the furnace exposure test. When looking at the high magnification OM images (Figure 2.16), it was more obvious that no distinct morphological change was observed such as ligament reduction, pore merge and pore creation. However, only protrusion on the ligament was removed and a smoother surface around the pore was formed due to low oxygen concentration as seen in Figure 2.16 (b).

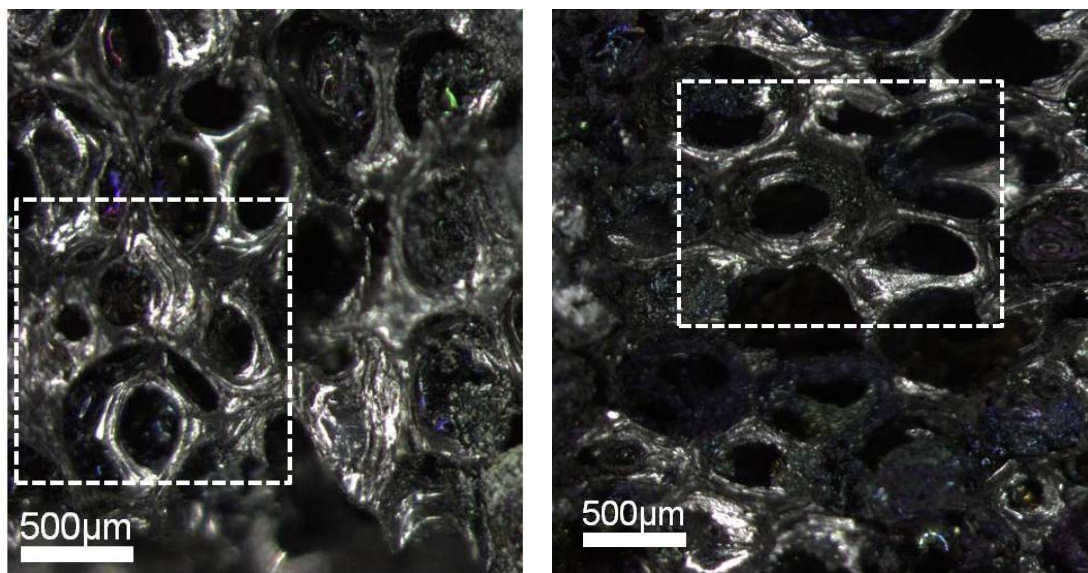
Although this surface was protected by the furnace bottom, some morphological changes were still detected. This can be explained as follows. Initially, the pore volume in the carbon foam has the same concentration of oxygen as in air. However, the oxygen concentration was decreased to form carbon monoxide and/or carbon dioxide and fill the



pore volume in carbon foam by its reaction with carbon. According to literature [23], it is that the carbon reaction rate by carbon monoxide or dioxide is much lower than that of oxygen (<5%).

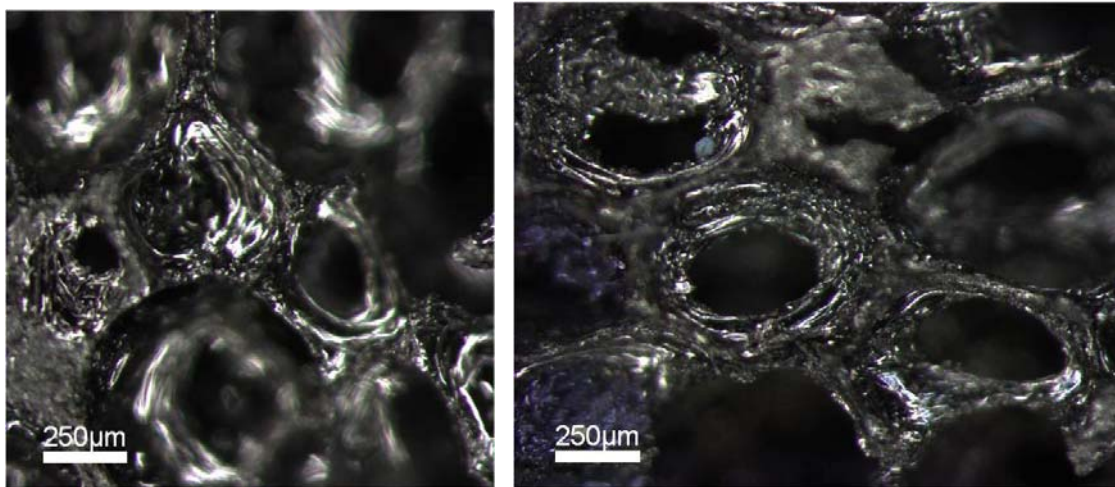


(a)

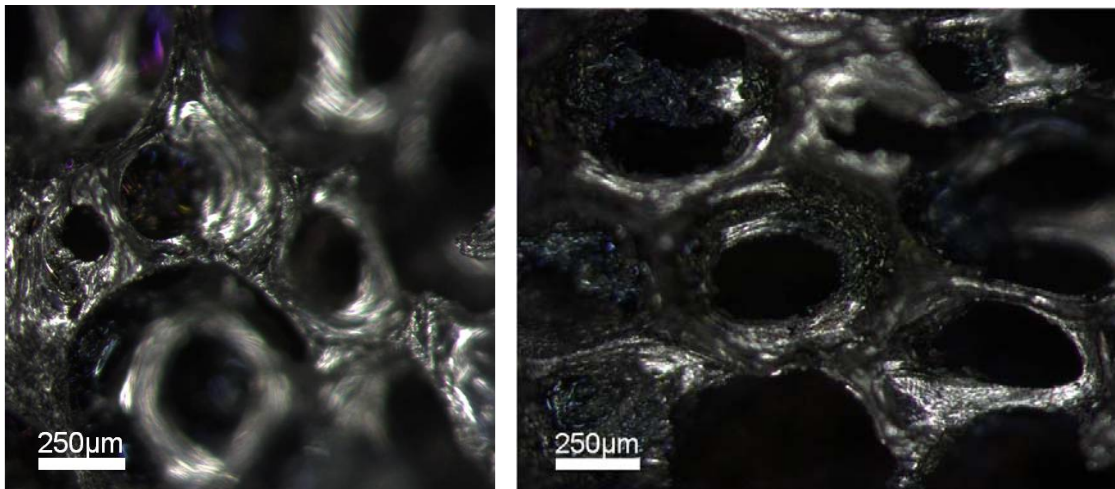


(b)

Figure 2. 15. Low magnification OM images of protected by furnace bottom: (a) before oxidation and (b) post oxidation



(a)



(b)

Figure 2. 16. High magnification OM images sites in contact with furnace bottom: (a) before oxidation and (b) post oxidation.

## 2.5. Remarks

Continuous in-situ measurement of mass loss was recorded by thermogravimetric analyzer (TGA) at three different temperatures. From the time history of mass loss data, the average mass rate at each temperature was calculated and compared as seen in Figure 2.7. It is seen that similar to the relationship between the kinetic reaction rate constant and temperature, mass rate of carbon foam also exponentially increased with temperature. In addition, the activation energy of carbon foam was calculated from the slope of the slope of  $\ln t_i$  against  $T_i^{-1}$ . Apparent activation energy which are determined from mass loss data at the three temperature (600 ~ 800°C) is 123.12kJ/mol (2.05 Std Dev). Note that when compared with the activation energy of pitch based carbon (112~205 kJ/mol), carbon foam showed lower oxidation resistance than carbon fiber due to the lower crystallite parameters, meaning there are more edge carbon atoms for oxidation [48].

In addition, furnace exposure tests were performed to identify any morphological change post oxidation. As shown in Figures 2.12-2.14, three distinct degradation patterns were observed and categorized such as ligament disconnection, pore merge and pore creation. Although the surface was contacted with the furnace bottom, a microscopic change in foam geometry was detected such as removal of protrusions. As exposure time increased, the oxygen concentration was decreased to form carbon monoxide and/or carbon dioxide by its reaction with carbon. According to data in the literature [23], reaction rate by carbon oxides is much smaller than that of oxygen (<5%).

### 3. COMPUTATIONAL APPROACH

#### 3.1. Overview

Computational models are developed to study the degree of oxidation in carbon foam as a function of time and temperature. First, the foam microstructure of 83% porosity is generated based on the porosity of samples in the TGA experiments, where the corresponding pore volume is 83% and ligament volume is 17%. The ligaments were assuming equilateral triangle cross-section. These geometries are simulated with the atmospheric oxygen concentration at the exterior surface and the flux boundary condition of oxygen concentration between the ligaments and pore (air) interfaces. From the carbon reaction rates coupled with oxygen concentration profile, mass losses are evaluated as a function of location, such as outer, middle, and inner zone of the foam model.

Although temperature is a dominant factor in oxidation [14], the carbon reaction rate is also dependent on the sample porosity. Three different foam models with 83%, 90%, and 95% porosity are created for finite element analysis to investigate the effect of foam porosity on the oxygen concentration profile. The total mass loss is calculated by the summation of the local mass loss and compared to the TGA experimental results for the model validation at temperatures of 600°C, 700°C, and 800°C.

### 3.2. Oxygen Concentration Profile: Diffusion Analysis

#### 3.2.1. Model Description

The carbon foam microstructure is comprised of tetrakaidecahedra single cells. A single cell consists of 36 ligaments arranged in 6 planar quadrilateral faces and 8 hexagonal faces as presented in Figure 2.1. In order to reduce the computational work penalty, the quarter model with dimension of 3.5 mm x 3.5 mm x 7 mm was utilized for FE analysis with the symmetry boundary conditions instead of the full model. The foam model consists of two volumes: one is ligament volume (17%) as a carbon and the other is air (pore) volume (83%) as shown Figure 3.1.

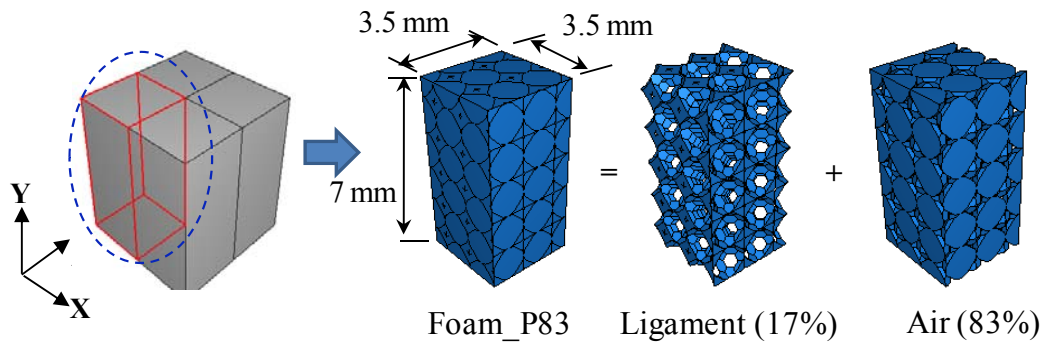


Figure 3. 1. Illustration of the quarter foam model.

The cross section of the ligament was assumed to be an equilateral triangle and the shared ligaments were modeled with half cross-sections at the symmetry surfaces. The total number of ligaments is 1125 in this model. Solid quadratic tetrahedron elements with ten nodes are assigned to model and schematic of this element is illustrated in Figure 3.2. The ligament volume is represented with 429,260 elements and the air volume with 56,926.



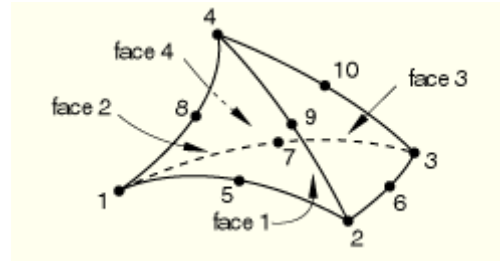


Figure 3. 2. Schematic of 10-node quadratic tetrahedron element.

Fick's second law as expressed below is used for this analysis,

$$\frac{\partial C_{O_2}}{\partial t} = D_{O_2-N_2} \left( \frac{\partial^2 C_{O_2}}{\partial x^2} + \frac{\partial^2 C_{O_2}}{\partial y^2} + \frac{\partial^2 C_{O_2}}{\partial z^2} \right) \quad (3.1)$$

Here, the oxygen concentration ( $C_{O_2}$ ) is a function of time and location and the binary diffusion coefficient ( $D_{O_2-N_2}$ ) was calculated from the Chapman–Enskog relationship [44]. Details of the binary diffusion principles are outlined in appendix A. At 600°C, the diffusion coefficient and density of air are  $1.27 \times 10^{-4}$  m<sup>2</sup>/sec and 0.4 kg/m<sup>3</sup> and those of carbon are  $8.33 \times 10^{-13}$  m<sup>2</sup>/sec and 1800 kg/m<sup>3</sup> [43, 44].

### 3.2.2. Initial and Boundary Conditions

To determine the oxygen concentration distribution, it is necessary to solve the transient diffusion equation with the appropriate boundary conditions to reflect TGA experiments for later comparison. As described in the testing condition in Section 2.3.1, in order to prevent the samples from oxidation during the heating process, nitrogen gas was introduced initially. Thus, oxygen concentration of  $C_{O_2}^{initial} = 0$  was applied to the

model as an initial boundary condition. In the quarter size model, the following symmetric boundary conditions were applied to x and z surfaces, as illustrated in Figure 3.3.

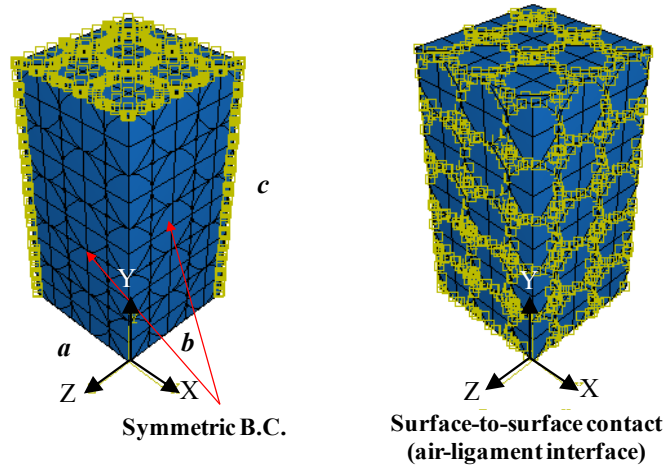


Figure 3. 3. Boundary conditions.

The oxygen concentration at the exposed surfaces (highlighted by yellow color in the left figure 3.3) was maintained at a constant value corresponding to the atmospheric oxygen concentration (0.21). In the OM image comparisons between pre and post oxidation, no distinct morphological changes were observed at the bottom surface due to the protection by the crucible bottom as shown in Figures 2.15 and 2.16. Thus the bottom surface was treated as impermeable surface [49]. In summary, the initial and boundary condition for the quarter-size model are as follows,

Initial condition:

$$C_{O_2}(x, y, z) = 0 \quad \text{at } t = 0$$

Exposed surfaces:

$$C_{O_2}(-a, y, z) = C_{O_2}(x, y, -b) = C_{O_2}(x, y, c) = 0.21, \quad \text{at } t > 0$$

Symmetry surfaces:

$$D \frac{\partial C_{O_2}}{\partial x} \Big|_{x=0} = D \frac{\partial C_{O_2}}{\partial z} \Big|_{z=0} = 0, \quad \text{at } t > 0$$

Impermeable surface:

$$\frac{\partial C_{O_2}}{\partial y} \Big|_{y=0} = 0, \text{ at } t > 0$$

The following oxygen flux boundary condition which is dependent on oxygen concentration is introduced at all the interfaces between the ligament and air. This is accomplished in ABAQUS by using the mass transfer coefficient ( $h_m$ , m/s) at interface between the ligament and air. The relationship between oxygen flux and mass transfer coefficient is defined as follow,

$$J_{O_2}^{Consumption} = \rho h_m C_{O_2}(x, y, z, t) \quad (3.2)$$

Using Equation 2.11 and the mass stoichiometric coefficient (Equation 2.14), the mass transfer coefficient ( $h_m$ ) is calculated as  $1.36 \times 10^{-2}$  m/s for the case of temperature  $600^\circ\text{C}$ .

### 3.2.3. Time Dependent Oxygen Concentration Observation

The oxygen concentration distribution of the quarter foam model is shown in Figure 3.4 where mesh lines are removed for ease of visualization. First note that the concentration at the exposed surface is 0.21, which reflects the applied boundary condition. The oxygen concentration gradient is formed by the diffusion of oxygen from the exposed surfaces. For example, after 16.7 minutes of exposure, cells near the



exposed surface show higher oxygen concentration (0.14-0.21), but the cells at the interior experience lower oxygen concentration.

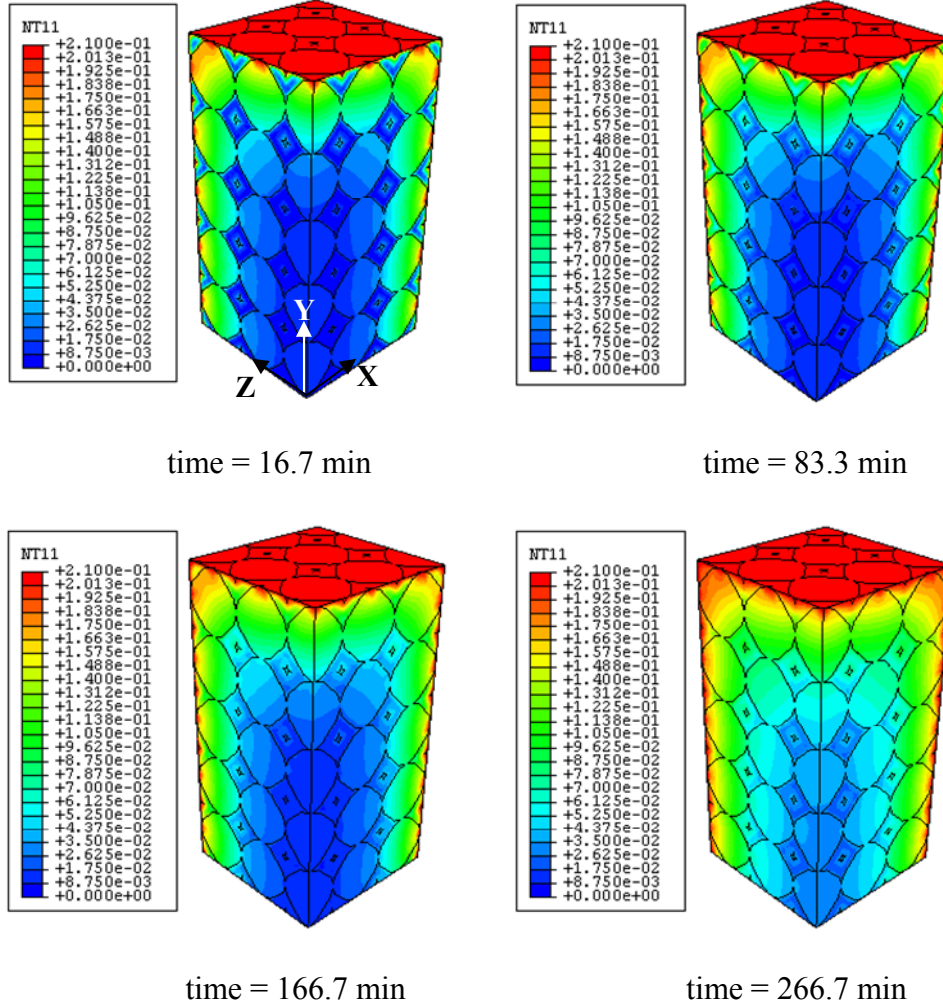


Figure 3. 4. Contour plot of oxygen concentration as a function of time.

For better understanding of the distribution, the three-dimensional profile of oxygen concentration is plotted by using 'SURF option' in MATLAB software. By assuming that  $C_{O_2}(x, y, z, t) = C_{O_2}(-x, y, z, t)$ ,  $C_{O_2}(x, y, -z, t) = C_{O_2}(-x, y, -z, t)$ , the rest of

the nodal concentrations are generated from the results of a quarter model as seen in Figure 3.5. Note that Figure 3.5(a) illustrates layer description of a quarter model. Figure (b) is the original plot of FEA result at normalized height of 0.5 after 166.7 minutes. Figure 3.5 (c) and (b) illustrate the constructed images from xy- and yz-plane, respectively.

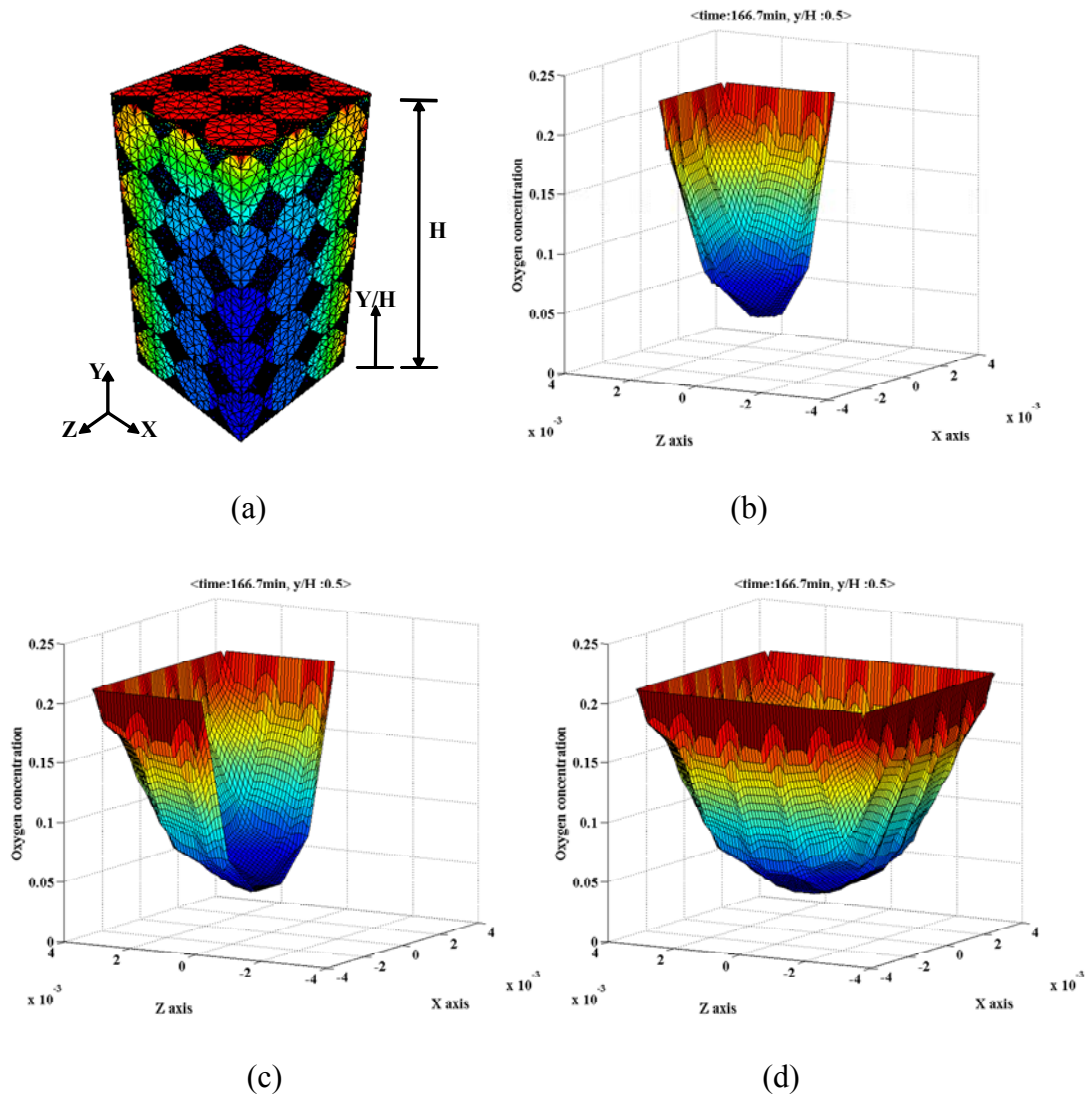


Figure 3. 5. The process of three-dimensional plot of oxygen concentration: (a) layer description, (b) original plot from FEA analysis, (c) constructed image about xy plane (d) full 3D profile.

In order to quantitatively compare with respect to exposure time and location, the three-dimensional profile of the oxygen concentration at select locations ( $y/H=0.5, 0.7$ , and  $0.9$ ) is plotted as a function of time as shown in Figure 3.6. It can be observed that the oxygen concentration is higher in close proximity to the exterior surface where the atmospheric concentration was applied. Thus these cells experienced rapidly since the reaction rate is proportional to the oxygen concentration.

The variation of the oxygen concentration with the exposure time is also clearly depicted. For example, at the location of  $y/H = 0.5$ , the cells at the exterior surface contact with high oxygen concentration ( $0.18\sim0.21$ ) but the center cells experience low oxygen concentration ( $0.025\sim0.035$ ) as seen Figure 3.5 (a) (left). However, as exposure time increases, the center cells experience a higher oxygen concentration and reach almost  $C_{O_2}$  of  $0.21$  after 300 minutes of exposure time due to the diffusion of oxygen concentration from the exterior surfaces.

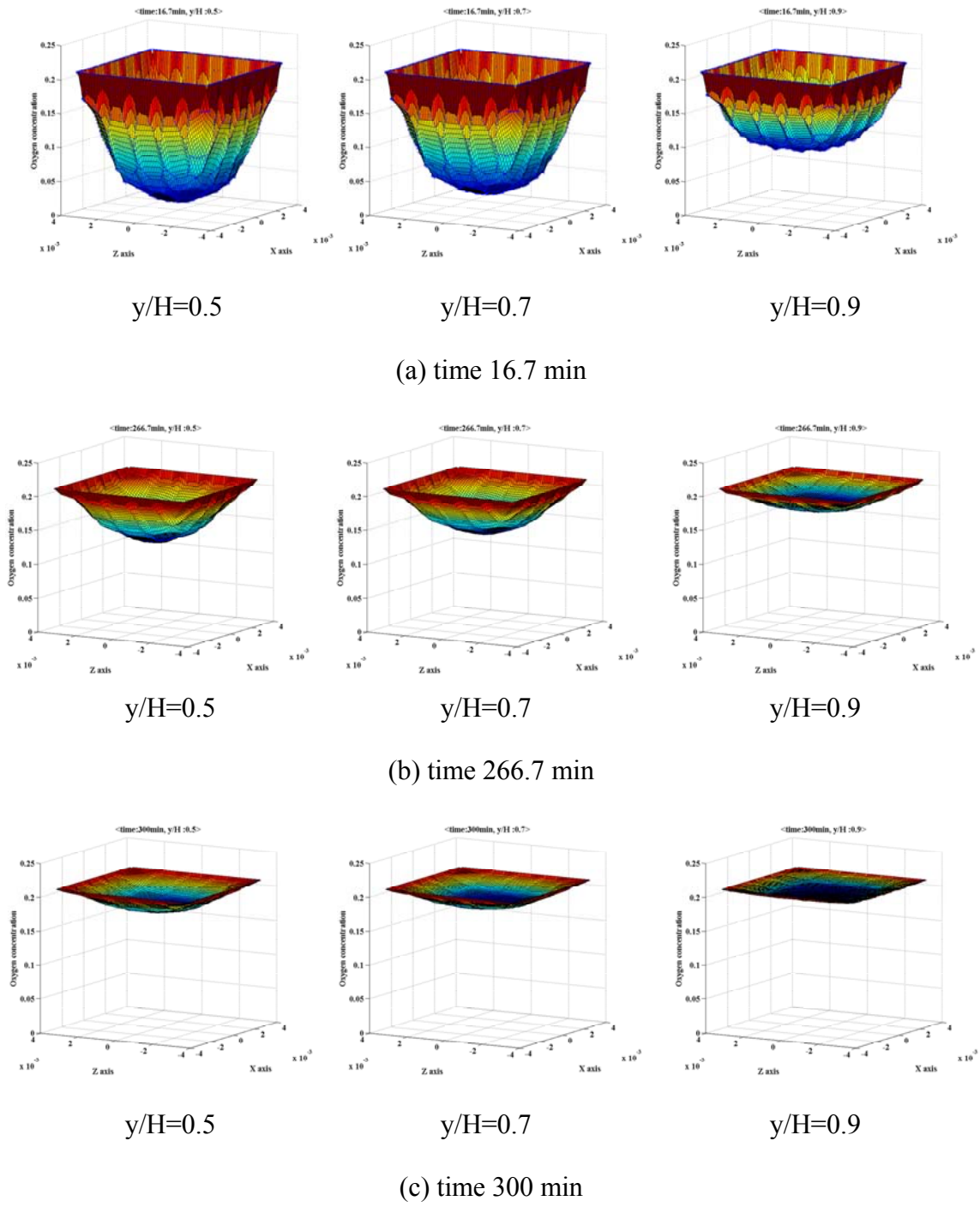
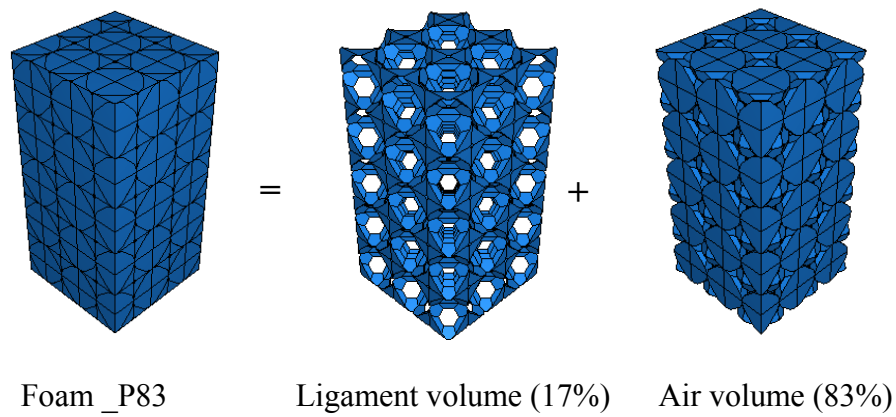


Figure 3. 6. Representatives of oxygen concentration profile throughout foam with respect to time: (a) 16.7 min, (b) 266.7 min and (c) 300 min at three different location,  $y/H=0.5$ ,  $0.7$ , and  $0.9$ .

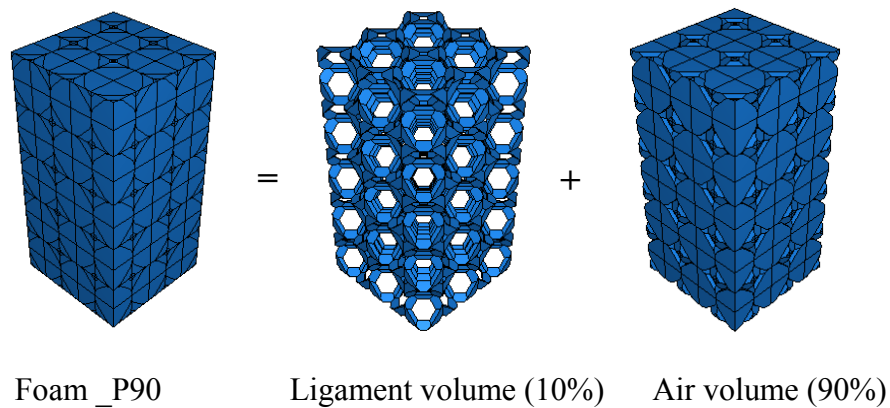
### 3.3. Influence of Porosity on Oxygen Concentration Profile

#### 3.3.1. Model Description

Three different porosity models (3.5 mm x 3.5 mm x 7mm) were introduced to investigate the effect of porosity on the oxygen concentration profile. Each model consists of the air volume and the ligament volume with following percent porosity; 83, 90 and 95% as shown in Figure 3.7. The total ligament surface areas in these models are  $320.8 \times 10^{-6} \text{ m}^2$ ,  $268.7 \times 10^{-6} \text{ m}^2$ , and  $181.5 \times 10^{-6} \text{ m}^2$ , respectively.



(a)



(b)

Figure 3. 7. Three different foam representations of a quarter model: (a) 83% porosity, (b) 90% porosity, and (c) 95% porosity.

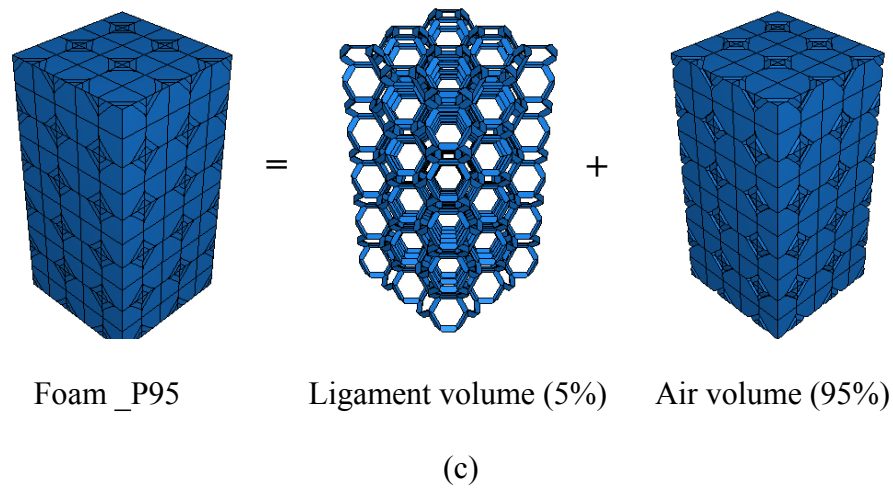


Figure 3. 7. Continued.

### 3.3.2. Results and Discussion

The same initial and boundary conditions are implemented here as illustrated in Figure 3.3. The oxygen concentration distribution is shown in Figure 3.8 as a function of exposure time. Models are sliced through visually in post-processing to illustrate the internal state of concentration in section A-A' (center of x-z plane). When looking at Figure 3.8 (a)-(c), oxygen deeply penetrates through and exposes the ligaments to a higher oxygen concentration in the high porosity foam since the total flux of oxygen concentration is proportional to the pore size. Note that same contour limit (0~0.21) is applied; red and blue contours indicate oxygen concentration of 0.21 and zero, respectively. However, the oxidation is restricted to the ligaments which are near the exterior surface in the low porosity foam (83%).

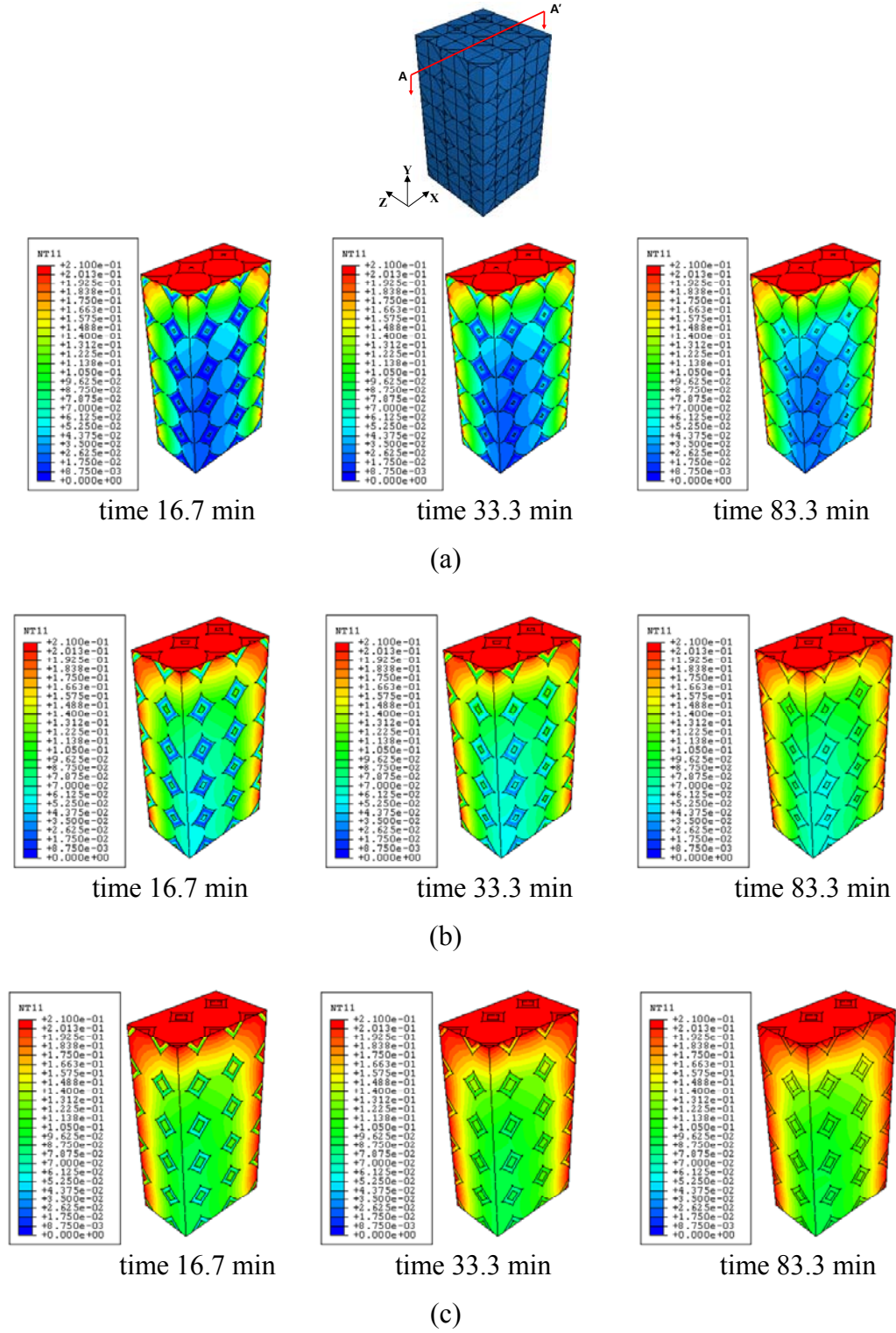


Figure 3. 8. Contour plot of oxygen concentration of section view at three different foam porosities: (a) 83%, (b) 90%, and (c) 95%.



Again, in order to quantitatively compare with respect to exposure time and location, the three-dimensional profile of the oxygen concentration at selected locations ( $y/H=0.5, 0.7$ , and  $0.9$ ) is plotted as a function of time as shown in Figure 3.9.

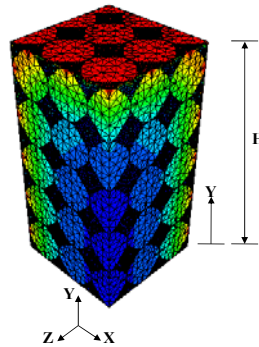


Figure 3. 9. Illustration of coordinates and normalized layer description.

Three dimensional oxygen concentration profiles for the three different porosities are compared after 16.7 minutes exposure as shown in Figure 3.10. In these plots, the same scale of axis value is plotted with data set on each layer. In Figure 3.10(a), at the normalized layer,  $y/H=0.5$ , it is noted that the oxygen concentration at the center is about 0.025 in 83% porosity model; however, its value is about 0.075 in 95% porosity model. This result indicates that reaction rate in 95% porosity foam is three times faster than in 83% porosity foam at the center. The oxygen concentration profiles near the exterior surface are similar regardless of porosity, but their values at the interior of foam increase as foam porosity increases due to the larger pore size.



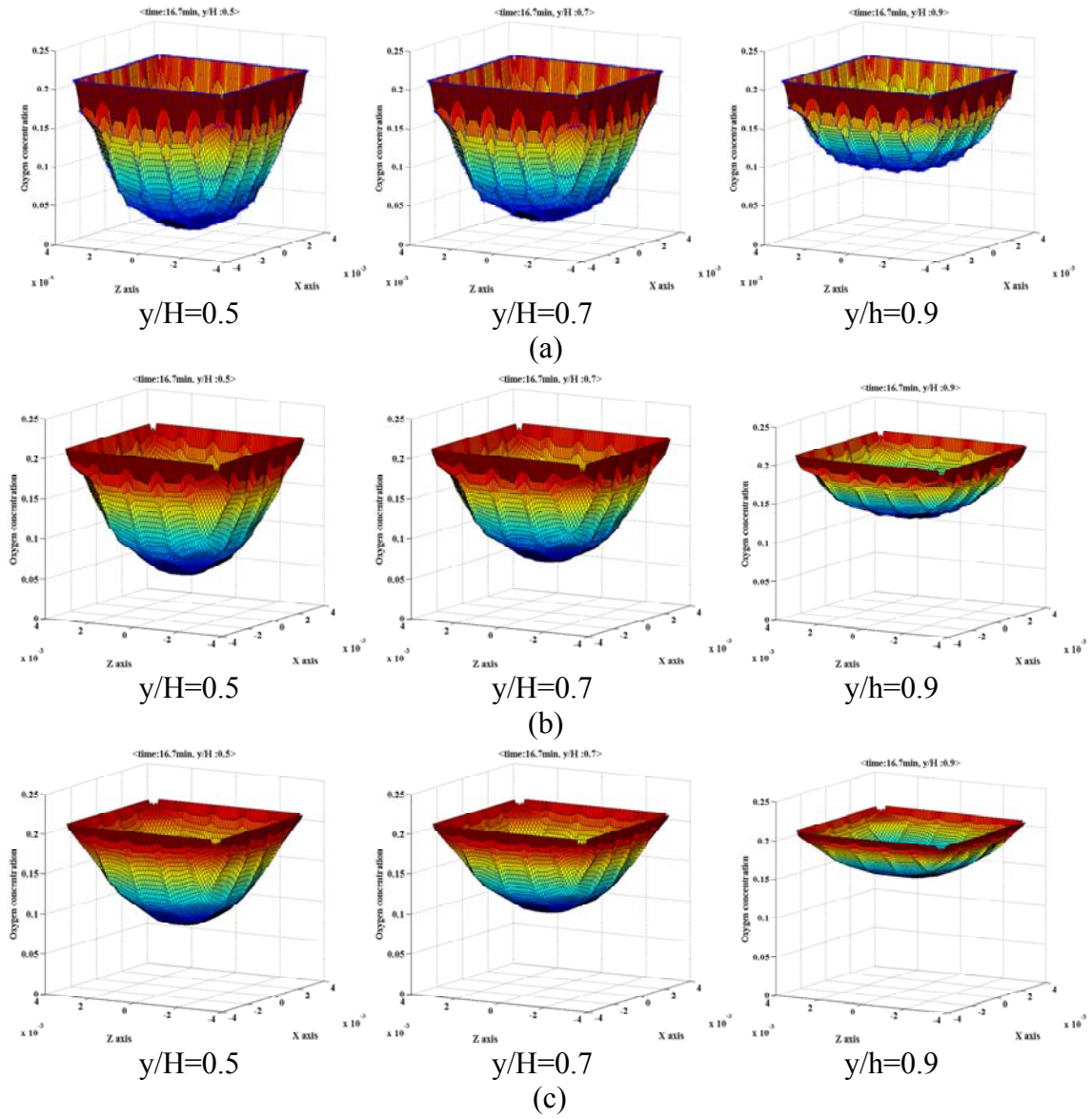


Figure 3. 10. Comparison of oxygen concentration at normalized layer of 0.5, 0.7, and 0.9 after 16.7 minutes exposure: (a) 83% porosity, (b) 90% porosity, and (c) 95% porosity.

### 3.4. Effect of Temperature on Oxygen Concentration

As described in Figure 3.11, the carbon reaction rate exponentially increases with temperature. Here, the carbon reaction rates are plotted for three different temperatures

of 600°C, 700°C, and 800°C. The carbon reaction rates are calculated by Equation 2.11 with other at the atmospheric pressure of 1 atm and oxygen concentration of 0.21.

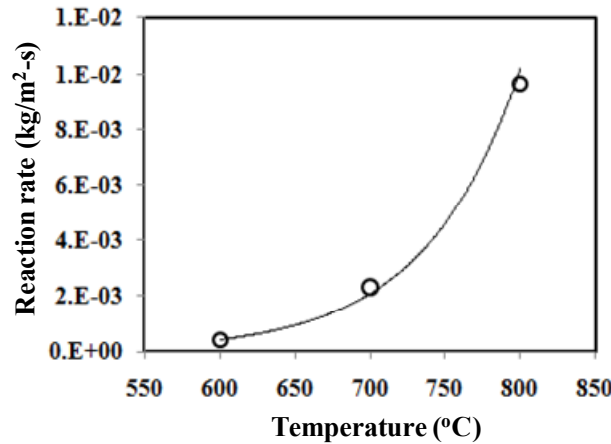


Figure 3. 11. Carbon reaction rate vs. temperature.

#### 3.4.1. Model Description

In addition to porosity, temperature dominates the carbon reaction rate since kinetic reaction rate constant ( $k$ ) exponentially increases with temperature [14]. Here, three different temperatures (600, 700, and 800°C) were considered for this study. Again, in order to reduce the computational work penalty, the quarter model was utilized for FE analysis with symmetric boundary condition instead of the full-size model. The model with 83 % porosity is adopted for this analysis. The initial and boundary conditions of Section 3.2.2 are adopted. As before, 10-node quadratic tetragon element was assigned and the same number of elements of ligament and air are generated as in Section 3.2.1. Temperature dependent material properties are given in Table 3.1 and the density of carbon is assumed to be constant (1800 kg/m<sup>3</sup>).

Table 3. 1. Temperature dependent material properties [44, 47]

	Temperature	600°C	700°C	800°C
Air	Diffusion coefficient ( $\text{m}^2/\text{sec}$ )	1.27 e-4	1.52e-4	1.78e-4
	Density( $\text{kg}/\text{m}^3$ )	0.40	0.36	0.33
	Mass transfer coefficient ( $\text{m}/\text{sec}$ )	1.36e-2	7.79e-2	3.23e-1
Carbon	Diffusion coefficient ( $\text{m}^2/\text{sec}$ )	8.3e-13	4.8e-12	2.0e-11

### 3.4.2. Results and Discussions

The initial and boundary conditions of Section 3.2.2 are adopted and repeated. As before, a 10-node quadratic tetragon element was assigned and the same number of elements of air and ligaments are generated as in Section 3.2.1. The contour plots of oxygen concentration at three different exposure temperatures (600, 700, and 800°C) are compared to each other as shown in Figure 3.12. Note that the concentration on the exterior surface reflects the applied boundary condition (0.21, atmospheric concentration). As exposure time increases, oxygen diffusing from the exterior surface results in forming oxygen gradient. Note that as temperature increases, higher concentration distributions are observed since the diffusion coefficient of oxygen in air and ligament reaction rate are proportional to temperature.

Figures 3.13 and 3.14 show the comparison of oxygen concentration and mass flux distribution resulting from two different temperature exposures (600 and 700°C) at  $y/H=0.5$ , respectively. As shown in Figure 3.13 (a), the concentration gradient takes on a “U” shape after 3.3 minutes for both temperatures. However, the reaction rate at 700°C is about four times greater than that at 600°C as seen in Figure 3.13 (a). As a result, higher oxygen concentration is observed at the interior and its distribution becomes a cone shape, as shown in Figure 3.14 (b) and (c).

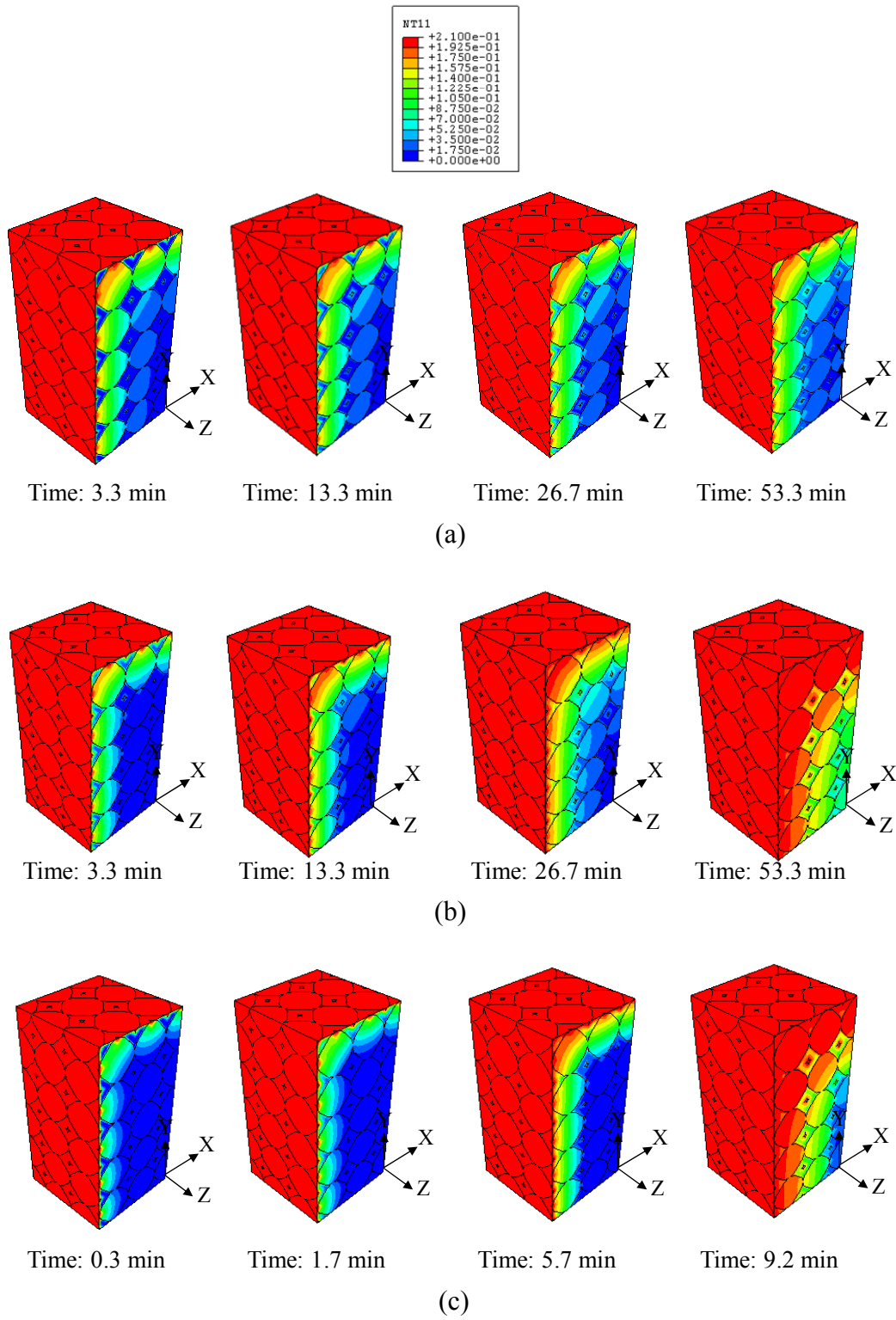


Figure 3. 12. Contour plot of oxygen concentration with increase of exposure time: (a) at 600°C, (b) at 700°C, and (c) at 800°C.

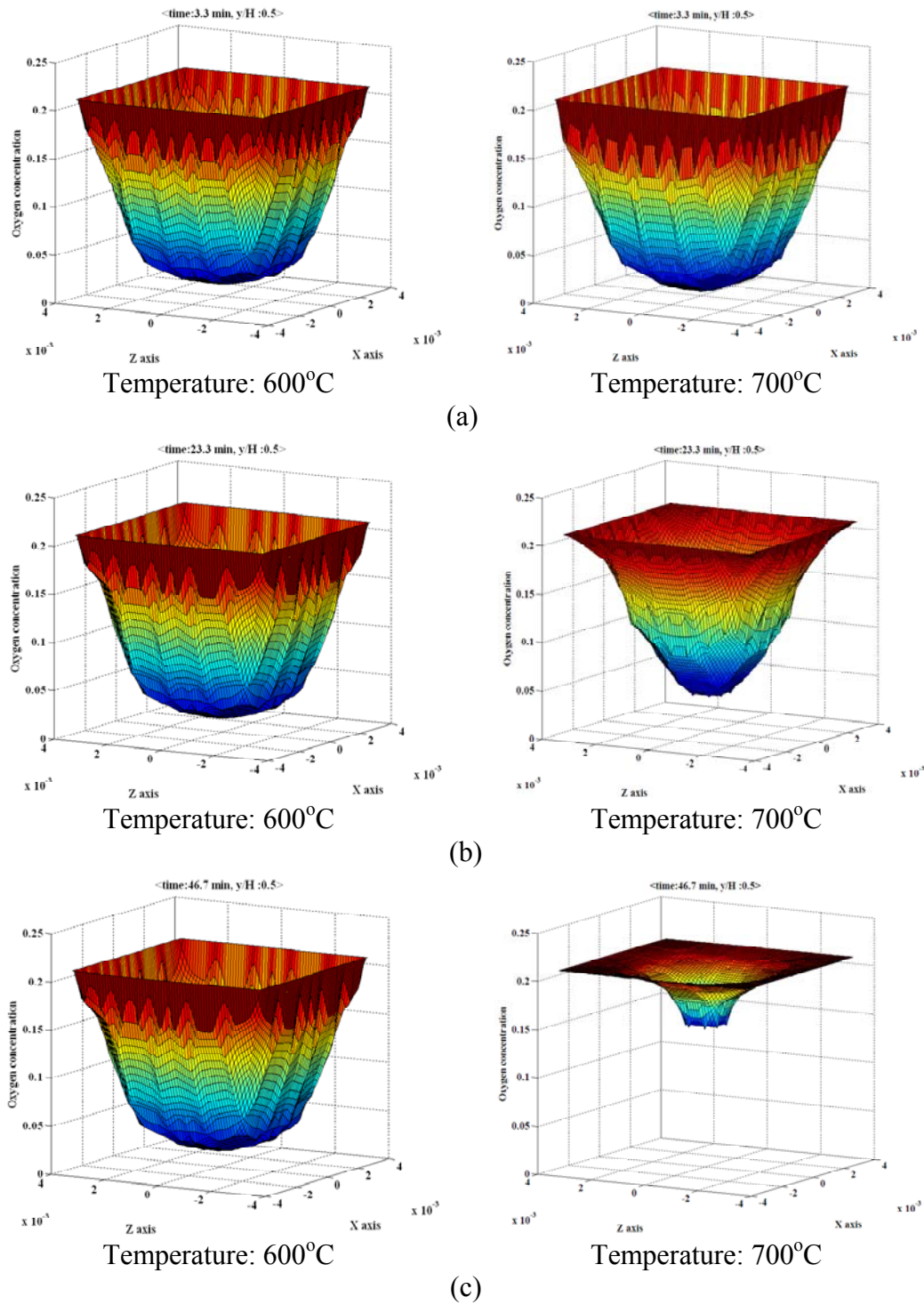
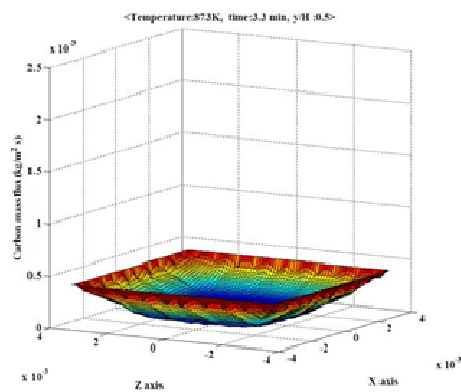
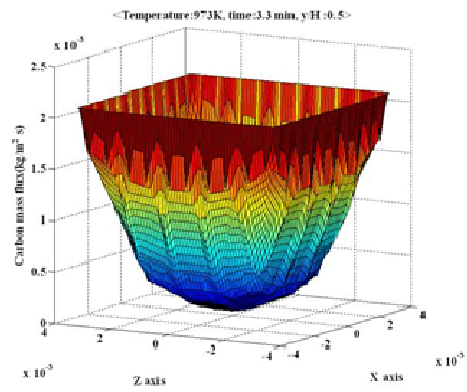


Figure 3. 13. Comparison of oxygen concentration profile at normalized layer ( $y/H$ ) of 0.5 with the increase of exposure time: (a) 3.3 minutes (b) 23.3 minutes, and (c) 46.7 minutes.

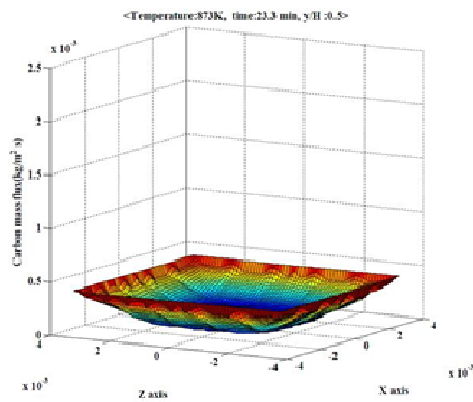


Temperature: 600°C

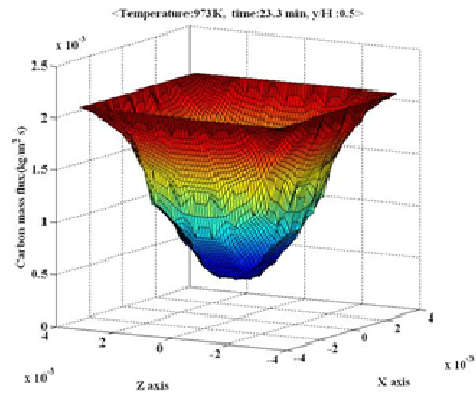


Temperature: 700°C

(a)

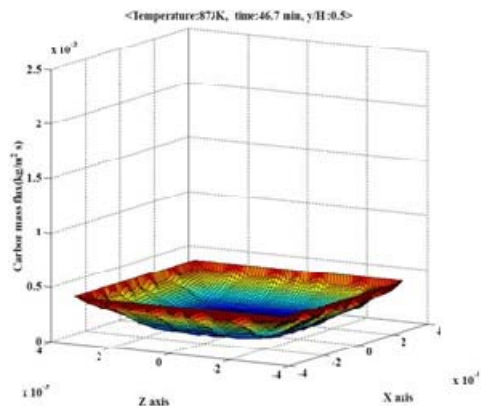


Temperature: 600°C

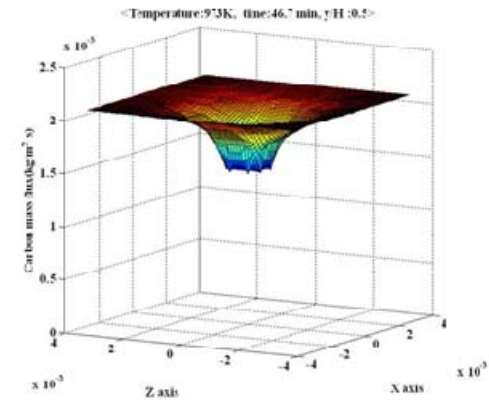


Temperature: 700°C

(b)



Temperature: 600°C



Temperature: 700°C

(c)

Figure 3. 14. Comparison of reaction rate at normalized layer 0.5 as a function of time:  
(a) 3.3 minutes (b) 23.3 minutes, and (c) 46.7 minutes.

### 3.4.3. Evaluating Mass Loss during Oxidation

Mass loss over time is calculated using the carbon reaction rate (Equation 2.11) and ligament geometry as shown Figure 3.15. With the ligament thickness of  $a$  and ligament length of  $l$ , ligament volume ( $V$ ) and ligament surface area ( $A_s$ ) can be expressed as,

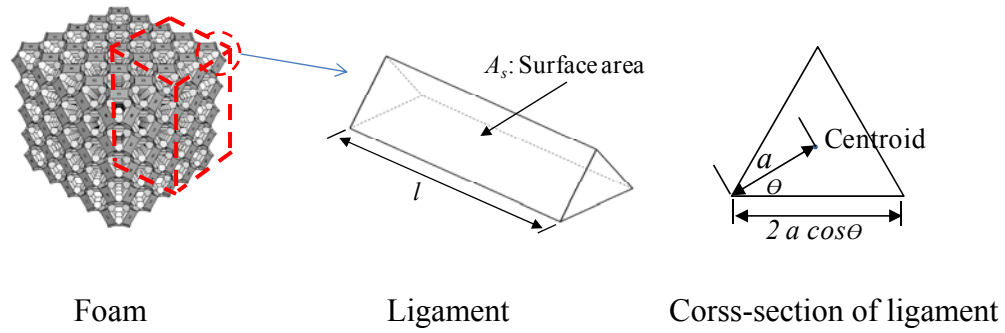


Figure 3. 15. Ligament geometry and cross-section definition.

$$V_{ligament} = 3a^2 \sin\theta \cos\theta l \quad (3.3)$$

$$A_s = 6a \cos\theta l \quad (3.4)$$

Again, carbon reaction rate of Equation 2.11 is represented below,

$$\dot{m}_C'' = \frac{MW_C MW_{mix}}{MW_{O_2}} \frac{P}{RT} A \exp\left[-\frac{E_A}{R_u T}\right] C_{O_2} \quad (3.5)$$

In this analysis, the carbon density ( $\rho$ ) is assumed to be constant. The oxidation is restricted to the ligament surface in contact with air; leading to uniform reduction of the cross sectional area. Thus, the reaction rate ( $\dot{m}_C''$ , kg/m<sup>2</sup>-sec) of ligament is,

$$\dot{m}_C'' = \frac{d}{dt} \left( \frac{m}{A_s} \right) = \rho \frac{d}{dt} \left( \frac{V_{\text{ligament}}}{A_s} \right) = \rho \frac{d}{dt} \left( \frac{3a^2 \sin \theta \cos \theta l}{6a \cos \theta l} \right) \quad (3.6)$$

Substituting Equation 3.5 into 3.6 yields,

$$v = \frac{da}{dt} = \frac{2}{\rho \sin \theta} \frac{MW_C MW_{\text{mix}}}{MW_{O_2}} \frac{P}{RT} A \exp \left[ -\frac{E_A}{R_u T} \right] C_{O_2} \quad (3.7)$$

Note that the reduction rate of ligament thickness ( $v$ ) is a function of oxygen concentration for a given temperature. As shown in Figure 3.16, oxygen concentration at the cell varies with its location as a function of time. From the nodal oxygen concentrations of a single cell, the average time history of oxygen concentration was plotted by taking the average values seen in the left of Figure 3.16 (b). Herein it is assumed the oxygen concentration is of the exponential form  $C_{O_2} = \alpha \exp^{(\beta t)}$ . The parameters  $\alpha_i$  and  $\beta_i$  are determined from average nodal oxygen concentration of cells. For example, using the software OriginPro,  $\alpha_l$  of 0.0115 and  $\beta_l$  of 0.0001second<sup>-1</sup> are found to be the best fit ( $r^2=0.9725$ ) for the data at a given location ( $x/L$  is 0.4~0.8).



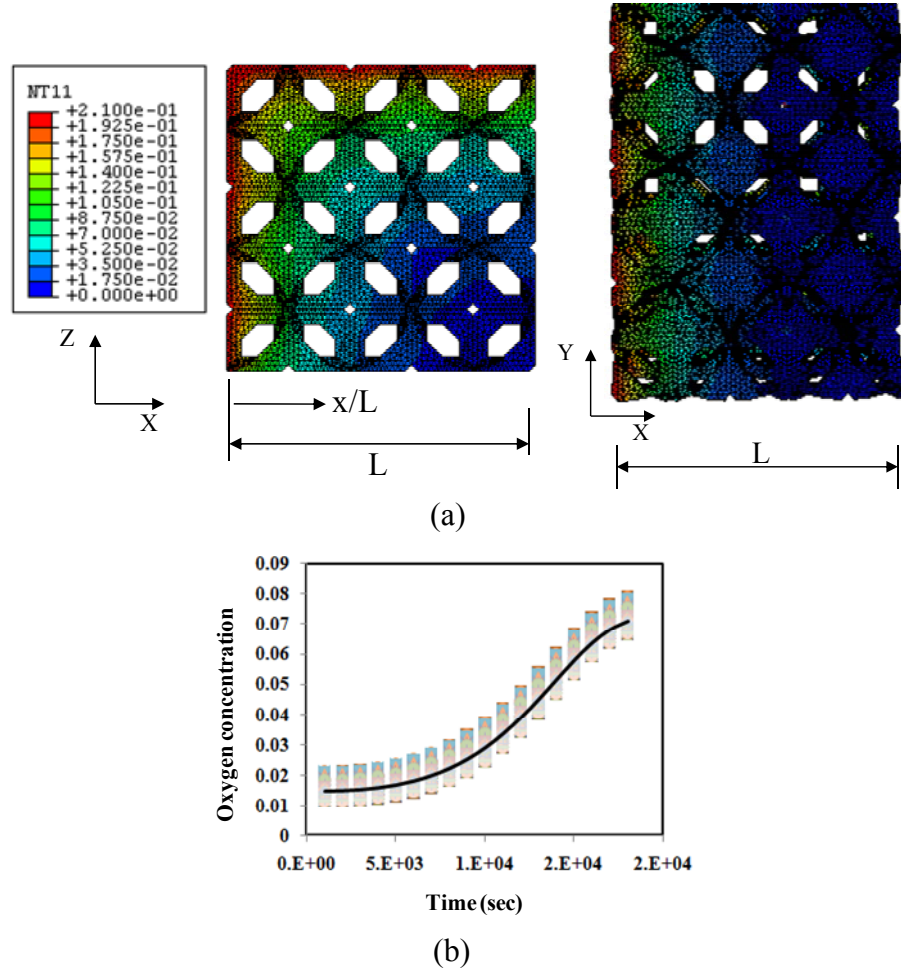


Figure 3. 16. Oxygen concentration vs. time: (a) description for location, (b) nodal oxygen concentrations of single cell at  $x/L$ : 0.4~0.8 and  $z/L$ : 0~0.4 (600°C) at  $y=0$ .

Substituting the exponential representation of oxygen concentration into Equation 3.7, the decrease rate of ligament thickness (oxidation velocity,  $v(t)$ ) can be expressed as,

$$v(t) = \frac{2}{\rho \sin \theta} \frac{MW_C MW_{mix}}{MW_{O_2}} \frac{P}{RT} A \exp \left[ -\frac{E_A}{R_u T} \right] C_{O_2} = C_2 \alpha \exp(\beta t) \quad (3.8)$$

where,  $C_2(= \frac{2}{\rho \sin \theta} \frac{MW_C MW_{mix}}{MW_{O_2}} \frac{P}{RT} A \exp\left[-\frac{E_A}{R_u T}\right])$  is constant for the isothermal condition. Integrating oxidation velocity ( $v(t)$ ) with time, the ligament thickness ( $a(t)$ ) yields,

$$a(t) = a_o - \int_0^t v dt = a_o - \int_0^t C_2 \alpha \exp(\beta t) dt = a_o - C_2 \frac{\alpha}{\beta} [\exp(\beta t) - 1] \quad (3.9)$$

where,  $a_o$  is the initial ligament thickness of 0.2 mm and  $t$  is exposed time in seconds. Using the Equation 3.7 with oxygen concentration function, the changes in the ligament thickness at three different zones are plotted as a function of exposure time in Figure 3.17.

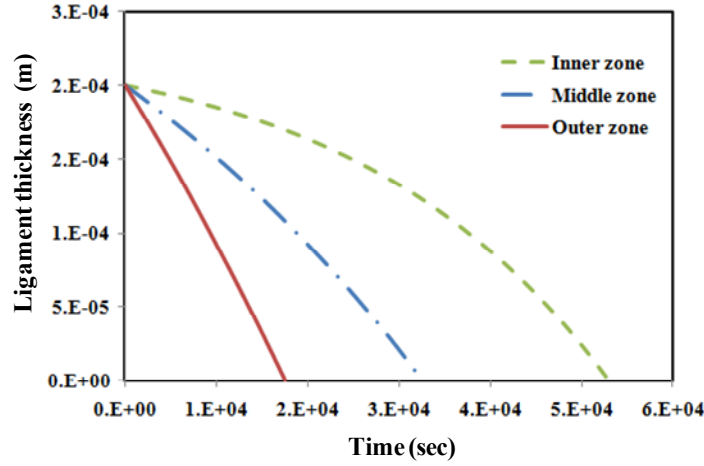


Figure 3. 17. Comparison of change in ligament thickness at three different zones of outer, middle, and inner zone of the cell. Note that the location ( $x/L$ ) of outer, middle and inner zones are 0.0~0.4, 0.4~0.8, and 0.8~1, respectively.

From the porosity expression (Equation 2.5) in Section 2.1.1, the mass of a single cell is,

$$M_{cell} = 3(0.91a)^2 \sin \theta \cos \theta \rho l N_{ligament} \quad (3.10)$$

By substituting Equation 3.9 into 3.10, the mass of a single cell can be expressed as a function of exposure time as,

$$M_{cell}(t) = 3[0.91(a_o - C_2 \frac{\alpha}{\beta}(\exp(\beta t) - 1))]^2 \sin \theta \cos \theta \rho l N_{ligament} \quad (3.11)$$

Total percent mass loss is defined by,

$$\% \text{ Mass Loss} = \frac{\sum M_o^{cell} - \sum M_t^{cell}}{\sum M_o^{cell}} \times 100 \quad (3.12)$$

where  $M_o^{cell}$  is the initial mass of cell and  $M_t^{cell}$  is the cell mass at time  $t$ . The local mass loss of single cells (125) are calculated from Equation 3.9, and the calculated percent mass loss is plotted and compared to the TGA test result in Figure 3.18.

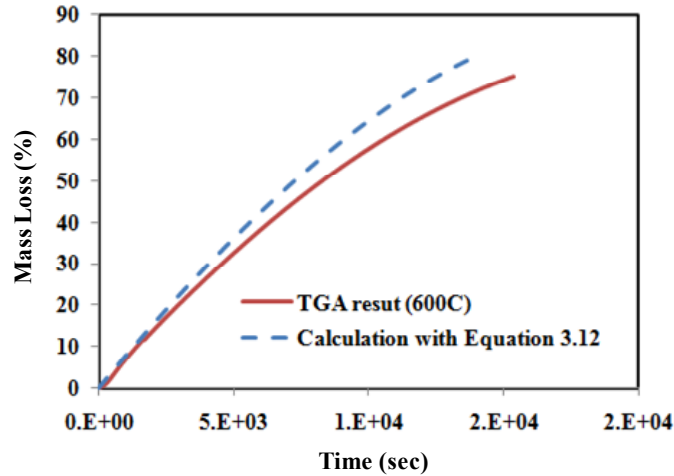
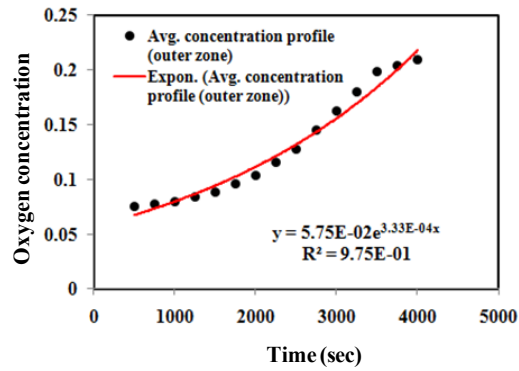


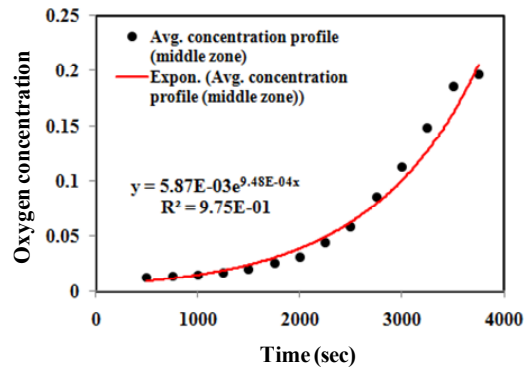
Figure 3. 18. Comparison of TGA result to calculation with Equation 3.12 (600°C).

This approach is repeated at 700°C and 800°C to assess the mass loss of foam as a function of time. Once again, the average oxygen concentration profiles at each location are plotted for each location of the outer, middle and inner zone in Figures 3.19-

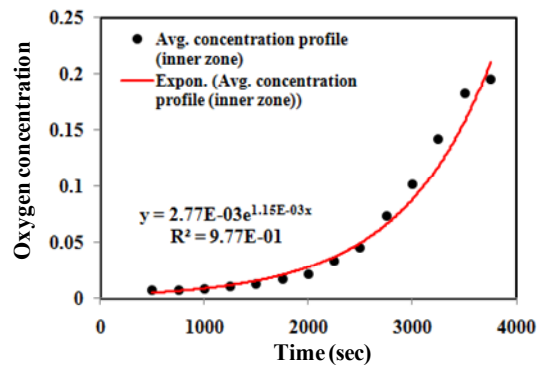
20: Figures 3.19 - 3.20 show the oxygen concentration vs. time curve at 700°C and 800°C, respectively.



(a)

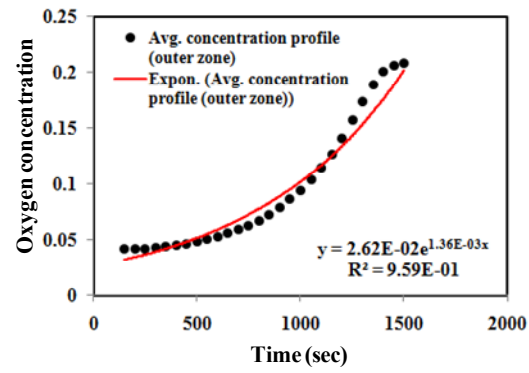


(b)

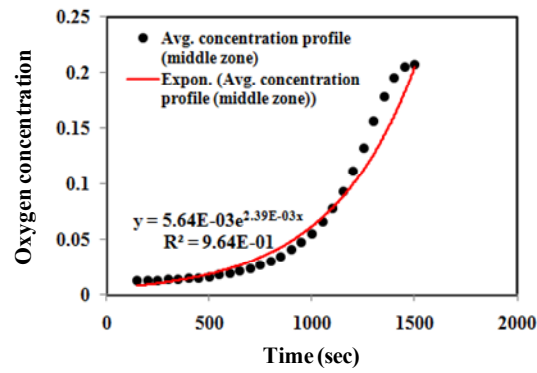


(c)

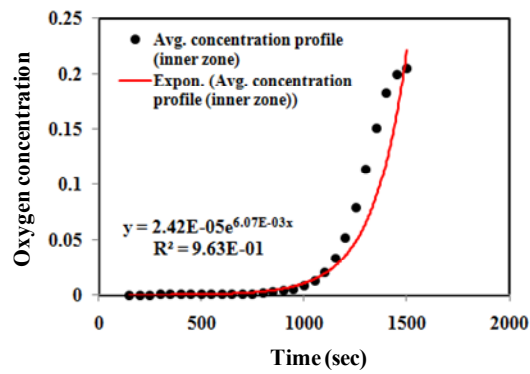
Figure 3. 19. Plot of FEA results (dot data) and exponential expression (red line) of oxygen concentration profile (temperature: 700°C) of foam: (a) at outer (x/L: 0 ~0.4), (b) at middle(x/L: 0.4 ~0.8), and (c) at inner zone(x/L: 0.8 ~1).



(a)



(b)



(c)

Figure 3. 20. Plot of FEA results (dot data) and exponential expression (red line) of oxygen concentration profile (temperature: 800°C) of foam: (a) at outer (x/L: 0 ~0.4), (b) at middle(x/L: 0.4 ~0.8), and (c) at inner zone(x/L: 0.8 ~1).

By substituting the local oxygen concentration function into Equation 3.9, the changes of ligament thickness at three different zones are plotted as a function of exposure time seen in Figure 3. 21. Although exposed to the same temperature of 700°C, the reaction rate coupled with the oxygen concentration gradient results in the different reduction rate of ligament thickness. For example, after 33.3 minutes exposure, the ligament thickness at the outer, middle, and inner zones of model are decreased by 70.4%, 26.2%, and 9.7%, respectively. As plotted in Figure 3.21 (a) and (b), as expected, higher temperature resulted in more rapid oxidation of the ligament. Five minutes of exposure resulted in 7.8 % reduction in the ligament thickness of outer zone at the temperature of 700°C; however, 800°C exposure led to about 49.4 % reduction in the ligament thickness. Temperature is more detrimental to the reduction rate of ligament thickness.

The percent mass losses calculated are larger than that of TGA in both set of temperature conditions. The initial stage of oxidation (mass loss % < 30 %) showed a good match with that of TGA results. However, as exposure time increased, the differences increased in both temperature sets.

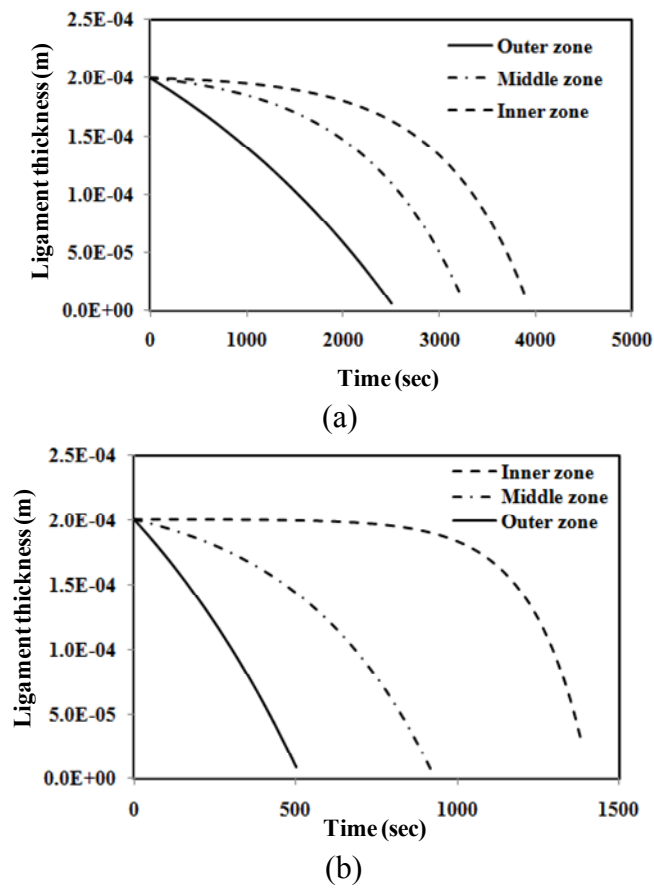


Figure 3. 21. Ligament thickness change at three different zones: (a) 700 °C, (b) 800 °C.

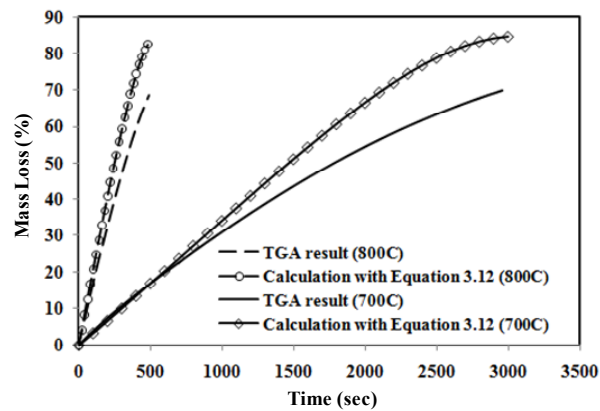


Figure 3. 22. Comparison of TGA results to calculation with Equation 3.12 at 700 °C and 800 °C.

### 3.5. Remarks

Herein the computational analyses are undertaken to obtain the oxygen concentration profile in the carbon foam for evaluating mass loss of carbon foam. Three different porosity levels are investigated such as 83%, 90%, and 95%. It was found that oxygen can penetrate deeper in high porosity foam. As a result, the ligaments of the high porosity foam contact with higher oxygen concentration than that of low porosity foam, which led to higher reaction rates than lower porosity foam.

The influence of temperatures was investigated at 600°C, 700°C, and 800°C. The analysis revealed that although exposed to the same temperature, the reduction rate of ligament thickness varied with its location with respect to the oxygen concentration gradient. For example, after 33.3 minutes exposure at 700°C, the ligament thickness at the outer, middle, and inner zones were decreased by 70.4%, 26.2%, and 9.7%, respectively. In addition, five minutes exposure at 700°C resulted in a 7.8% reduction in the ligament thickness. However, the same exposure time led to a 49.4% reduction in the ligament thickness at 800°C at the same zone. The percent mass losses calculated with Equation 2.13 are larger than that of TGA in both set of temperature cases. However, the mass loss percent below 30 % showed good match with that of TGA results.



## **4. EVALUATING OF CARBON FOAM MATERIAL PROPERTIES**

### **4.1. Overview**

This section presents the computational models used to predict the bulk effective modulus and effective thermal conductivity. First, finite element models are created to evaluate the effective modulus of carbon foam. Here, the multiple-cell models are created by assembling single cells. Linear elastic and isotropic properties of carbon are assigned to the ligaments. The average strain theorem is utilized to calculate the effective modulus, where the nodal reaction forces resulting from the displacement boundary condition are obtained as a function of cell number. The goal is to study the impact of the single cell number and porosity on the effective modulus and effective thermal conductivity.

In addition, coupled thermal-mechanical response for compressive loads are described in TGA test temperatures (600°C, 700°C, and 800°C). First, temperature boundary conditions are introduced to FE models in order to obtain the coefficient of thermal expansion of the bulk foam. Secondly, the temperatures and boundary conditions are simultaneously applied to the model to study the nodal reaction force and stress distributions.

### **4.2. Compressive Response of Carbon Foam**

#### **4.2.1. Problem and Model Description**

A three-dimensional network of the single cell is utilized to characterize the bulk foam morphology as shown in Figure 2.1 of Section 2. Parametric studies are undertaken

to observe the effect of number of cells in RVE and porosity on mechanical response. The goal is to define an appropriate number of cells that resemble the bulk foam prior to oxidation studies. The bulk foam is assumed to be comprised of single cell, thus the multiple-cell models are created by the assembling single cells. Figure 4.1 illustrates representative models for FE analysis. For example, the model in Figure 4.2 (b) consists of 75 single cells ( $5 \times 5 \times 3$ ) and the ligaments on 6 planar quadrilateral faces in a single cell are shared with the adjacent cells. The total number of cells and ligaments for this study are given in Table 4.1.

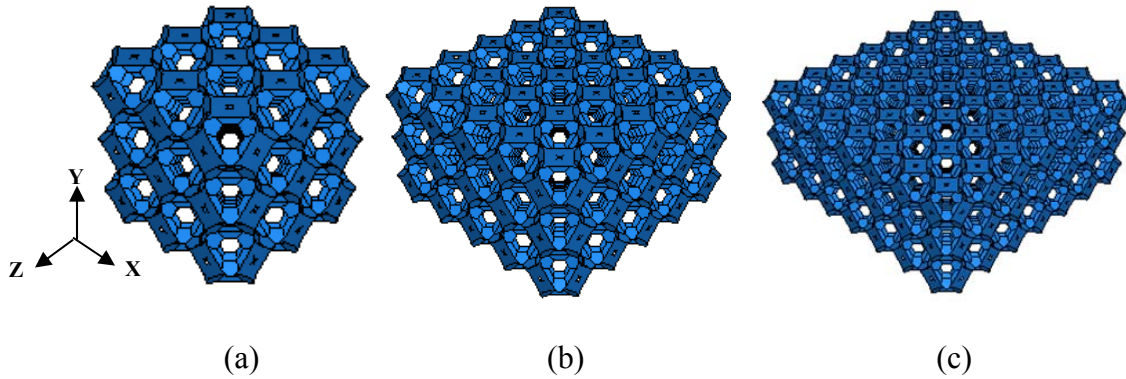


Figure 4. 1. Representations of the foam models: (a)  $3 \times 3 \times 3$ , (b)  $5 \times 5 \times 3$ , and (c)  $7 \times 7 \times 3$ .

Table 4. 1. Total number of single cells and ligaments

	Single cell	$3 \times 3 \times 3$	$5 \times 5 \times 3$	$7 \times 7 \times 3$	$10 \times 10 \times 3$
Total number of single cell	1	27	75	147	300
Total number of ligament	36	648	1800	3528	7200

#### 4.2.2. Boundary and Loading Conditions

A tetrakaidecahedral cell is created using solid element for the ligaments, which is a tetrahedron quadratic element with 10 nodes. Linear elastic and isotropic properties of carbon ( $E$  of 15610 MPa and  $\nu$  of 0.33) are assigned to each ligament as used elsewhere in the literature [35, 36]. As illustrated in Figure 4.2, the nodes that are on  $-y$  plane of the model of  $7 \times 7$  cells are constrained in the  $y$ -direction. Two points are also constrained in the  $x$ - and  $z$ - direction as well to prevent from rotation during the compressive loading. A displacement of 0.042 mm is applied to all nodes on the  $+y$  surface as shown in Figure 4.2; they are displaced an equal magnitude in the negative  $y$ -direction.

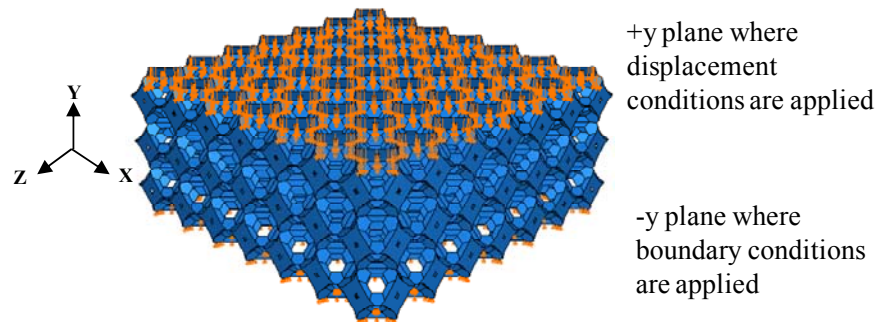


Figure 4. 2. Schematic of displacement boundary conditions. The displacements of -0.042 mm and zero are applied on  $+y$  and  $-y$  surfaces, respectively.

Periodic boundary conditions are applied to the single cell by creating two opposing pairs of surface sets located on the  $\pm x$ -planes and  $\pm z$ -planes as shown in Figure 4.3 (the planes of the single cell that are shared between adjacent cells). All nodes located on these surfaces are constrained to displace the same magnitude as the nodes on the opposing surface. This is accomplished in ABAQUS by creating four master nodes

all at the same point (in this case, at the origin) and using the EQUATION option to assign the same deformation on opposite faces relative to the master node. If the displacements of the nodes on the  $+x$ -plane are  $u_{1,+x}$  and the displacements on the  $-x$ -plane are  $u_{1,-x}$ , then the nodal constraints equations are written as:

$$\begin{aligned} u_{1,+x} - u_{ref,1} &= 0 \\ u_{1,-x} - u_{ref,2} &= 0 \end{aligned} \quad (4.1)$$

where  $u_{ref,1}$  and  $u_{ref,2}$  are the displacements of the master nodes. Since the master nodes have the same displacement,  $u_{ref,1}=u_{ref,2}$ , then the magnitudes on both planes are equal.

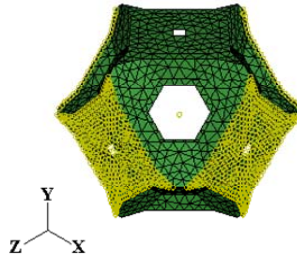


Figure 4. 3. Illustration of the periodic boundary condition on single cell. The nodes applied to periodic boundary conditions are highlighted by yellow color.

#### 4.2.3. Effective Modulus

The average strain theorem [35, 36] is utilized to calculate the effective modulus  $E^*$  as follows:

$$E^* = \frac{\bar{\sigma}}{\bar{\varepsilon}} = \frac{L}{\delta} \frac{\sum P^{nodal}}{A} \quad (4.2)$$

Here, the average strain  $\bar{\varepsilon}$  is calculated using  $\delta/L$  where  $\delta$  is the prescribed displacement of 0.042 mm and  $L$  is 4.2 mm. The average stress  $\bar{\sigma}$  is expressed as

$\sum P^{nodal} / A$  where  $A$  is the total cross-sectional area of model, and  $\sum P^{nodal}$  is the summation of nodal reaction force.

#### 4.2.4. Impact of Cell Number on Effective Modulus

When the displacement on the (+y) plane (1% strain magnitude) is applied on the models in the -y-direction, the sum of resultant nodal reaction forces are given in Table 4.2 as a function of number of cells. With each cross-sectional area and an average strains with respect to multiple cells, the homogenized effective modulus ( $E^*$ ) is calculated using Equation 4.2 and compared as a function of the number of cells in Figure 4.4. As the number of single cell increases, the effective modulus initially increases and then converges to a stable value (695 MPa). When the same displacement is applied on single cell with periodic boundary conditions on  $\pm x$ -planes and  $\pm z$ -planes, the summation of the resultant nodal reaction forces on the +y-surface leads to -13.80 N. Similarly, calculated effective modulus using Equation is 704 MPa. This value shows good match with that of the 10 x 10 x 3 size-model (695 MPa).

Table 4. 2. Total reaction force in different number of single cell

Total number of single cell	1	27	75	147	300
Total reaction force (N)	-10.85	-112.38	-332.97	-665.16	-1362.62
Cross sectional area (mm <sup>2</sup> )	1.96	17.64	49.0	96.04	196

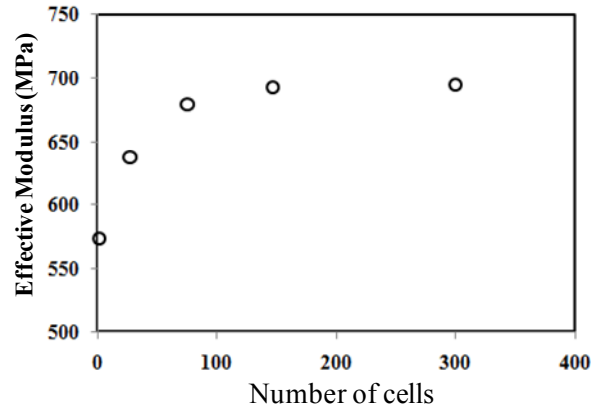


Figure 4. 4. Impact of the number of single cells on effective modulus.

The displacement fields in the x-direction and z-direction of the models are shown in Figure 4.5 (left figure  $u_x$  and right figure  $u_z$ ). In the case of a single cell, locally distorted deformation was observed on both  $\pm x$ -planes and  $\pm z$ -planes due to absence of the adjacent cell (Figure 4.5 (a)). However, in the case of the multiple cells, most of single cells showed uniform deformation except at the edges as seen in Figure 4.5 (b). The single cell with periodic boundary condition showed uniform deformation in x- and z-direction as shown in Figure 4.5 (c). Note that the total expansion in the x-direction is 0.0042 mm and occurred uniformly throughout the given x-y plane. The same total expansion of 0.0042 mm occurs in the z-direction as well. The lateral strain ( $\epsilon_{xx}$ ) in the x-direction is calculated as  $\epsilon_{xx} = u_x / L_o$ , where  $u_x$  is the expansion in the x-direction,  $L_o$  is the initial length of model. Figure 4.6 shows the variations of the lateral strains ( $\epsilon_{xx}$ ) as a function of the number of cells. It is seen that the lateral strain ( $\epsilon_{xx}$ ) of a single cell is  $1.01e^{-2}$ . However, as the number of cells increases, the lateral strains ( $\epsilon_{xx}$ ) decrease and then converge to a stable value. Note that the lateral strain of 10 x 10 cells is  $3.31e^{-3}$ ,

indicating this value is close to that of single cell with periodic boundary conditions ( $3.30e^{-3}$ ): plotted with red line in Figure 4.6. These x- and z-displacements of single cell with periodic boundary conditions are used to calculate the effective Poisson's ratios  $\nu_{yx}^*$  and  $\nu_{yz}^*$  using the relationships of  $-\bar{\varepsilon}_x/\bar{\varepsilon}_y$  and  $-\bar{\varepsilon}_z/\bar{\varepsilon}_y$ , respectively, where the average strains are used. The value of both  $\nu_{yx}^*$  and  $\nu_{yz}^*$  are calculated to be 0.30.

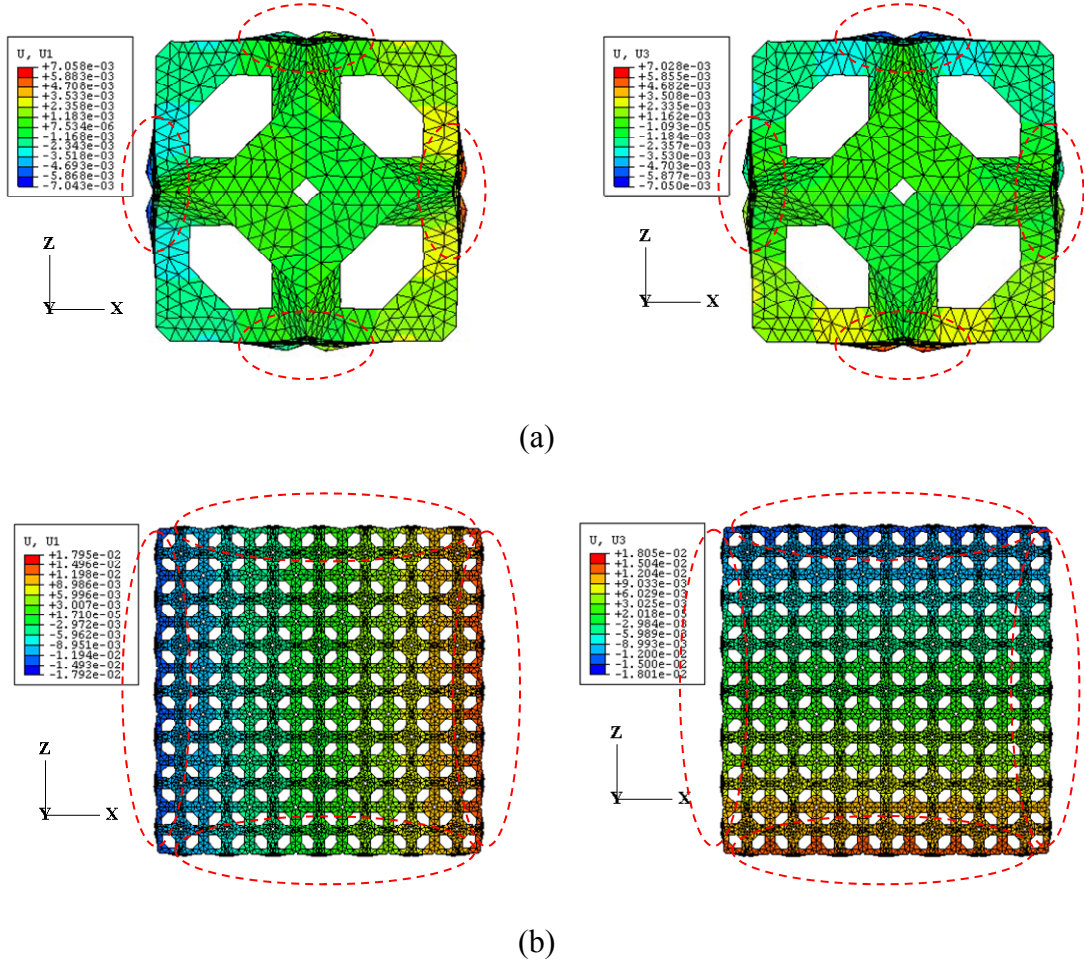
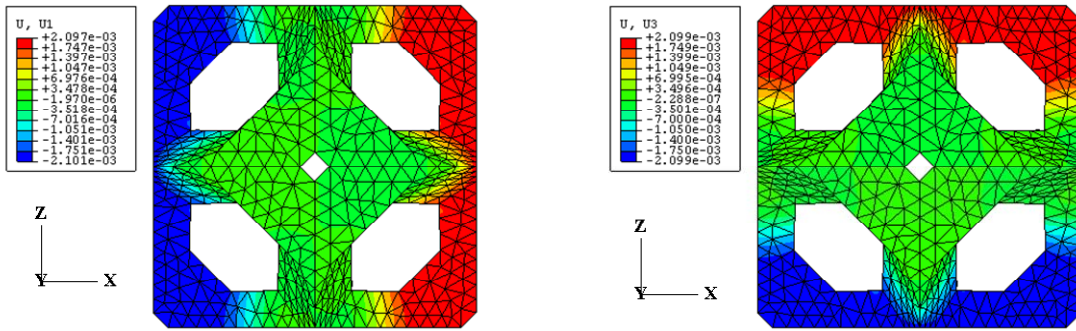
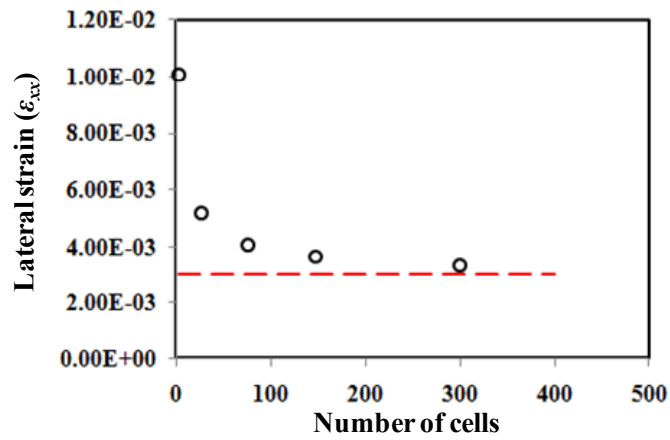


Figure 4. 5. Contour plot of the x- and z- displacements: (a) single cell, (b) 7 x 7 cell, and (c) single cell with periodic boundary condition.



(c)

Figure 4. 5. Continued.

Figure 4. 6. Plot of lateral strain ( $\epsilon_{xx}$ ) as a function of number of cells.

The contour plot in Figure 4.7 illustrates the global stress of single cell with periodic boundary conditions. As highlighted by the arrows, the maximum compressive stress ( $\sigma_{yy}$ ) of 535 MPa occurs around the pore. The maximum tensile stress ( $\sigma_{xx}$ ) of 318 MPa is observed around the pore.



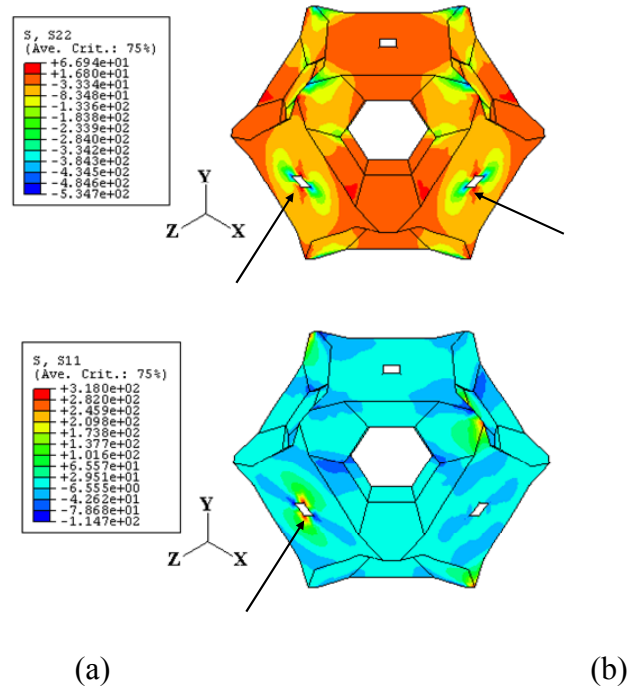


Figure 4. 7. Contour plot of stress distributions of a single cell with periodic boundary condition: (a)  $\sigma_{yy}$  and (b)  $\sigma_{xx}$  (MPa)

The maximum compressive strength of the bulk foam is reported as 8.3 MPa in the manufacture's data sheet [45]. The allowable maximum load was calculated from the relationship of the total load and the cross-sectional area. With the cross-sectional area of  $1.96 \text{ mm}^2$ , the allowable maximum load is calculated to be -16.28 N. The displacement corresponding to the maximum load is 0.0154 mm, indicating the allowable global strain is 0.0112 or 1.12%. As presented in Figure 4.4 and 4.6, as the number of cells increases, the effective modulus ( $E^*$ ) and lateral strain ( $\epsilon_{xx}$ ) are converged to the stable values. Although it is seen that there are differences between the effective modulus of  $10 \times 10$  cells and single cell with periodic boundary condition by 1.27 % (effective modulus) and 3.23 % (lateral strain),  $10 \times 10$  cells model is taken as the RVE for the bulk foam.

#### 4.2.5. Impact of Foam Porosity on Effective Modulus

One of the important characteristics of cellular materials, as mentioned before, is its relative density ( $R$ ) as expressed in Equation 2.5b. The bulk properties of the foam are proportional to its relative density ( $R$ ). These relationships are widely based on empirical formulations. Some closed-form solutions are developed to predict the stiffness of open cell foams [31-36]. In this study, carbon foam with various porosity (95, 90, 83%) are simulated with FEA models to calculate its effective modulus. Periodic boundary conditions, as described in Section 4.2.3, are applied to single cell. The Young's modulus ( $E$ ) and Poisson's ratio ( $\nu$ ) of the carbon ligament are, respectively, taken to be 15.61 GPa and 0.33 as done in the previous analysis in section 4.2.5. Similarly, a displacement boundary condition is applied to all nodes on the +y surface of the single cell. Its magnitude is 0.014 mm, which is equivalent to 1% strain in the y-direction. Once again, the average strain theorem is utilized to calculate the effective modulus as described in section 4.2.4.

The effective modulus ( $E^*$ ) as a function of the relative foam density ( $R$ ) is illustrated in Figure 4.8, and compared to the predictions of two models in the literature [2, 36]: note that the plot with “circle” presents the results of FEA [2] and “triangle” is the result of closed form solution [36]. The plot with “star” presents the result of Sarzynski's result (the foam geometry from micro-CT scanned image). The  $E^*$  predictions are very close for the low-density foams ( $R < 0.1$ ). However, for the high-density foams (with  $R > 0.1$ ), discrepancies between these models increase as the relative density of foam increases.

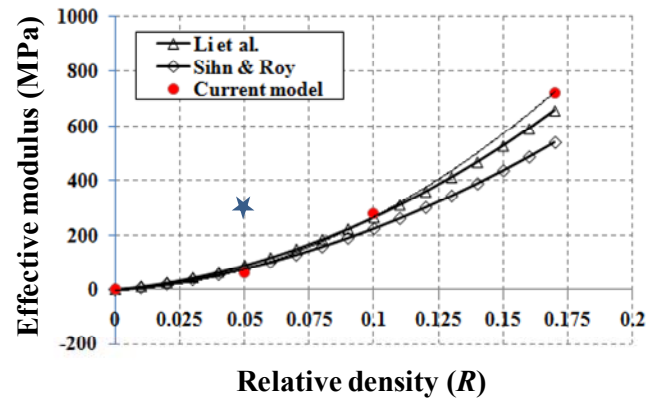


Figure 4. 8. Effective modulus vs. relative density.

### 4.3. Thermal Conductivity of Carbon Foam Microstructure

#### 4.3.1. Problem and Model Description

In addition to mechanical characteristics, thermal response of carbon foam is one of the important factors in many applications. For example, in carbon foams produced from mesophase pitch precursor, high thermal conductivities are achieved by subjecting the foams to post-foaming heat treatments. However, in foams generated from alternate precursors, including coal or polymers, graphitization is not possible and these foams remain insulated [4, 5, 11]. It is noted that the properties (modulus and Poisson's ratio) of air (pore) volume do not influence the mechanical stiffness; however, air conductivity must be considered in the thermal response since the air (pore) volume charges high portion in foam geometry. Generally, the thermal conductivity of foam can be thought of as having three contributions if radiation is neglected [31]:

$$k_e = k_{ligament} + k_{air} + k_{convection} \quad (4.3)$$

where,  $k_e$  [W/m-K] is effective thermal conductivity,  $k_{ligament}$  and  $k_{air}$  are conduction through ligament and conduction through pore, respectively.  $k_{convection}$  is convection within the cells. However, convection is important only when the Grashof number (which describes the ratio of the buoyant force driving convection to viscous force) is greater than about 1000. The Grashof number is defined by [31],

$$Gr = \frac{g\beta\Delta T l^3 \rho^2}{\mu^2} \quad (4.4)$$

where,  $g$  is gravity acceleration,  $9.81\text{m/s}^2$ ,  $\beta$  is the volume coefficient of expansion for the gas (for an ideal gas,  $\beta=1/T$ ),  $\Delta T$  is the temperature difference across one cell,  $l$  is the cell size,  $\rho$  is the density of air, and  $\mu$  is dynamic viscosity of gas, respectively. Here, the contribution term by the pore is lower because the Grashof number is much smaller ( $<30$ ) than 1000 within the temperature range of interest (25-1300°C).

Although generally the pore conductivity is lower than the carbon ligament [11], the pore conductivity term may not be neglected due to its high volume fraction in the foam. Therefore, the effective foam conductivity is simplified as,

$$k_e = k_{ligament} + k_{air} \quad (4.5)$$

Here, the carbon foam microstructure is also assumed to be comprised of periodic tetrakaidecahedra single cells. In order to study the impact of pore conductivity on the effective foam conductivity, both pore and ligament volumes were modeled as shown in Figure 4.9. The results of the effective conductivity were compared to the result of micro-CT image with 95% porosity [11]. Note that the same number of single cells is created for the purpose of comparison with micro-CT image.

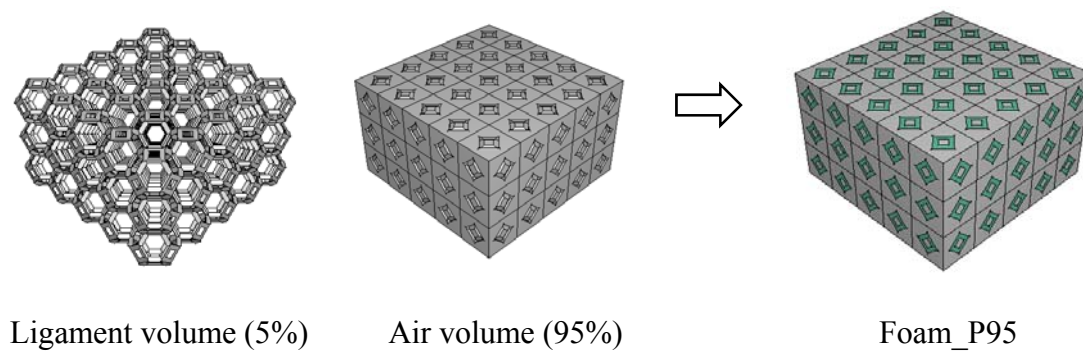


Figure 4. 9. Illustration of foam model composed 5 x 5 x 3 cells.

#### 4.3.2. Element Properties and Boundary Condition

Two volumes are merged with the assumption of perfect interfaces between the ligament volume and the air (pore) volume and meshed with the 10-node quadratic tetrahedron element (DC3D10). Total number of elements for the ligament and air (pore) are 194,939 and 236,303, respectively. Isotropic conductivity of carbon of 0.085W/m-K was assigned to the ligaments. [11]. Temperature dependent conductivity was assigned to the air volume (0.02 - 0.08 W/m-K). Note that thermal conductivity of air, is calculated from the polynomial curve, corresponding to the data set for 100-1600 K in reference

[48]. As illustrated in Figure 4.10, the temperature of 300K is applied to all nodes on the  $-y$  surface and 1300K is applied to the top surface. The magnitude of temperature difference is 1000K in the foam model.

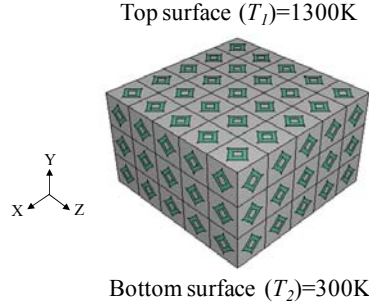


Figure 4. 10. Illustration of temperature boundary conditions on the foam model.

#### 4.3.3. Evaluation of Effective Thermal Conductivity

To calculate effective thermal conductivity, volume weighted heat flux vector is identified at each integration point [11].

$$\vec{q}_w^{\text{int}} = \vec{q}^{\text{int}} V^{\text{int}} \quad (4.6)$$

where,  $\vec{q}^{\text{int}}$  and  $V^{\text{int}}$  are heat flux vector at integration point and integration volume, respectively. The total heat flux vectors for the model are calculated as the sum of the individual volume weighted heat flux vectors. The total volume, both ligament and air phases, is used to calculate the average heat flux as given in Equation 4.7,

$$\vec{q}_{\text{average}} = \frac{\sum \vec{q}_w^{\text{int}}}{V^{\text{ligament}} + V^{\text{air}}} \quad (4.7)$$

Utilized to define the average heat flux and the applied temperature gradient, the effective thermal conductivity in Equation 4.8 as,

$$\bar{k} = q_{average} \frac{dy}{dT} \quad (4.8)$$

#### 4.3.4. Impact of Pore Conductivity on Effective Thermal Conductivity

The effective conductivities are listed in Table 4.3 for the temperature difference ( $\Delta T=1000$ ). When air conductivity is neglected, the value of effective thermal conductivity ( $k^*$ ) predicted by the current model and the value with the micro-CT X-ray scanned model [11] are same. This indicates that although the geometric features between these two models are different, effective thermal conductivity calculated from the volume weighted heat flux vector is similar since they have an identical porosity of 95%. The effective thermal conductivity with the incorporating air conduction is calculated to be 0.0352 W/m-K using Equation 4.8, which is considerably higher.

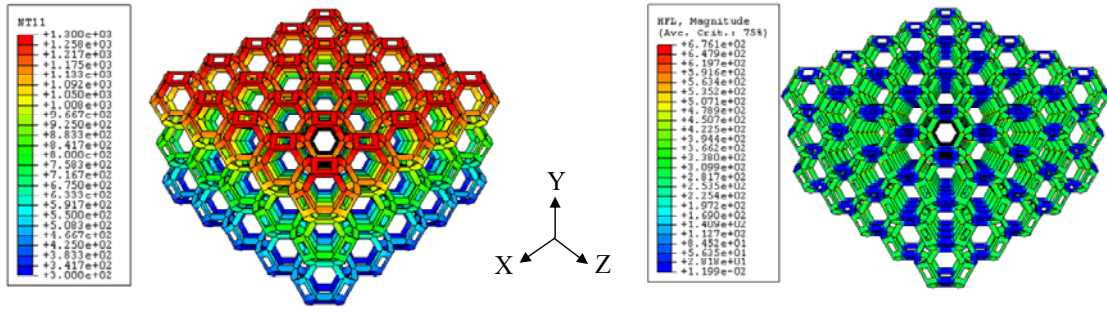
Table 4. 3. Effective thermal conductivities with and w/o air conductivity,  $W/m-K$

	Air conductivity	Ligament conductivity[48,50]	Effective foam conductivity
Sarzynski's model [11]	0	0.085	0.0012
Idealized foam model (5 x 5 x 3)	0	0.085	0.0012
	0.02-0.08	0.085	0.0352

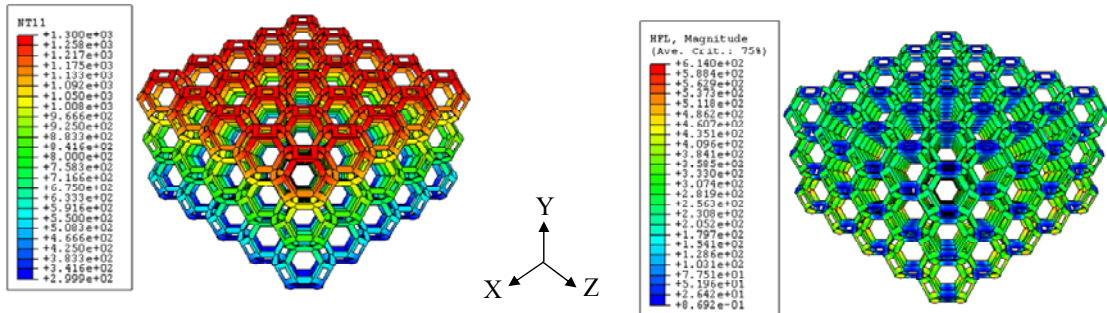
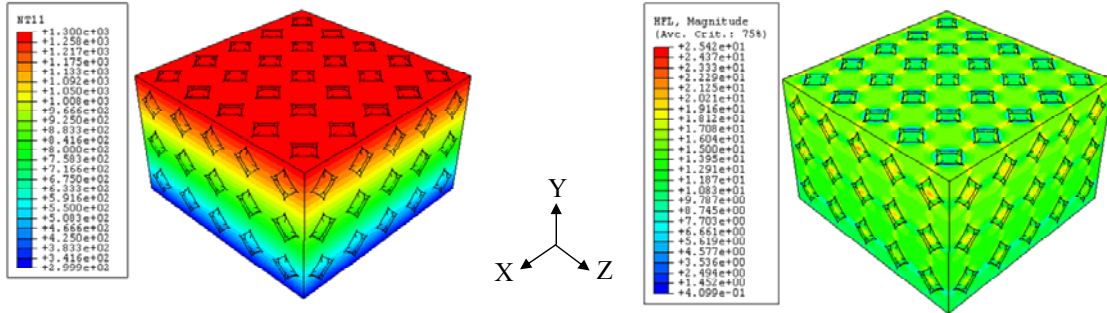
The contours plot of temperature and heat flux is presented in Figure 4.11 where the ligament volume and air volume are presented separately for the purpose of comparison. Note that the maximum and minimum temperature located on the  $+y$ -surface and  $-y$ -surface are 1300 and 300 K matching the applied boundary condition. Also, note that the majority heat flux in the air volume is smaller than that of the ligament by one order of magnitude. This is expected since its conductivity is lower than the ligament.

The effect of air conduction on the temperature gradient and the heat flux are presented in Figure 4.12. First, when air conduction is neglected, the temperature gradient is perpendicular to the ligament direction since only the ligament can play a role in the heat flux from the  $+y$ -surface (high temperature) seen in left contour of Figure 4.12 (a). As a result, heat flux concentration is observed around the corner of ligaments, indicated by the arrows in Figure 4.12 (a). However, in the case of air conduction, the temperature gradient is perpendicular to  $y$ -direction due to the contribution of air conduction seen in Figure 4.12 (b). Therefore, unlike the heat flux contour plot in Figure 4.12 (a), no heat flux concentration is observed at the corner.





(a)



(b)

Figure 4. 11. Contour plot of temperature distribution and heat flux: (a) w/o air conduction, (b) with air conduction.

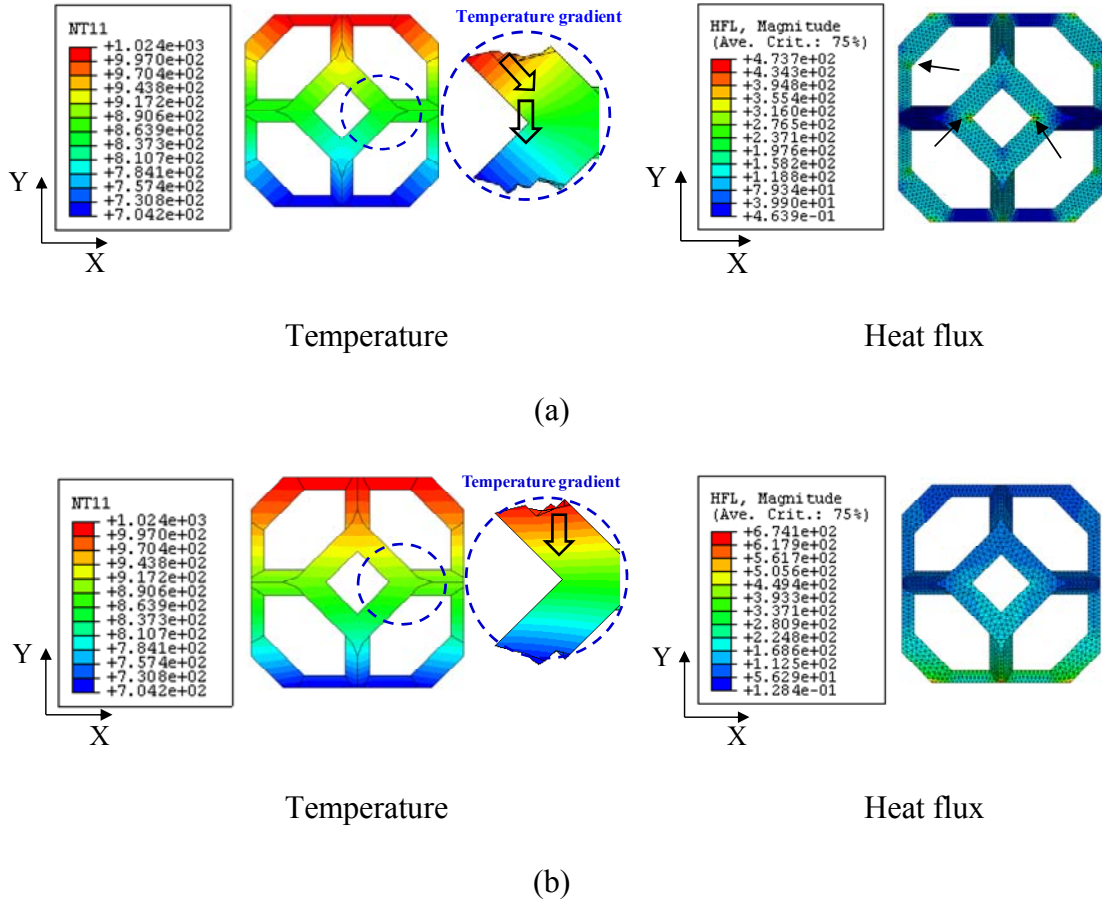


Figure 4. 12. Contour plot of temperature gradient and heat flux in single cell at middle layer: (a) w/o air conduction and (b) with air conduction.

#### 4.4. Coupled Thermo-Mechanical Behavior

##### 4.4.1. Problem and Model Description

Although carbon foam has garnered more attention due to its low coefficient of thermal expansion [11], the residual stress may play an important role in a coupled thermo-mechanical conditions. When carbon foam experiences temperature change, stress develops if the thermal expansion is constrained. Herein the bulk foam model of  $10 \times 10 \times 3$  cells is engaged to obtain the coefficient of bulk thermal expansion and to

investigate the residual thermal stress associated at 600, 700, and 800°C in inert atmosphere. First, the temperature is applied to evaluate coefficient of bulk thermal expansion without constraints. Secondly, the temperatures and constraints are simultaneously applied to the model to study stress distributions and allowable bulk strain. Figure 4.13 shows the illustrations of bulk foam model for coupled thermal-mechanical field.

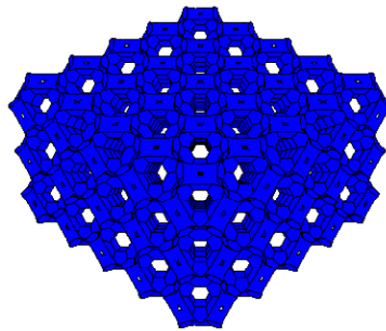


Figure 4. 13. Illustration of the bulk foam model (5 x 5 x 3).

#### 4.4.2. Element Properties and Boundary Conditions

Linear elastic properties of carbon ( $E$  of 15610 MPa and  $\nu$  of 0.33) and the coefficient of thermal expansion (CTE of  $2e^{-6}$  1/K) are assigned to the ligaments [11, 35, 36]. The selected element is the 10-node thermally coupled tetrahedron element (C3D10MT). Isothermal conditions are assumed to the ligament elements. The applied temperature differences ( $\Delta T$ ) are 575K, 675K, and 775K, reflecting the TGA tests described in Section 2.3. First, only temperatures are applied to bulk foam model without any constraints to obtain the coefficient of the bulk thermal expansion. Later, the temperature differences ( $\Delta T$ ) and constraints on  $\pm y$ -plane are simultaneously applied to models to investigate stress associated with thermal expansions. Again  $x$ - and  $z$ -

symmetry boundary conditions are applied on the  $-x$ - and  $-z$  plane of model by constraining all nodes on that surface to zero displacement in the  $x$ - and  $z$ -directions ( $u_x = u_z = 0$ ). The details of boundary conditions are illustrated in Figure 4.14.

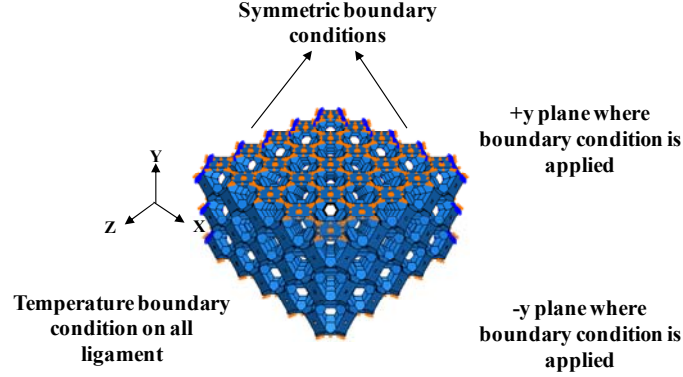


Figure 4. 14. Temperature and boundary conditions.

#### 4.4.3. Coefficient of Thermal Expansion (free expansion at isothermal condition)

When subjected to temperature changes, the displacement of the bulk foam model in the  $x$ - and  $z$ - directions are shown in Figure 4.15. The values in the  $x$ - direction are  $6.038 \times 10^{-3}$  mm,  $7.088 \times 10^{-3}$  mm,  $8.137 \times 10^{-3}$  mm at the temperature difference ( $\Delta T$ ) of 575, 675, and 775K, respectively. The same displacements occur in the  $z$ -direction as well since no constraints are applied on  $\pm z$ -planes. The volumetric thermal expansion coefficient can be expressed as [47],

$$\alpha_v = \frac{1}{V_o} \frac{dV}{dT} \quad (4.9)$$

where,  $V_o$  is the initial volume and  $dV/dT$  is the change of volume with temperature. The calculated volume change is  $0.3588 \text{ mm}^3/\text{K}$ ,  $0.3590 \text{ mm}^3/\text{K}$ , and  $0.3592 \text{ mm}^3/\text{K}$  at the temperatures of  $600^\circ\text{C}$ ,  $700^\circ\text{C}$ , and  $800^\circ\text{C}$ , respectively. With the initial volume of

$208.80\text{mm}^3$ , the coefficient of thermal expansion of bulk foam is calculated to be  $4.51\text{e}^{-6}$   $1/\text{K}$ . When compared to the product data sheet ( $5.0\text{e}^{-6}$   $1/\text{K}$ ) [45], this value is higher by 9.8 %.

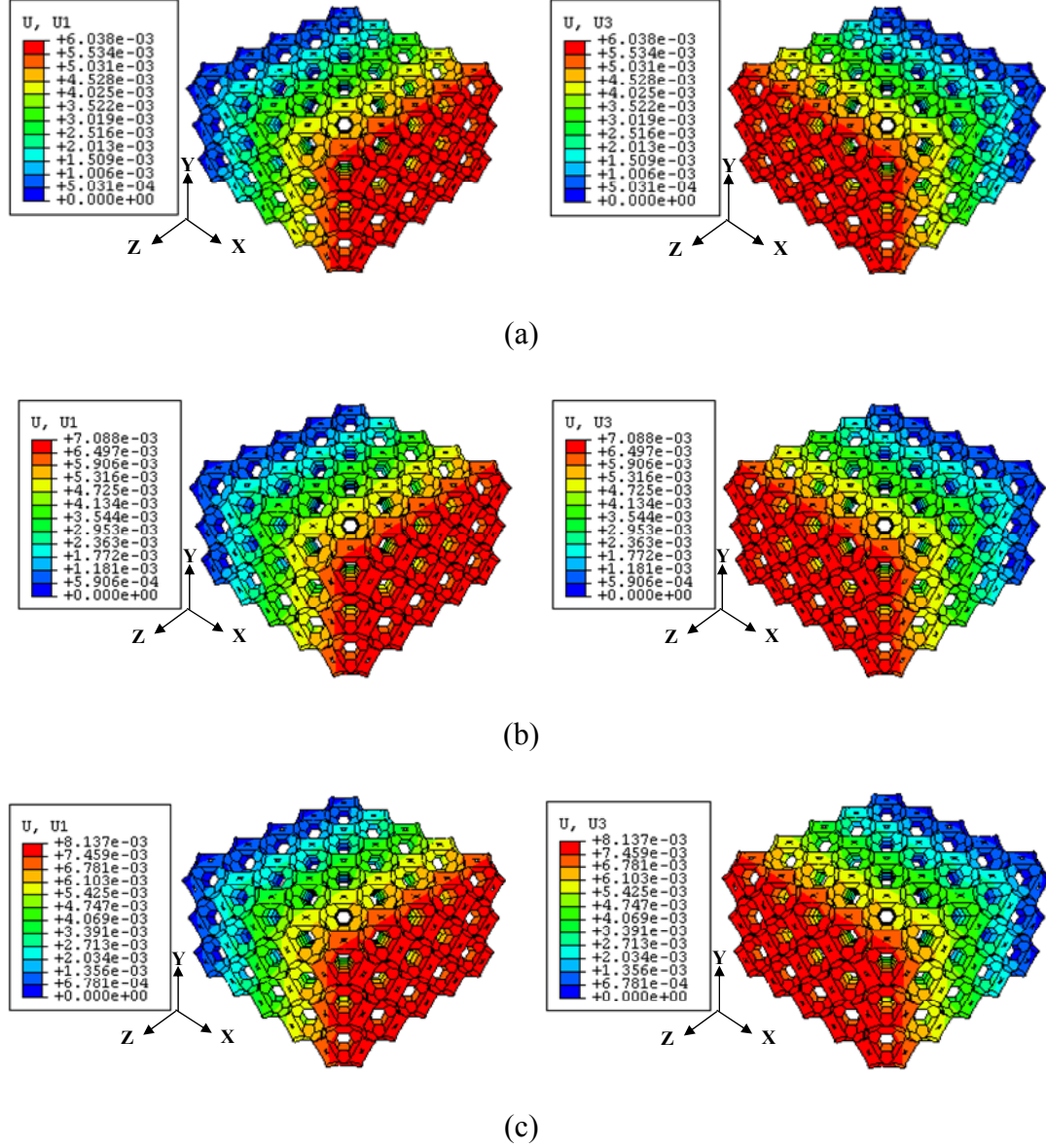


Figure 4. 15. Contour plot of the x- and z-expansion (mm). Note that the expanded values in the x- and z- directions are approximately same: (a)  $\Delta T=575\text{K}$ , (b)  $\Delta T=675\text{K}$ , and (c)  $\Delta T=775\text{K}$ .



#### 4.4.4. Isothermal with Displacement

Figure 4.16 shows the comparison of deformations in x- and z-direction at the temperature of 600°C. When the temperatures and the displacement are simultaneously applied, the total expansion in x-direction is larger than that of free expansion on y-direction. This can be explained that the total expansions are developed by two contributions: one is the expansion by applied temperature and the other is that by Poisson's effect. In this temperature, total deformation is increased by 27.5% when compared to the result of free expansion.

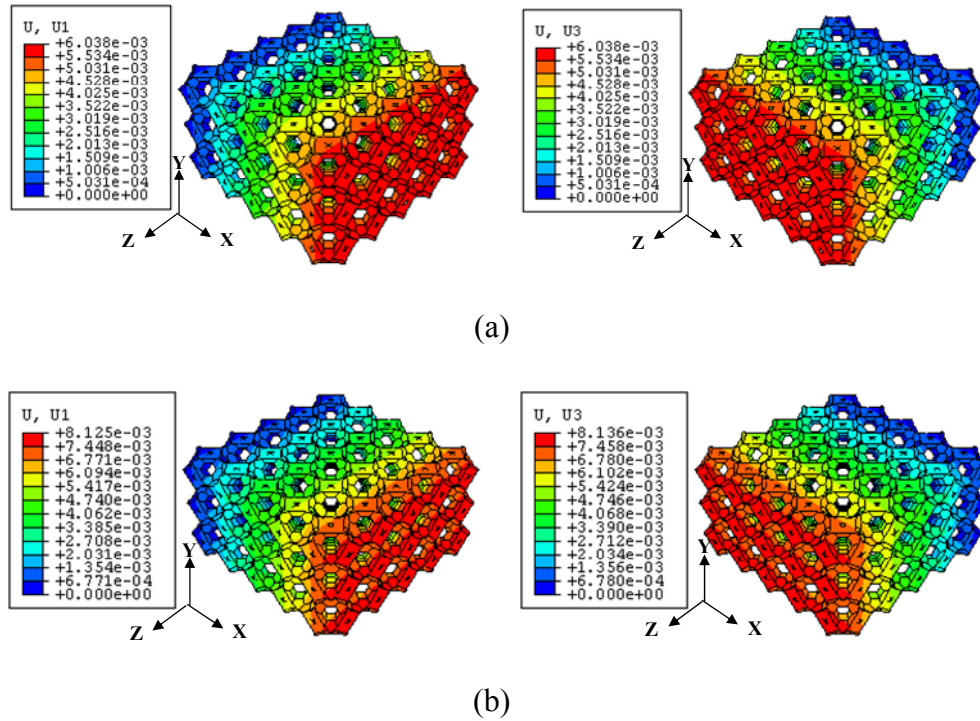
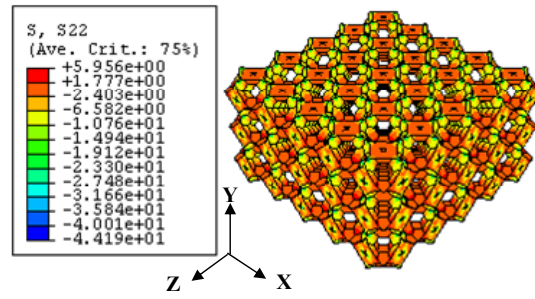


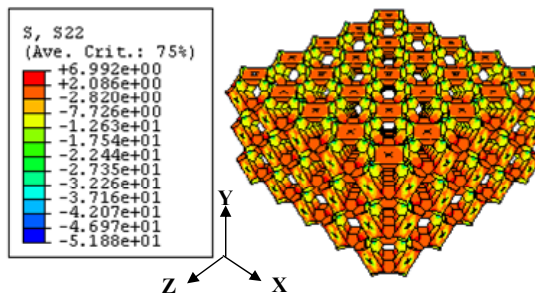
Figure 4. 16. Comparison of deformation in x-direction at the temperature of 600°C: (a) free expansion and (b) boundary condition on +y-surface ( $u_y=0$ ).

Stress distributions in the y- and x-directions are shown in Figure 4.17-18. The contour plots shown in Figure 4.17 present the global stress ( $\sigma_{yy}$ ). The maximum compressive stress occurs in the ligaments that are aligned in the y-direction and are in contact with the adjacent cells. As shown in Figure 4.17 (a)-(c), the maximum stress also increases when temperatures increase. The maximum stresses are 44.2, 51.9, 59.6 MPa at the temperature difference ( $\Delta T$ ) of 575, 675, and 775K, respectively.

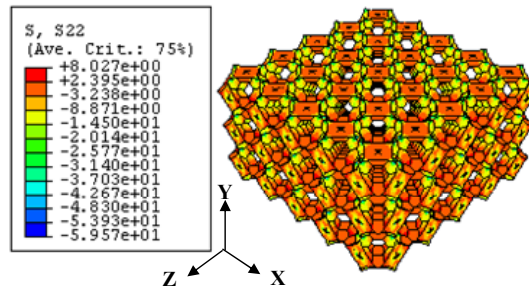
The contour plot in Figure 4.18 shows the transverse stress distribution ( $\sigma_{xx}$ ) at the temperatures of 575, 675, 775K, respectively. The majority stress distributions are tensile mode and as temperature increase, these values also increase due to the thermal expansion and constraints. Similar tensile stresses occur in the z-direction as well since same symmetry boundary conditions are applied. The maximum stresses are observed around the pore due to the thermal expansion and Poisson's effect. The maximum stresses are about 32.7, 38.4, and 44.1 MPa at the temperature difference ( $\Delta T$ ) of 575, 675, and 775K, respectively.



(a)



(b)



(c)

Figure 4. 17. Contour plots of  $\sigma_{yy}$  stress distribution (MPa): (a)  $\Delta T = 575K$ , (b)  $\Delta T = 675K$ , and (c)  $\Delta T = 775K$ .



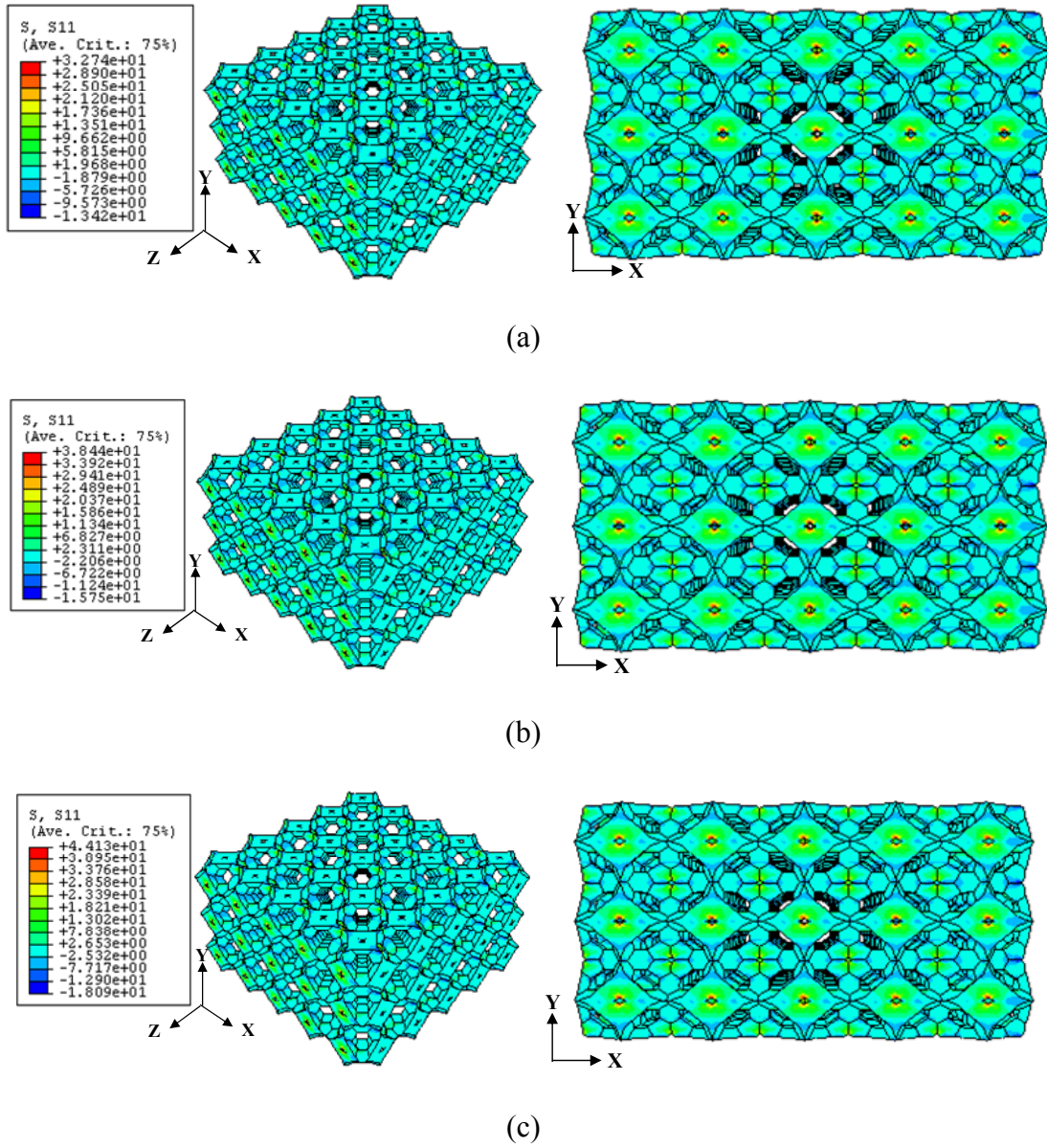
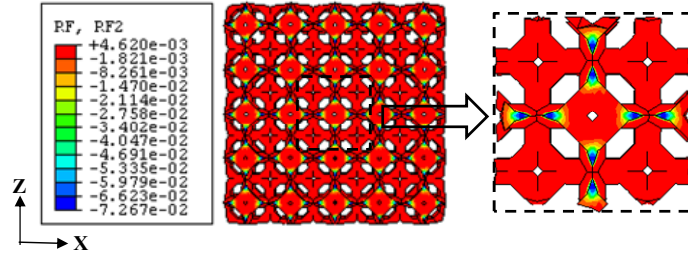


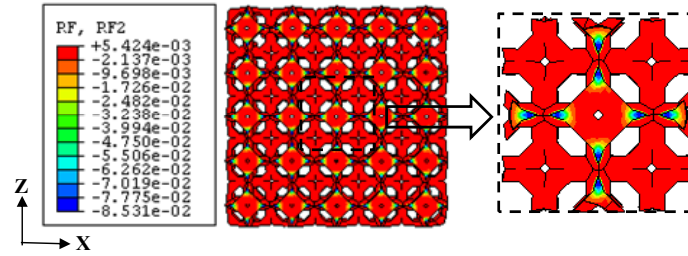
Figure 4. 18. Contour plots of  $\sigma_{xx}$  stress distribution (MPa): (a)  $\Delta T = 575K$ , (b)  $\Delta T = 675K$ , and (c)  $\Delta T = 775K$ .

Figure 4.19 shows the contour plot of nodal reaction forces ( $RF_2$ ) at the temperature of  $600^\circ C$ ,  $700^\circ C$  and  $800^\circ C$ . As expected, the maximum reaction force occurs at the ligaments that are aligned with loading direction. The resultant nodal forces

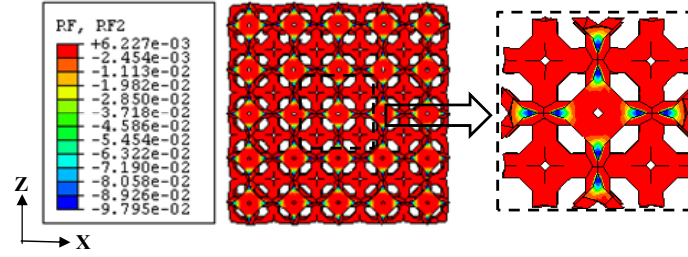
increase with temperature change since the reaction force associated with the thermal expansion. As shown in Figure 4.19 (a)-(c), the maximum nodal reaction force is  $-7.27 \times 10^{-2}$  N at the temperature difference ( $\Delta T$ ) of 575 K, whereas those are  $-8.53 \times 10^{-2}$  N,  $-9.76 \times 10^{-2}$  N at the temperatures differences ( $\Delta T$ ) of 675 K and 775 K. The summation of resultant nodal reaction force at the temperature difference ( $\Delta T$ ) of 675 and 775 K are -37.0 N and -42.51 N, which are increased by 17.4 % and 34.8 %, respectively when compared to that of  $\Delta T$  of 575 K. The maximum compressive strength of the bulk foam is reported as 8.3 MPa in the manufacturer's data sheet [45]. The allowable maximum load was calculated from the relationship of the total load and the cross-sectional area. With the cross-sectional area of  $49 \text{ mm}^2$ , the allowable maximum load is -421.4 N. The displacement corresponding to the maximum load is 0.0471 mm, indicating the allowable global strain in the loading direction is 0.0112. However, smaller displacement may reach the maximum allowable load at the temperature of 600°C due to the residual stress associated by thermal expansion. In this scenario, the displacement of 0.0430 mm leads to the maximum allowable load (-421.4 N), indicating the allowable global strain is decreased by 8.5% when compared to that of 25°C (0.0112 to 0.0103). As temperature increase, the allowable global strains decrease to 0.0101 and 0.010 at temperatures of 700°C and 800°C, respectively, indicating decreases by 9.6 % and 10.7 % when compared to that at 25°C.



(a)



(b)



(c)

Figure 4. 19. Contour plots of nodal reaction force ( $RF_2$ ): (a)  $\Delta T = 575K$ , (b)  $\Delta T = 675K$ , and (c)  $\Delta T = 775K$ .

#### 4.5. Remarks

Mechanical, thermal and coupled thermal-mechanical are considered to evaluate bulk foam properties in inert atmospheric conditions. As the single cell number increases, the effective modulus initially increased and then converged to the stable value, which

was approximately 22.7% greater than that of a single cell without periodic boundary condition. Subsequently different foam porosity (83, 90, 95 %) models were constructed. Effective modulus was evaluated with the average strain theorem present prediction were very good for low-density foam ( $R < 0.1$ ). However, for high-density foams ( $R > 0.1$ ), discrepancies between these models increased with increasing relative density.

In addition to mechanical response, thermal response of carbon foam was simulated incorporating air conductivity. At the ligament-scale, it was observed that heat flux w/o air conduction was parallel to the ligament directions, however, heat flux with air conduction was parallel to the y-direction which was the direction of applied temperature gradient.

In coupled thermal-mechanical response, as temperature difference ( $\Delta T$ ) increased, volumetric expansion increased. The percent of the bulk volume changes were 0.25%, 0.30%, and 0.35 % at the temperature of 600°C, 700°C, and 800°C, respectively when compared to the initial volume of the bulk foam. The coefficient of thermal expansion of bulk foam was calculated to be  $4.51 \times 10^{-6} \text{ 1/K}$  with Equation 4.9. In addition, as temperature increased, the maximum compressive stresses in the y-direction also increased due to the combination of thermal expansion and boundary conditions  $\pm y$ -surfaces. As a result, higher residual stress and resultant nodal reaction forces occurred. The summation of resultant nodal reaction force at the temperature difference ( $\Delta T$ ) of 675 and 775 K are -37.0 N and -42.51 N, which were increased by 17.4 % and 34.8 %, respectively when compared to that at  $\Delta T$  of 575 K.

## **5. CARBON FOAM REPRESENTATIVES: OXIDATION EFFECT**

### **5.1. Overview**

Oxidation of the carbon foam can be documented as morphological observations, such as reduction in ligament thickness, ligament fracture-discontinuity, and pore enlargement as described in Section 2.4. The increase of foam porosity due to mass loss reduces the mechanical stiffness, since the bulk foam modulus is proportional to the relative density [33-36]. Here, the carbon foam model of 5 x 5 cells of Section 4.2, is utilized to investigate the effect of oxidation on bulk modulus. The ligament reduction rates coupled with oxygen concentration are evaluated as a function of time.

By combining the relationships of the porosity-exposure time as described in Section 3 and the porosity-effective modulus as studied in Section 4, the time-dependent effective modulus of bulk foam is simulated as a function of time at the temperatures of 600°C and 700°C. User subroutine (UMAT) in ABAQUS is used to assign the local material stiffness matrix and to update the state of stress during compressive loading. As a result, variations of the reaction force and stress distribution are investigated as a function of location and time.

### **5.2. Evaluation of Oxygen Concentration Profile and Porosity**

#### **5.2.1. Oxygen Concentration Profiles in Bulk Foam**

The bulk foam model of 5 x 5 x 3 cells is engaged to obtain the oxygen concentration profile as a function of time. Similar to the initial and boundary conditions applied in Section 3.2.2, atmospheric oxygen concentration is assumed at the exposure.

Additionally, symmetric boundary conditions were applied to all nodes on x and z surface ( $x=L_1$  and  $z=L_2$ ). The difference from the previous analysis in Section 3 is the two impermeable conditions are applied to all nodes on the top and bottom surface ( $y=0$  and  $y=H$ ) since these two surfaces in contact with the loading bar and fixture are assumed to be protected from oxidation. Figure 5.1 shows details of the model descriptions and applied initial and boundary conditions for the quarter-size model:

Initial condition:

$$C_{O_2}(x, y, z, 0) = 0$$

Two exposure surfaces:

$$C_{O_2}(0, y, z) = C_{O_2}(x, y, 0) = 0.21, \quad \text{at } t > 0$$

Two symmetric surfaces:

$$D \frac{\partial C_{O_2}}{\partial x} \Big|_{x=L_1} = D \frac{\partial C_{O_2}}{\partial z} \Big|_{z=L_2} = 0, \quad \text{at } t > 0$$

Two impermeable surfaces:

$$\frac{\partial C_{O_2}}{\partial y} \Big|_{y=0} = \frac{\partial C_{O_2}}{\partial y} \Big|_{y=H} = 0, \quad \text{at } t > 0$$

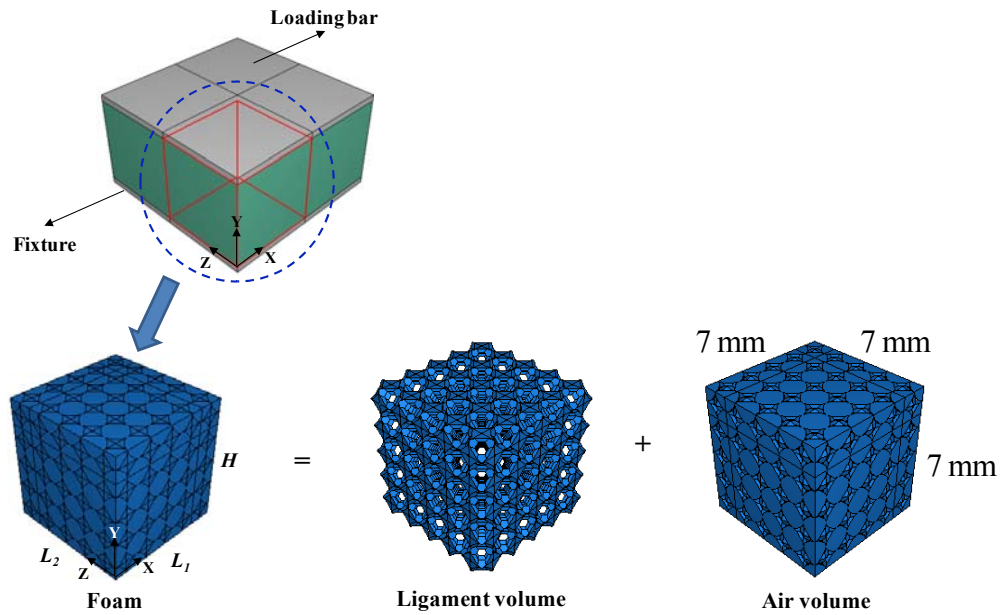


Figure 5. 1. Model schematic.

As a result, the oxygen concentration profiles are identified as a function of time. Note that the oxygen concentration distributions of this model differ from the result in Section 3 since two impermeable boundary conditions are applied on  $+y$ - and  $-y$ -surfaces. For example, the contour plot of oxygen concentration after 50 minutes exposure at the temperature of  $600^{\circ}\text{C}$  is shown in Figure 5.2. The current model shows consistent distribution regardless to the normalized height ( $y/H$ ) due to two impermeable boundary conditions on  $+y$  and  $-y$ -surfaces.

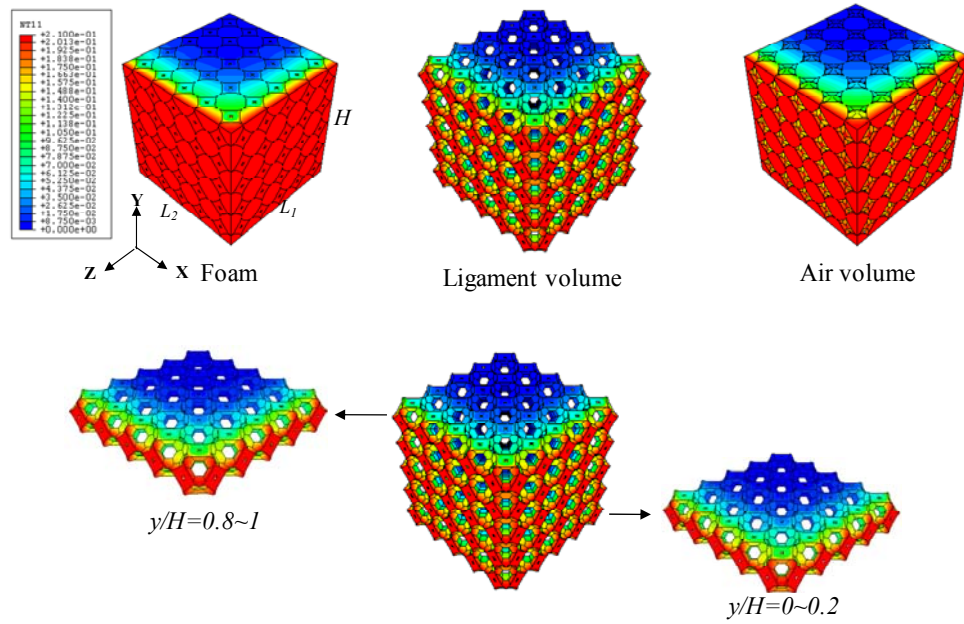


Figure 5. 2. Contour plot of oxygen concentration distribution after 50 minutes elapse at 600°C.

In order to evaluate the oxidation rate, it is necessary to identify the time history of oxygen concentration in model. With the same method as described in Section 3.4.4, the equivalent oxygen concentration of individual cell is determined by taking the average values at each location as a function of time. For example, as seen in Figure 5.3 (b), oxygen concentration distributions of a single cell at the location ( $x/L_1=0\sim0.2$ ) are plotted as a function of time. Note that data points are nodal concentrations of single cell and the line indicates the average oxygen concentration of single cell. Here, it is also assumed that the time history of oxygen concentration is of the exponential form  $C_{O_2} = \alpha_i \exp(\beta_i t)$ , where  $\alpha_i$  and  $\beta_i$  are determined from the average nodal concentration of the individual cell. Using software OriginPro,  $\alpha$  of  $9.73e^{-2}$  and  $\beta$  of  $1.68e^{-5} \text{ second}^{-1}$  are found to be a best fit for the average concentration distributions of cell as seen in



Figure 5.3 (c). The single cells ( $x/L_1 = 0 \sim 0.2$ ) near the exposure surface experience higher oxygen concentration; however, further away, their values are low at initial stage and then increase with the exposure of time. In same manner, the average oxygen concentrations of each cell are plotted as a function of exposure time in Figure 5.3 (d).

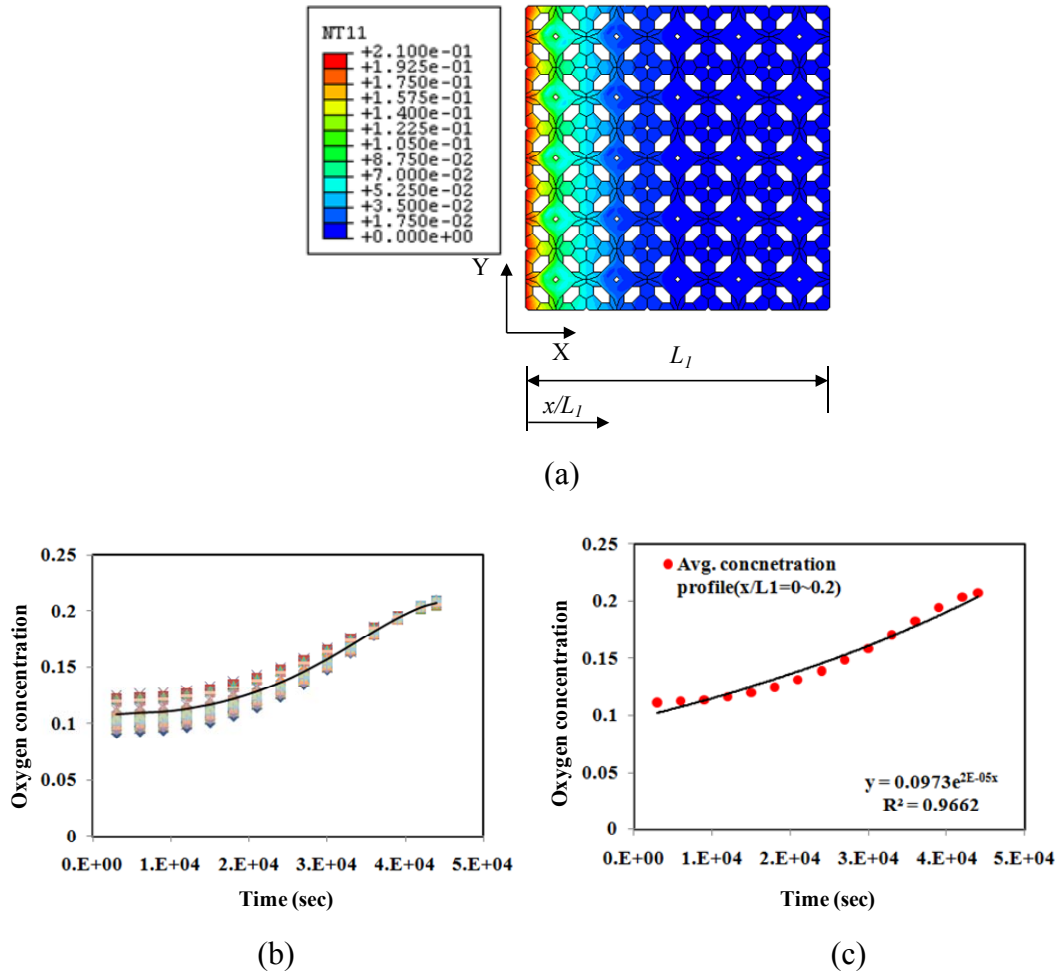
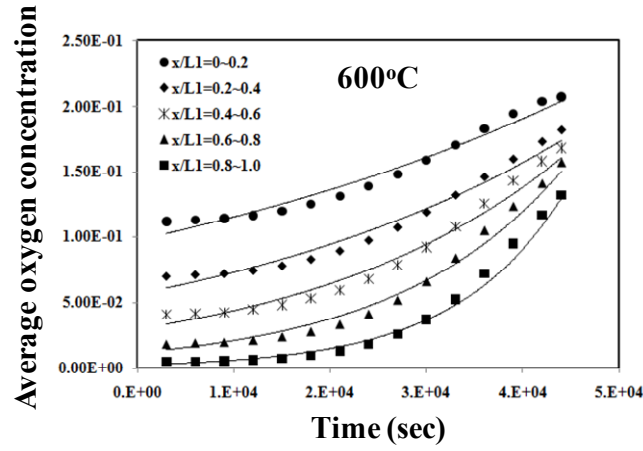


Figure 5. 3. Plot of time history of oxygen concentration profile: (a) contour plot of oxygen concentration, (b) nodal concentration distribution of cell at the location of  $x/L_1 = 0 \sim 0.2$ , (c) average oxygen concentration of cell at the location of  $x/L_1 = 0 \sim 0.2$  (d) average oxygen concentrations at each location.



(d)

Figure 5. 3. Continued.

### 5.2.2. Change of Foam Porosity Due to Oxygen Concentration

Based on the ligament geometry described in Section 3.4.4, the ligament mass flux (Equation 3.4) is,

$$\dot{m}_c'' = \frac{d}{dt} \left( \frac{m}{A_s} \right) = \rho \frac{d}{dt} \left( \frac{V}{A_s} \right) = \rho \frac{d}{dt} \left( \frac{3a^2 \sin \theta \cos \theta l}{6a \cos \theta l} \right) \quad (3.4)$$

Substituting Equation 3.4 into 2.11, the reduction rate of ligament thickness ( $v$ ) can be expressed as,

$$v(t) = \frac{da}{dt} = \frac{2}{\rho \sin \theta} \frac{MW_C MW_{mix}}{MW_{O_2}} \frac{P}{RT} A \exp \left[ -\frac{E_A}{R_u T} \right] C_{O_2} = C_2 \alpha \exp(\beta t) \quad (5.1)$$

where,  $C_2$  is constant for the isothermal temperature and atmospheric pressure. Integrating oxidation velocity (used in this work to describe the reduction rate of the ligament thickness) with time,  $a(t)$  yields,

$$a(t) = a_o - \int_0^t v dt = a_o - \int_0^t C_2 \alpha \exp(\beta t) dt = a_o - C_2 \frac{\alpha}{\beta} [\exp(\beta t) - 1] \quad (5.2)$$

where,  $a_o$  is the initial ligament thickness of 0.2 mm and  $t$  is the exposure time in seconds. Substituting Equation 5.2 into the porosity equation (Equation 2.5), the porosity (or relative density) of cell can be expressed as follows,

$$\Phi(t) = 1 - \frac{3[0.91a(t)]^2 \sin \theta \cos \theta l N_{ligament}}{V_{cell}} \quad (5.3a)$$

$$R(t) = \frac{3[0.91a(t)]^2 \sin \theta \cos \theta l N_{ligament}}{V_{cell}} \quad (5.3b)$$

where  $a(t)$  is the time dependent ligament thickness,  $a_o - C_2 \frac{\alpha}{\beta} [\exp(\beta t) - 1]$ ,  $l$  and  $N_{ligament}$  are ligament length and number of ligament in a sing cell, respectively. According to Equation 5.3(a), pore volume fraction in a single cell can be expressed in terms of ligament thickness which is a function of oxygen concentration. Figure 5.4, for example, shows the variation of pore volume fraction in a single cell at the each location ( $x/L_I$ ) as a function of time. Note that the initial pore volume fraction of all cells is 0.83. When exposed for same time period at the temperature of 600°C, the oxygen concentration gradient results in the different increase rate of the pore volume fraction. For example, in this plot, the pore volume fractions at the each location ( $x/L_I$ ) are increased to 0.95, 0.92, 0.88, 0.85 and 0.83, respectively after 100 minutes. The cell near the exterior surface shows rapid increase in pore volume (increased by 14.8%); however, the cell in the center of the foam maintains its original pore volume fraction after this time period since oxygen concentration at the center of foam is almost zero (0.0039).

The pore volume at the center of foam begins to increase at 152.8 minutes (increased by 1%). From the normalized length ( $x/L$ ) of 0.1 to 0.9, the times to reach the pore volume fraction of 0.95 are about 98.3, 144.9, 233.3, 394.9 and 588.3 minutes, respectively.

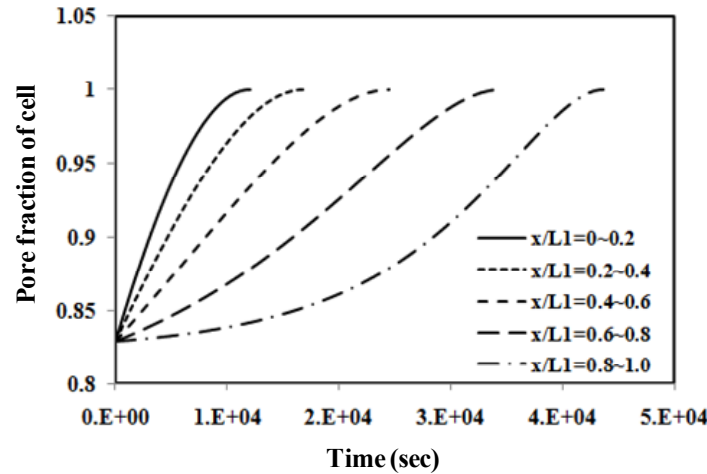


Figure 5. 4. Plot of change in pore volume fraction of single cell as a function of time.

### 5.3. Time Dependent Compression Response of Bulk Foam

#### 5.3.1. Problem and Model Description

The 3D model of 5 x 5 x 5 cells of Section 4.2.5 is used in evaluating the degradation in effective modulus of the bulk foam. Because of the symmetry involved in this analysis, the idealized cube block is modeled as a quarter-model with x- and z-symmetry planes. In this model, it is assumed that two out of six faces of model are protected from oxidation since the top and bottom surfaces are in contact with the loading plate and fixture. Thus oxygen can diffuse into the foam in x- and z- direction from the exterior surfaces. Figure 5.5 shows the details of the model description.

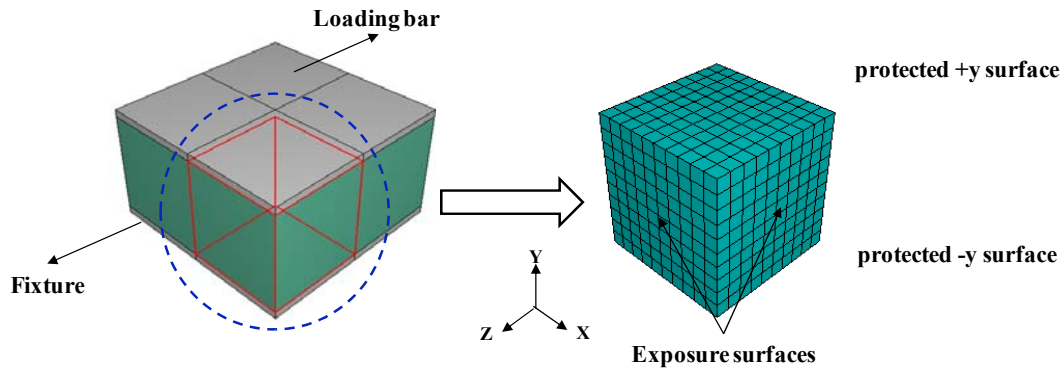


Figure 5. 5. Model description of idealized foam.

### 5.3.2. Mesh Creation and Time Dependent Properties

The idealized cube model is meshed with 8-node thermally coupled solid elements (C3D8T); this model consists of 1,000 elements and 1,331 nodes. In order to account for the thermal expansion at the oxidizing temperature of 600°C and 700°C, the bulk coefficient of thermal expansion (CTE of  $4.5 \times 10^{-6}$  1/K) determined in Section 4.4 is assigned to the FE model. Non-uniform oxidation due to the oxygen concentration gradient leads to change in the relative density with the increase of exposure time. Although closed-form solutions and empirical formulas are reported to predict the stiffness of carbon foams with respect to the relative density ( $R$ ), there are no expressions that relate relative density ( $R$ ) and oxidation time since carbon foam oxidation depends on the activation energy and geometry of foam. As described in the previous section, by using the relationship between the oxygen concentration profile and oxidation kinetics equation, time dependent ligament thickness (Equation 5.2) is driven. Then this equation is utilized to express the relative density ( $R$ ) as a function of time by substituting into the proposed relative density equation (Equation 5.3b). Gibson and

Ashby used a micromechanics model of cubic cells for effective modulus ( $E^*$ ) of an open-cell foam and reported the following formula [31],

$$E^* = K E R^2 \quad (5.4)$$

where,  $E$  is the Young's modulus of ligament and the constant  $K$  was found to be close to unity after curve fitting the experimental data. Note that the effective modulus is assumed as a second order the polynomial form  $E^* = k_l E R^2$ , where  $k_l$  is determined by curve fitting using OriginPro. The value of  $k_l$  at 1.52 is found to be the best fit ( $r^2=0.9991$ ) for the FEA results. Figure 5.6 shows the plots of the FEA results and Equation 5.4 with constant ( $k_l$ ) of 1.52.

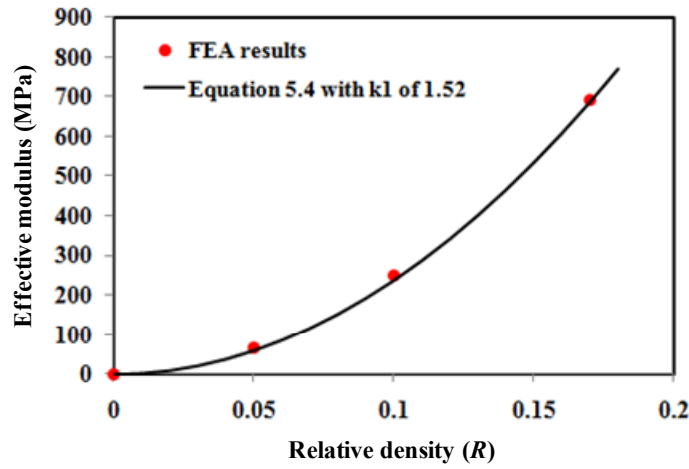


Figure 5. 6. Comparison of FEA results to Equation 5.4 with  $k_l$  of 1.52.

By substituting Equation 5.3b into Equation 5.4, time dependent effective modulus can be expressed as follow,

$$E(t)^* = k_l E R(t)^2 = k_l E \left[ \frac{3[0.91a(t)]^2 \sin \theta \cos \theta l N_{ligament}}{V_{cell}} \right]^2 \quad (5.5)$$

where,  $a(t)$  is ligament thickness, which varies with the exposure time and is also coupled with the oxidation rate.  $l$  and  $N$  are ligament length and the number of ligament in a single cell, respectively. The time dependent Young's moduli of each cell are assigned to an individual cell using user subroutine (UMAT) in ABAQUS; the initial Young's modulus is 690 MPa. Details of UMAT code is described in appendix B.

### 5.3.3. Boundary and Loading Conditions

As illustrated in Figure 5.7, the temperature of 600°C is assigned to model to include the effect of thermal expansion and simultaneously, the nodes that are on  $-y$  plane of the model are constrained in the  $y$ -direction. A uniform displacement of -0.07 mm is applied to all nodes on the  $+y$  surface. Symmetry boundary conditions are applied on the  $-x$ -plane and  $-z$ -plane of the quarter model by constraining all the nodes on that surfaces to zero displacement in the  $x$ - and  $z$ -directions ( $u_x = u_z = 0$ ).

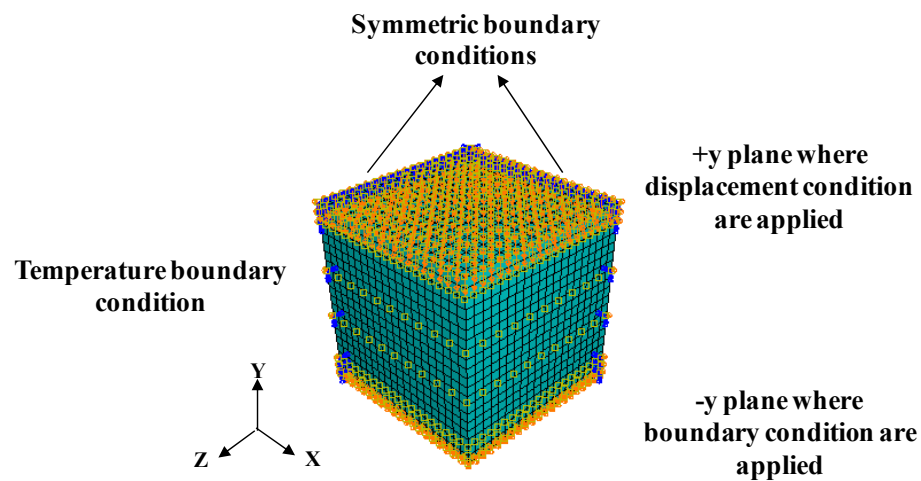


Figure 5. 7. Illustration of boundary conditions.

#### 5.3.4. Reaction Force and Stress Distribution

The displacement outputs in each coordinate direction are shown in Figure 5.8. The displacement on the +y-surface is -0.07mm, which reflects the applied displacement boundary condition (Figure 5.8 (a)). The displacements in the x- and z-direction are shown in Figure 5.8 (b). The total expansion in the x-direction is 0.0231mm and occurs uniformly throughout y-z plane since the nodes on -y plane are only constrained in the only the y-direction. The same total expansion of 0.023 mm occurs in the z-direction as well since the same boundary conditions are applied in the z-direction.

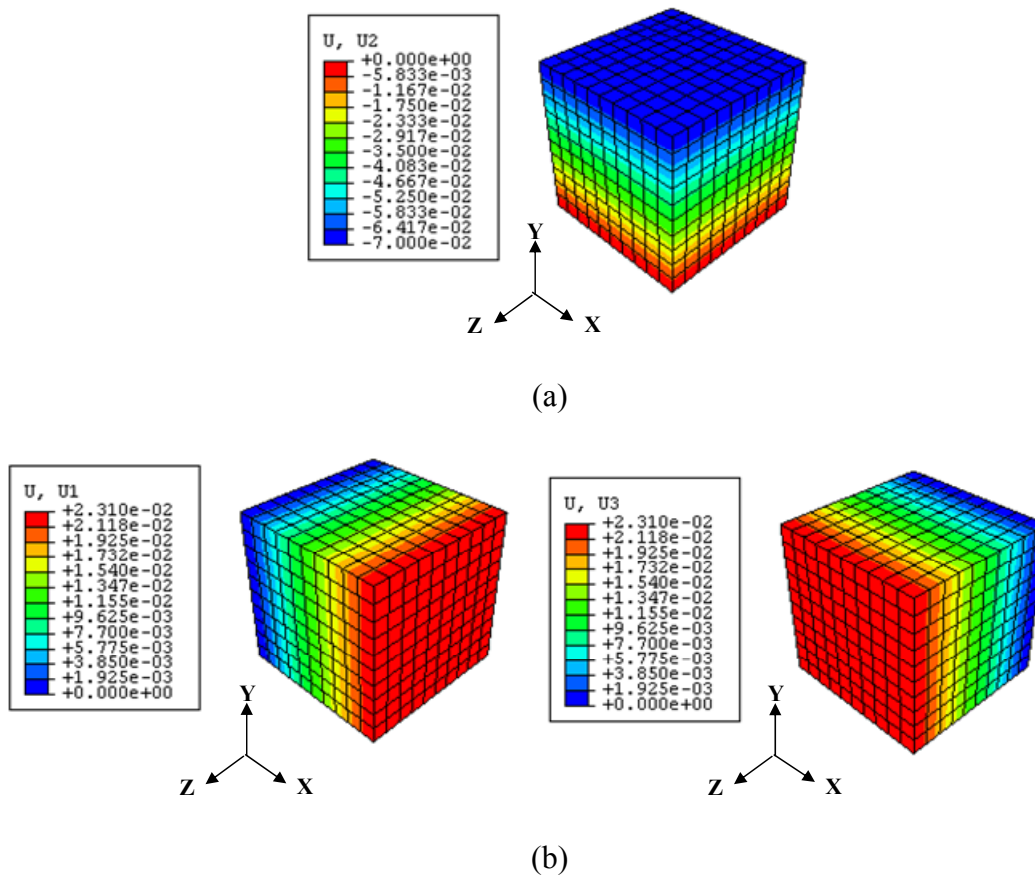


Figure 5. 8. Displacement output fields: (a)  $u_y$ , (b)  $u_x$ , and  $u_z$ .



The representative contours of the normal stress ( $\sigma_{22}$ ) in the y-direction are shown in Figure 5.9. Here, the stress distribution is plotted within the same contour limits (-7.60 MPa to zero) for a comparison purpose. Note that +x and +z-surfaces are exposed to air, allowing oxygen diffusion through these surfaces. At the initial stage ( $t=0$ ), the stress distributions are uniform in the overall model since oxidation has not initiated and cells exhibit their original stiffness. The normal stress ( $\sigma_{22}$ ) begins to decrease starting at the exposed surfaces (+x- and +z-planes) as time increases. Then this decrease gradually progresses toward the center of model over time. For example, after 51.7 minutes elapse, the stress at the center retains its original value of -7.56 MPa. However, the stress near the exposure surface is -6.11 MPa, which decreased by 19.6%. After 218.3 minutes, the cells near the exposure surface show almost 99% reduction in stress, whereas only 9.6% decrease occurs at the center cells: As time increases, the center cells also begin to decrease rapidly to 16.5% and 20.7% of their values after 285 minutes and 318 minutes, respectively.

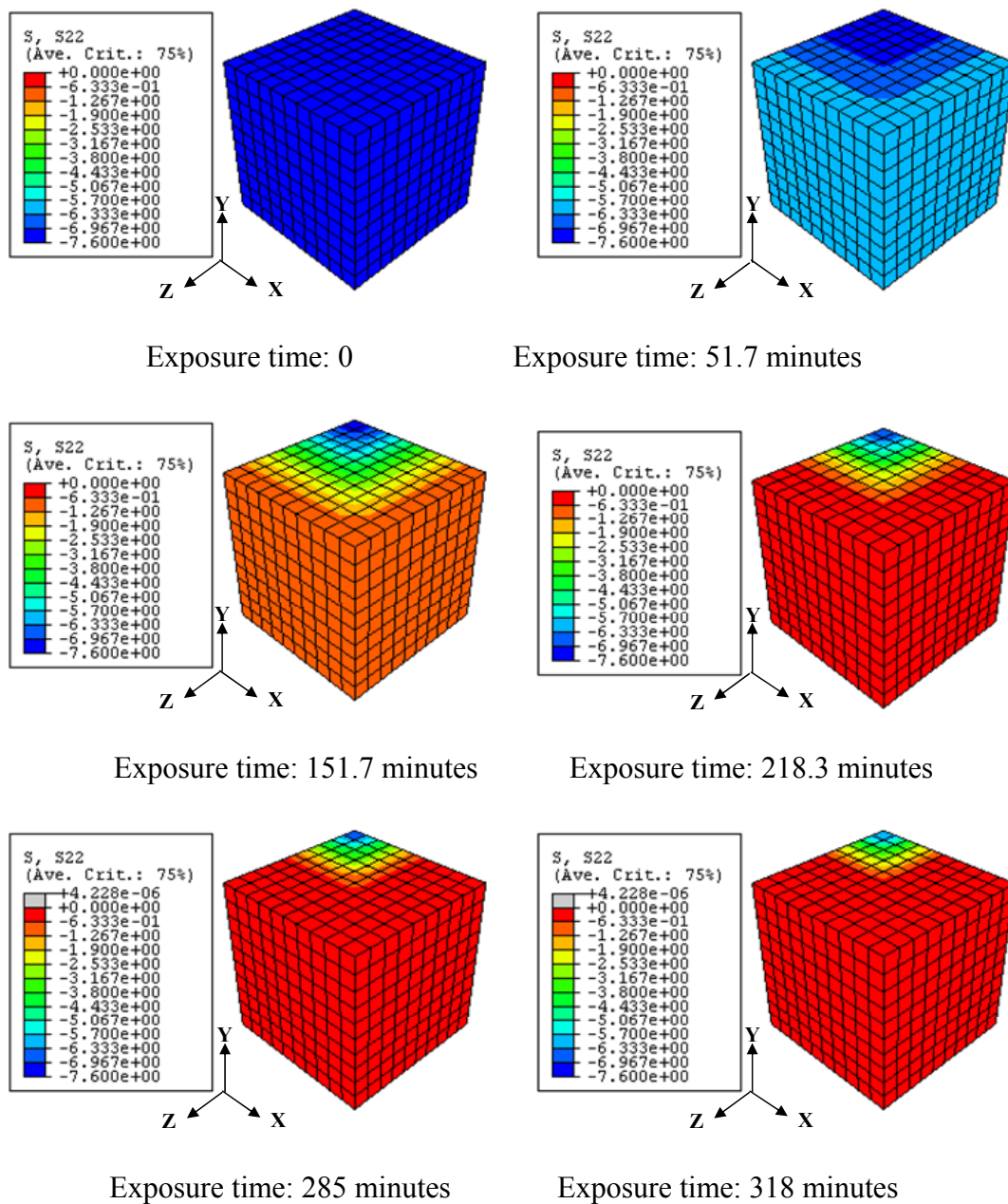


Figure 5. 9. Normal stress (MPa) contours in the y-direction as a function of exposure time.

Figure 5.10 shows the plot of normal stress ( $\sigma_{22}$ ) in the y-direction at each location ( $x/L$ ) as a function of time. Stress distributions in the y-direction on x-y plane are consistent along the y-direction. When looking at the normal stress ( $\sigma_{22}$ )-time curve, as the normalized length ( $x/L$ ) increases, the stresses decrease more rapidly since a higher  $x/L$  means the location is closer to the exposed surfaces. The initial stress at all nodes is -7.60 MPa and is the same regardless of the normalized length ( $x/L$ ). As time increases, the rates of reduction in stresses vary with their location. The main reason for this non-uniform decrease rate is the oxygen concentration gradient throughout the model. For example, the cells near the exposure surface experience a high reduction rate at the beginning stage of oxidation (at 1.7 minutes) due to high oxygen concentration (0.1), whereas the center cell subjected to low oxygen concentration of 0.002 results in retaining its initial value of -7.60 MPa.

After 25 minutes, the stress at the location ( $x/L$ ) of 0.1 (center cell) is -7.55 MPa (decreased by 0.7%), whereas that at the location ( $x/L$ ) of 0.9 is -4.71 MPa (decreased by 38.1%). The time to reach the 50% decrease is about 35 minutes at the location ( $x/L$ ) of 0.9 (outer cell), whereas the time for the same amount of decrease % is 415 minutes at the location ( $x/L$ ) of 0.1 (center cell).

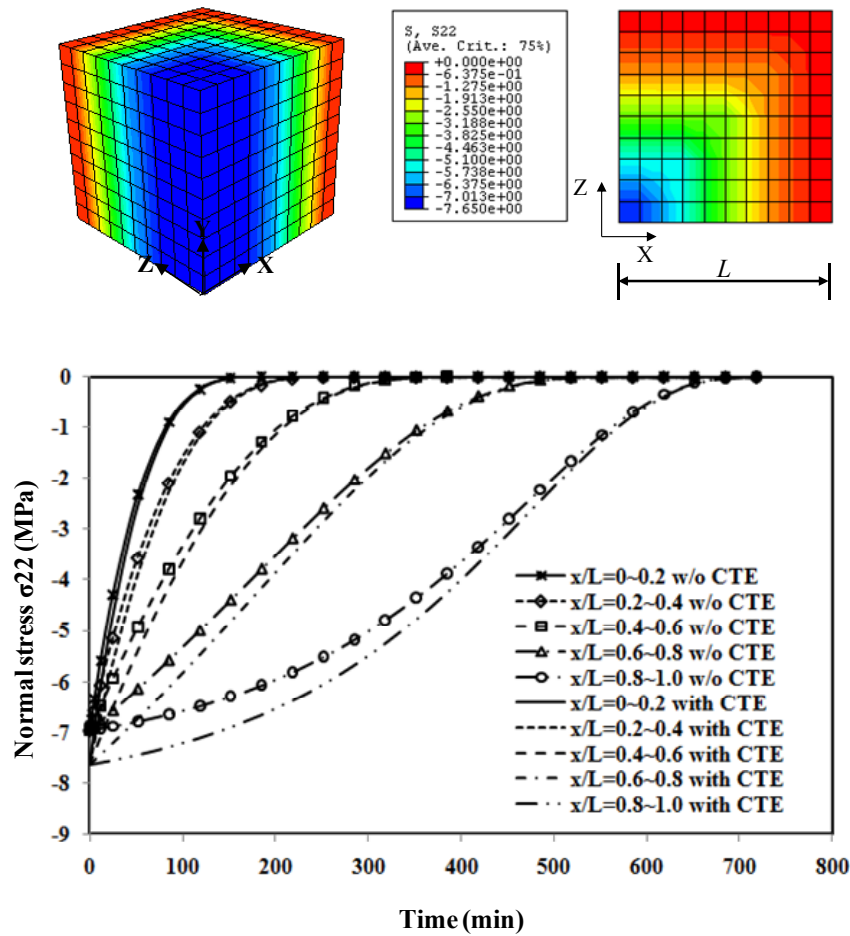
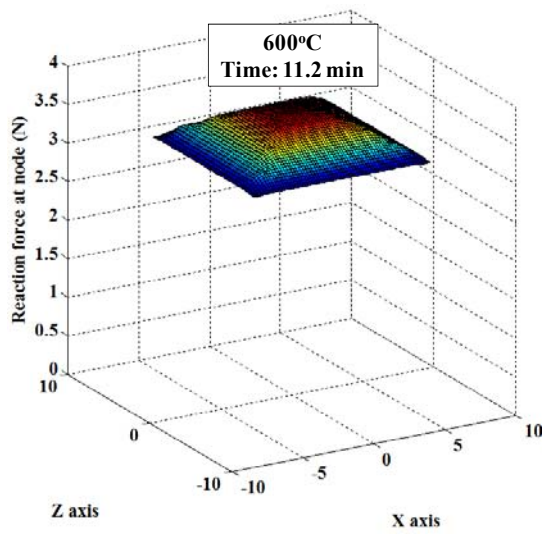


Figure 5. 10. Plot of normal stress in y-direction of each normalized location ( $x/L$ ) at  $z=0$  as a function of time. The plot with marks is the stress vs. time curve with neglecting thermal expansion at the temperature of  $600^{\circ}\text{C}$ .

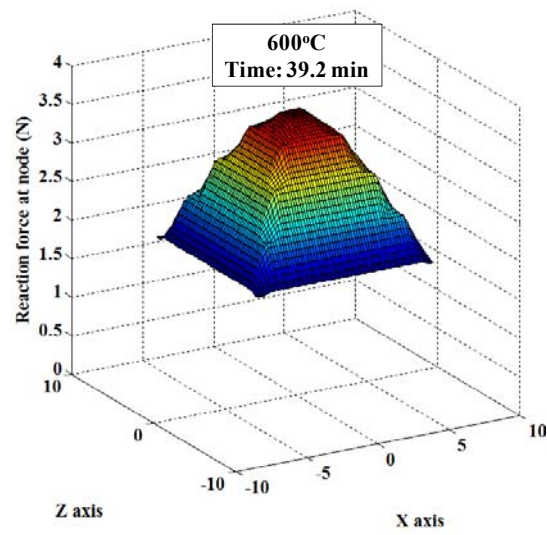
The resultant nodal reaction forces also vary with the location due to the different degradation rate. For example, the cells near the exposure surfaces (+x-and +z-surfaces) are in contact with the higher oxygen concentration where faster oxidation occurs than the interior of the foam. With the same method described in Section 3.2.3, the three-dimensional the resultant nodal reaction forces are plotted as a function of time by using ‘SURF’ option in MATLAB. Figure 5.11 shows representatives of 3-D plot of nodal

resultant force at temperature of 600°C. Note that all figures are plotted within the same scale of axis for comparison purposes. After 11.2 minutes exposure, the reaction force on +y-surface is almost uniform as seen in Figure 5.11 (a). The minimum reaction force of 3.18 N is at the near exposure surface and the maximum value (3.71 N) is observed at the center of foam. The summation of the nodal reaction forces leads to 340.3 N. When compared to its initial value of 374.2N, the total reaction force is decreased by 9.1 %.

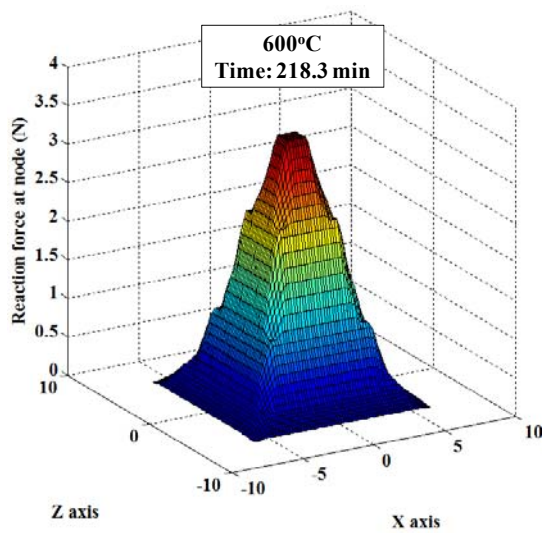
After 39.2 minutes of exposure (Figure 5.11 (b)), the cells near the exposed surfaces show 49.3% decrease in nodal reaction force (3.71 N to 1.88 N); whereas the reaction force at central cells are degraded by 1.4 % (3.71 N to 3.66 N). When looking at the oxygen concentration profile shown in Figure 5.3 (d), the average oxygen concentration at the exposure surface is 0.103, however this value at the center is 0.003. Note that at this time, the pore fractions calculated by Equation 5.4(a) are 0.913 and 0.832 at the exposure surface and the center, respectively. After 218.3 minutes of exposure (Figure 5.11 (c)), the reaction force at the exposed surface is decreased to almost zero (0.02 N), and begins to decrease at the center. After 218 minutes, the values of the total reaction force and decrease % in total reaction forces are given in Table 5.1.



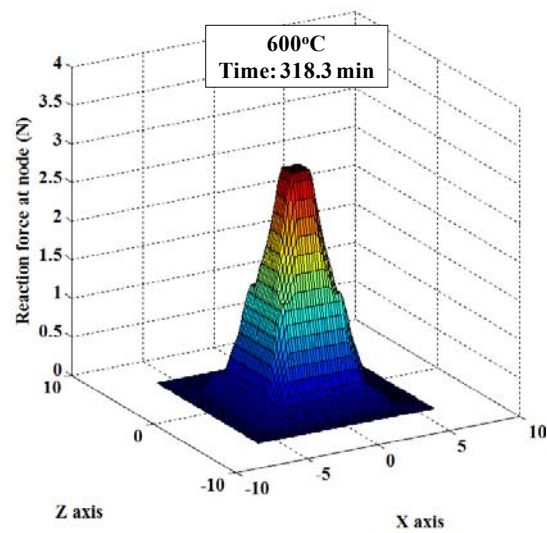
(a)



(b)



(c)



(d)

Figure 5. 11. Representatives of 3-D plot of resultant nodal reaction force at the temperature of 600°C: (a) after 11.2 minutes, (b) after 39.2 minutes, (c) after 218.3 minutes, and (d) after 318.3 minutes.

Table 5. 1. List of total reaction forces and decrease % in total reaction forces as a function of time for bulk foam (600°C)

Time (minutes)	Total reaction force	Decrease %
0	374.4 N	0
285	36.2 N	90.3 %
351.7	22.5 N	93.9 %
418.3	13.9 N	96.2 %
551.7	8.9 N	97. 6%

To investigate the influence of temperature on the effective bulk modulus of bulk foam, average oxygen concentration profiles at the temperature of 700°C are also obtained with the same process described in Section 5.2.1. The assigned material properties are listed in Table 3.1 in Section 3.4.2. The time histories of oxygen concentration at an individual cell were determined by the taking average values of the cell and plotted as shown in Figure 5.12. Note the cell locations are expressed in the same coordinates as shown in Figure 5.3 (a).  $x/L$  of 0~0.2 is the first cell from the exposed surface.

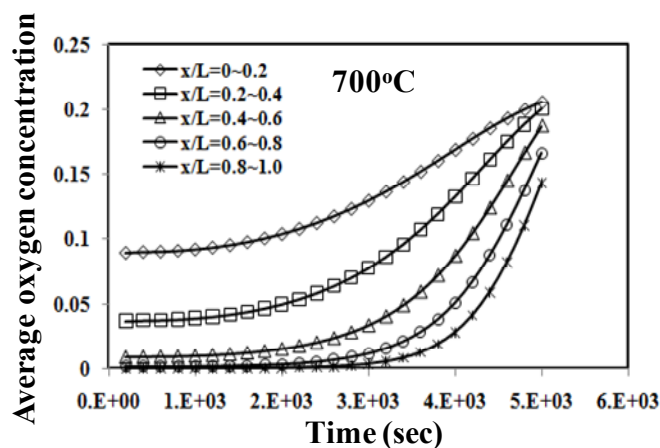


Figure 5. 12. Average oxygen concentration profiles of cells as a function of time (700°C).

The time dependent material properties are assigned to individual cell using subroutine (UMAT) in ABAQUS. Similar to the boundary conditions described in Section 5.3.3, a displacement of 0.07 mm (1% strain magnitude) is applied to all the nodes on the +y-surface and all nodes on the -y-surface are fully constrained in the y-direction. In addition, temperature of 700°C is applied to account for thermal expansion during oxidation. Details of the boundary conditions are illustrated in Figure 5.7.

The contours of the normal stress ( $\sigma_{22}$ ) in the y-direction are compared between the temperatures of 600°C and 700°C as a function of time as seen in Figure 5.13. Here, all stress distribution is plotted with the same contour limits (-7.85 MPa to zero). Initially, uniform stress distributions are seen in the overall model since all cells retain their original stiffness as seen in Figure 5.13 (a). The stress distributions begin to decrease from the exposed surfaces (+x- and +z-planes) and gradually progress toward the center of the model over time. The decrease rate is more rapid at the higher temperature. After 8.5 minutes (Figure 5.13 (b)), for example, normal stress ( $\sigma_{22}$ ) near the exposure surface is -6.78 MPa at 600°C, but that value is decreased to -3.78 MPa at 700°C (highlighted by arrow). This represents 10.8% and 51.9% decrease with respect to the initial value, respectively. Note that the cells at the center retain 99% of their original stress values in both cases (highlighted by red circle). At 17.5 minutes (Figure 5.13 (c)), stress near the exposure surface is decreased by 86.7%. However, only 23.4 % decrease occurs at the same location in the case of 600°C (highlighted by arrow). According to the oxygen concentration profiles in Figures 5.3 (d) (600°C) and Figure 5.12 (700°C), the oxygen concentrations at these locations are similar ( $\sim 0.1$ ) in both cases. Thus, the rate



of decrease reflects the carbon reaction rate that exponentially increases with temperature (Equation 2.11). After 69.2 minutes (Figure 13 (f)), only the center cell shows high stress value (-6.54 MPa) at the temperature of 700°C. However, at the temperature of 600°C, the center cells show the range of stress -2.62 to -7.36 MPa, indicating they still retaining their stiffness although there is the difference of magnitude (highlighted by red circle)

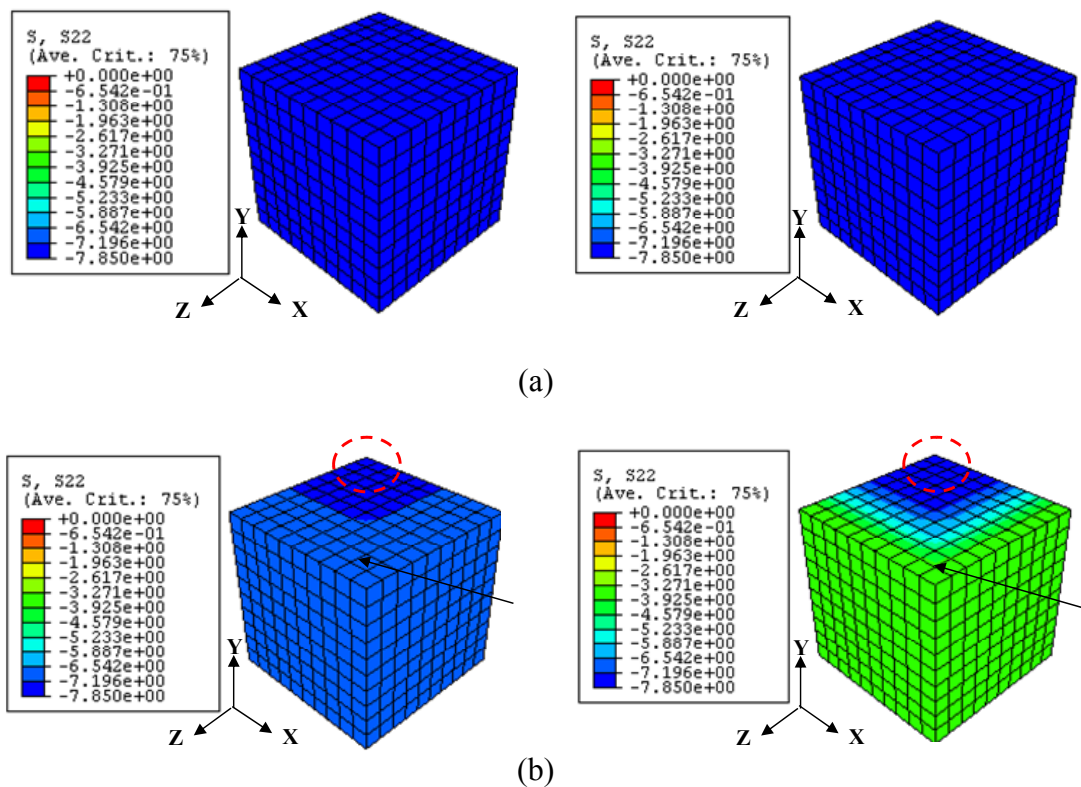


Figure 5. 13. Comparison of normal stress (MPa) in the y-direction as a function of time- left figure at 600°C and right figure at 700°C: (a) initial, (b) time 8.5 minutes, (c), time 17.5 minute, (d) 34.2 minutes, (e) 44.6 minutes, and (f) 69.2 minutes.

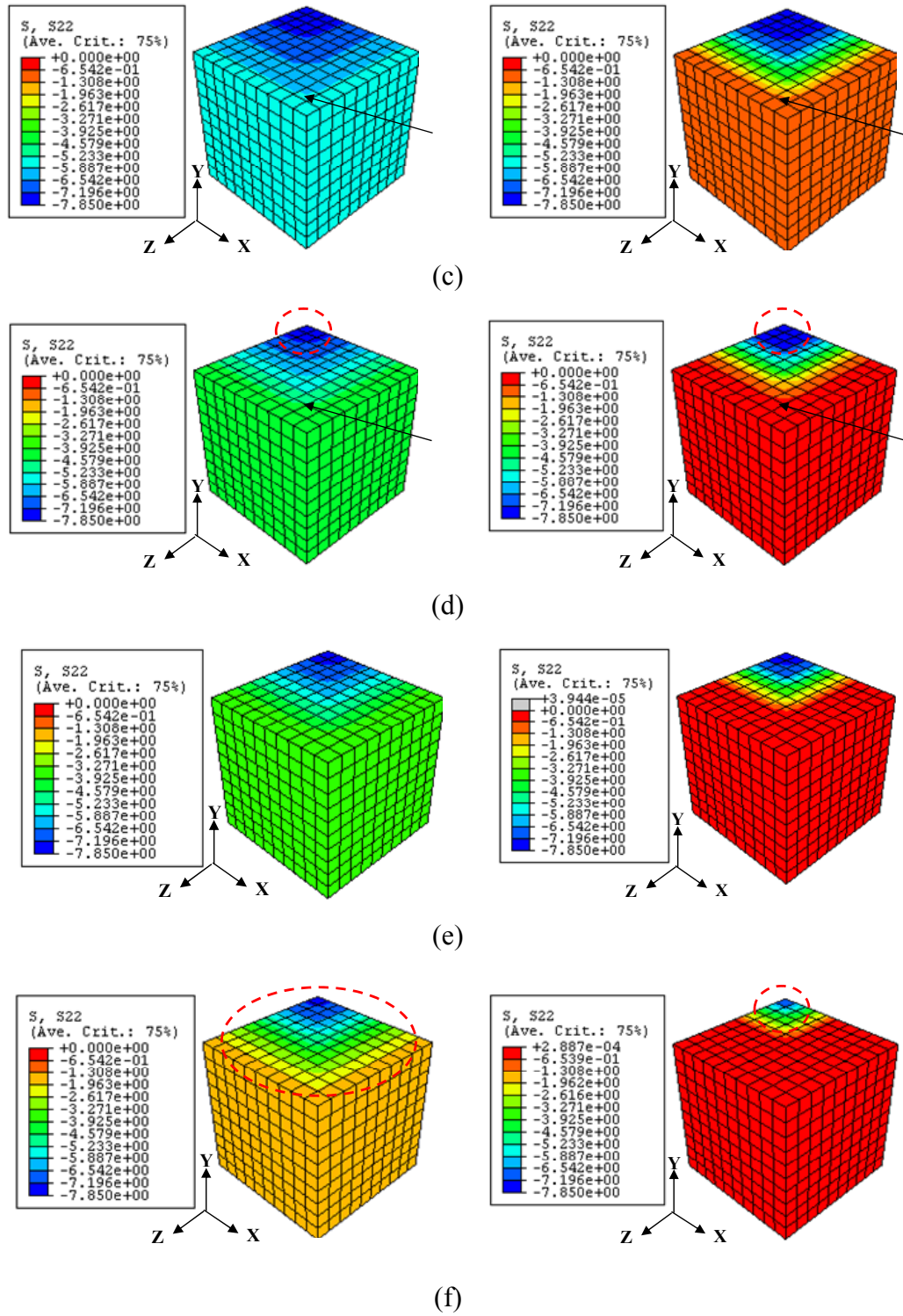


Figure 5.13. Continued.

These observations on ( $\sigma_{22}$ ) are summarized in Figure 5.14 as a function of location. Note that the variations of stresses at 700°C are plotted with different marker types, such as triangle, circle, Etc. First, as expected, the overall decrease in stress occurs more rapidly at 700°C. For example, at the normalized location ( $x/L$ ) of 0.9, the time to reach 90% decrease is about 15.5 minutes at 700°C, whereas the time for the same decrease percent is about 91.2 minutes at the temperature of 600°C. At the location of 0.1 (center cell), the stress decrease initiates at 44.5 minutes in the case of 700°C (dash red line), however, no distinct decrease is observed even after 108 minutes when exposed at the temperature of 600°C.

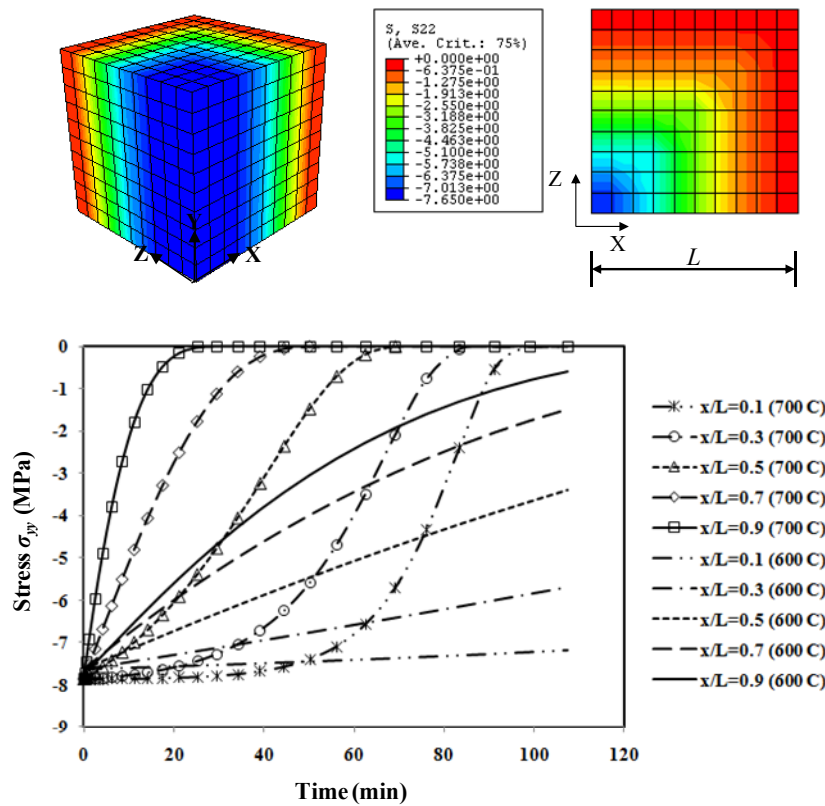


Figure 5. 14. Plot of normal stress in y-direction of each normalized location ( $x/L$ ) at  $z=0$  as a function of time. Dash red line represents the time of degradation initiation at the center cell at 700°C.

The reaction forces in the y-direction ( $RF_2$ : the forces that act in the opposite direction of displacement boundary condition) for 600 °C and 700°C models are compared over time by the three-dimensional plot in Figure 5.15. Although the same magnitude of displacement boundary condition (-0.07 mm) is on the model in the -y-direction, the variation of reaction forces are observed throughout the model. Figure 5.15 shows the representatives of 3-D plots of nodal reaction forces as a function of time. After 11.2 minutes exposure, the reaction forces are almost uniformly distributed in the case of 600°C, whereas distinct decrease in reaction forces is observed at 700°C: the minimum reaction force (1.33 N) at the exposure surface, the maximum reaction force (3.83 N) at the center cell. At this time, the sum of reaction force of 700°C is 253.5 N (decreased by 33.6 %), that of 600°C is 340.3 N (decreased by 9.1 %). After 39.2 minutes, the cells near the exposure surface show 99% decrease in reaction force (3.83 N to  $1.57 \times 10^{-4}$  N) at 700°C; only 49% decrease is observed at 600°C. At this time, the sum of reaction forces at 600°C and 700°C are 253.2 N and 103.7 N, respectively. Some values of the total reaction forces ( $P^{total}$ ) at each temperature are given in Table 5.2.

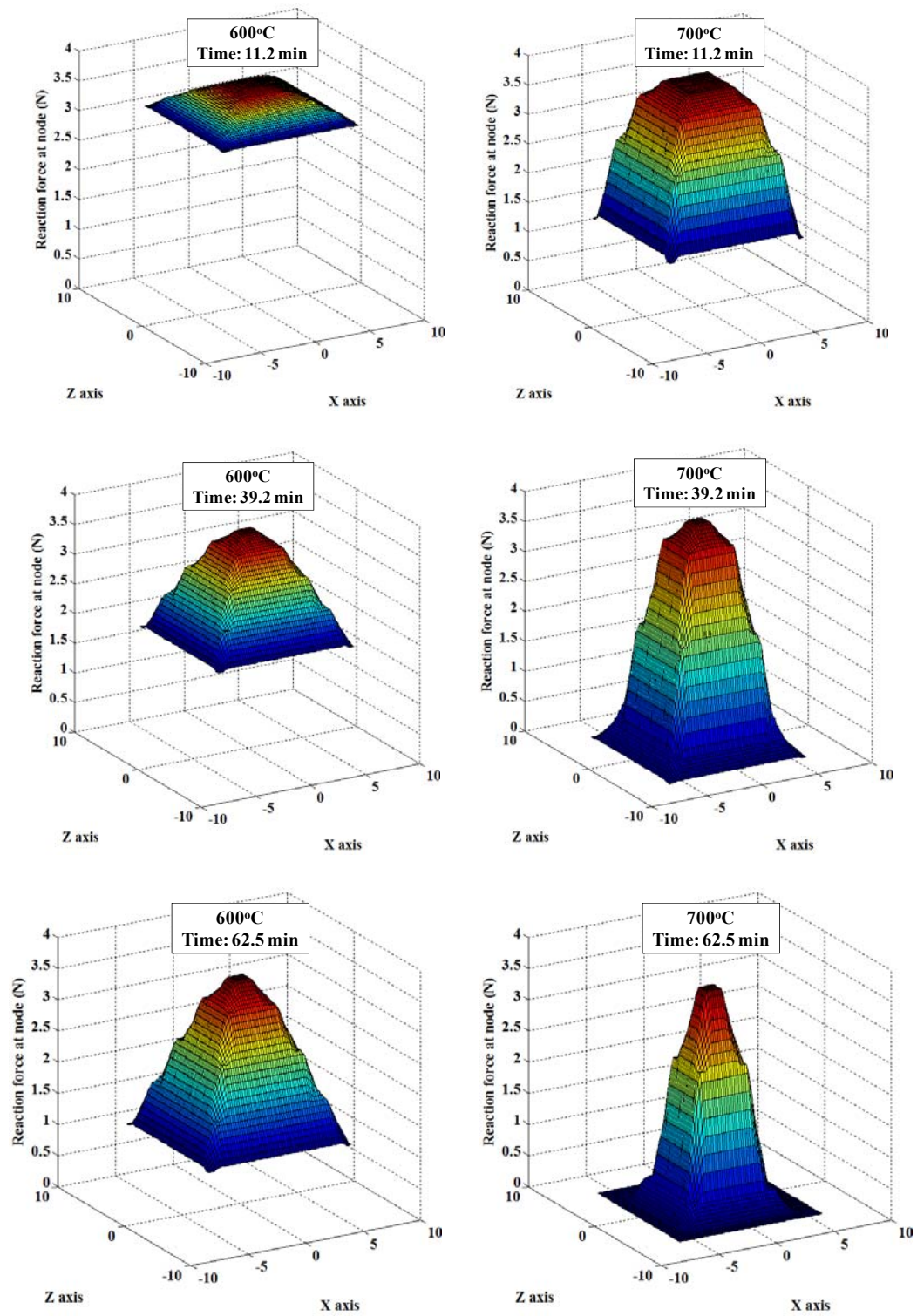


Figure 5. 15. Representatives of 3-D plot of nodal reaction force as a function of time: right figure is 600°C and left figure is 700°C.

Table 5. 2. Total reaction forces for temperature of 600 and 700°C at each time exposure.

Time (minutes)	600°C		700°C	
	$P^{total} (N)$	Decrease %	$P^{total} (N)$	Decrease %
0	374.4	-	381.5	-
44.5	238.8	36.2	88.8	76.7
56.2	209.9	43.9	61.4	83.9
69.2	181.7	51.5	35.1	90.8
83.5	154.9	58.6	12.9	96.6
99.2	130.6	65.1	1.0	99.7

### 5.3.5. Evaluation of Degradation in Bulk Stiffness

According to the average strain theorem [35, 36], the time dependent effective modulus,  $E^*(t)$ , can be expressed as follows,

$$E^*(t) = \frac{\bar{\sigma}}{\bar{\varepsilon}} = \frac{L}{\Delta\delta} \frac{\sum P^{nodal}(t)}{A} \quad (5.6)$$

where, the average strain  $\bar{\varepsilon}$  is calculated using  $\Delta\delta/L$  where  $\Delta\delta$  is the prescribed boundary condition of 0.07 mm and  $L$  is 7 mm. The summation of nodal reaction forces ( $\sum P^{nodal}(t)$ ) are obtained from FEA results at each time period. The normalized effective modulus  $E_t^*/E_o^*$  is plotted in Figure 5.16 as a function of time. Where,  $E_t^*$  is effective modulus of bulk foam at time  $t$  and  $E_o^*$  is the initial effective modulus ( $t=0$ ). It is seen that degradation of effective modulus is more rapid at 700°C. For example, after 25.2 minutes elapse, the effective modulus calculated by equation 5.6 is 545.5 MPa at 600°C (decreased by 21.4 %), whereas its value at 700°C is 243.2 MPa, indicating a decrease of 59.8%.

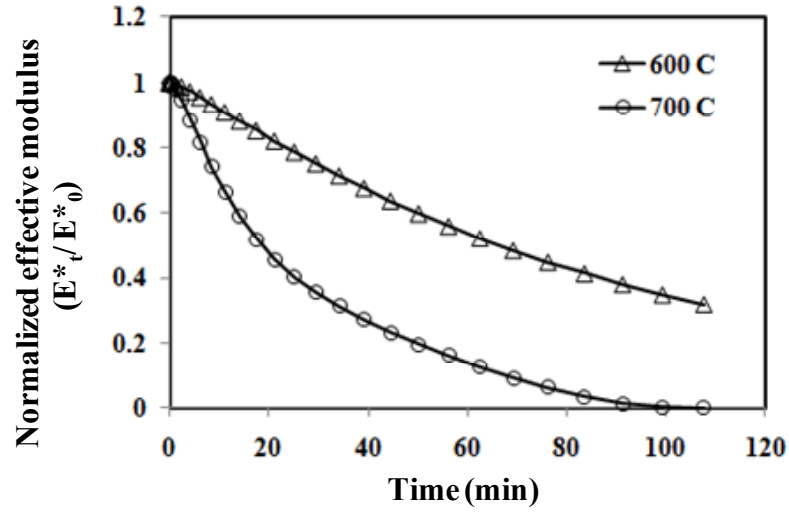


Figure 5. 16. Plot of variation in normalized effective modulus as a function of time.

The normalized stiffness of bulk foam at two temperatures are calculated using the following relationship,

$$\text{Normalized stiffness } (\bar{k}) = 1 - \frac{k_t}{k_o} \quad (5.7)$$

where,  $k_o$  is initial axial stiffness ( $\sum P/\Delta\delta$ ) and  $k_t$  is the bulk foam stiffness at time  $t$  ( $\sum P_t/\Delta\delta$ ). The time elapse for the same degradation at each temperature is plotted in Figure 5.17. For example, the time for 10% reduction in stiffness is 3.2 minutes at 700°C, whereas 11.8 minutes of exposure at 600°C resulted in the same degradation %. Although the degradation rate seems to decrease as time increases, the average degradation rate is evaluated by slope of degradation ratio vs. time curve (red line). Note that the average degradation rate at 700°C is 3.6 times more rapid than that of 600°C.



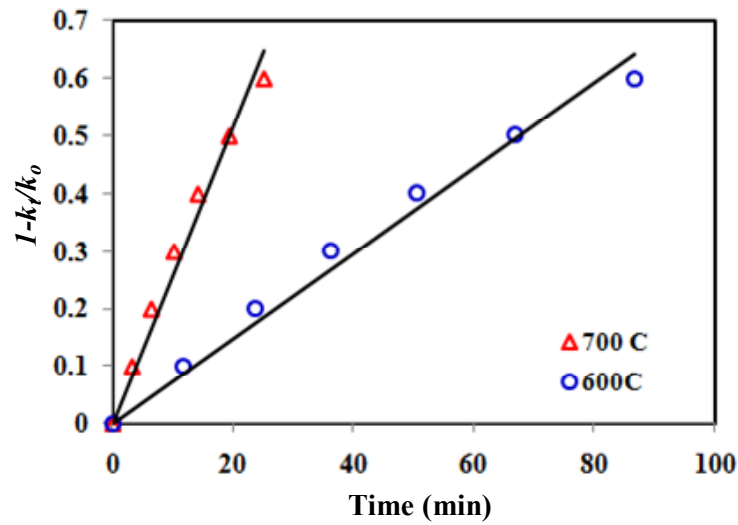


Figure 5. 17. Change in normalized stiffness vs. time at 600 and 700°C as a function of time.

#### 5.4. Remarks

In this section, the idealized bulk foam models, as determined in Section 4.2 were simulated to evaluate the degradation in effective modulus in bulk foam at the temperature of 600°C and 700°C. First, the oxygen concentration profiles throughout the foam were identified as a function of time and utilized to predict the variation of porosity over time by integrating these profiles into carbon reaction model.

By combining the relationships of the cell porosity-exposure time and the cell porosity-stiffness, the time-dependent effective modulus of bulk foam was simulated as a function of time at the temperature of 600°C and 700°C. First, when the displacement boundary condition (1% strain magnitude) was applied on the model, the oxygen concentration gradient resulted in non-uniform degradation in effective modulus of bulk foam. The cell near the exposed surface showed more rapid reduction in reaction force



than the interior foam. In addition, to investigate the influence of temperature on effective bulk foam, the variation of effective modulus at 600°C was compared to that of 700°C as a function of time. The temperature effect dominated degradation in bulk effective modulus of carbon foam. For example, after 8.5 minutes elapsed, no distinct decrease in reaction force was observed at 600°C, whereas total reaction force was decreased by 25.9%. Note that the oxygen concentrations in both cases are similar (~0.1) at this exposed time. The rate of decreases reflected the carbon reaction rate that exponentially increased with temperature. Consequently, by comparison of the slope of normalized effective modulus vs. time curves, it is found that the average degradation rate at the temperature of 700°C was 3.6 times more rapid than that of 600°C.

## 6. CONCLUSIONS

In this study, experimental and computational models were developed to assess the carbon foam in an oxidizing environment as a function of exposure time and temperature. Thermogravimetric analyzer (TGA) and furnace exposure tests were conducted to obtain mass loss of carbon foam at 600°C, 700°C, and 800°C. The results showed clearly that the mass loss of carbon foam increased as the temperature increased. The apparent activation energy was calculated to be 123.12 kJ/mol from the mass loss versus time curve data obtained from the TGA experiment. Furthermore, morphological changes were identified by optical microscopy (OM) observations of the sample before and after oxidation. Three distinct degradation patterns were observed and classified: (1) reduction in ligament thickness; (2) merging of pores; and (3) creating pore. These observations also revealed that there is not any significant morphological change at the protected surface.

The non-steady state diffusion theory was used to obtain the oxygen concentration profile as a function of time. The results demonstrated that the oxygen penetrated deeper into the high porosity foam due to the larger pore size at a given temperature. Furthermore, the reduction rates of ligament thickness were evaluated by taking into consideration both the oxygen concentration profile and the kinetic reaction rate. The ligaments near the exposed surface experienced higher oxygen concentration than the cells located in the interior of the foam. Temperature also had a significant effect on the foam degradation. Five minutes of exposure at 700°C, resulted in a 7.8% reduction of the

ligament thickness. However, the same exposure time at 800°C, led to a 49.4 % reduction of ligament thickness.

Convergence studies were conducted to predict the effective bulk properties and to select an appropriate size for the representative volume element (RVE). The effective modulus obtained from a single cell with periodic boundary conditions matched clearly with the result of the multiple cells assembly of 10 x 10 x 3. The coefficient of the thermal expansion of bulk foam was calculated to be  $4.51\text{e}^{-6}$  1/K, which was 9.8% higher than the manufacturing data sheet. The degradation in bulk foam stiffness was found to be strongly dependent on the temperature and the non-uniform oxygen concentration profile.

## REFERENCES

1. Mesut, K., Aysenur, G., Ekerm, E., Ferhat, Y. and Ata, M. (2007). Computational Modeling of Micro-Cellular Carbon Foams. *Finite Elements in Analysis and Design*, **44**: 45-52.
2. Sihn, S.W., Roy, A.K. (2004). Modeling and Prediction of Bulk Properties of Open-Cell Carbon Foam. *Journal of the Mechanics and Physics of Solids*, **52**: 167-191.
3. Ford, W. (1967). Method of Making Cellular Refractory Thermal Insulating Material. U.S. Patent 3,121,050.
4. Kearns, K.M. (1999). Process for Preparing Pitch Foams. U.S. Patent No. 5,868,947. Washington, DC: U.S. Patent and Trademark Office.
5. Kearns, K.M. Pitch Foam Products. (1999); U.S. Patent No. 5,961,814. Washington, DC: U.S. Patent and Trademark Office.
6. Klett, J.W. (2000). Process for Making Carbon Foam. U.S. Patent No. 6,033,506. Washington, DC: U.S. Patent and Trademark Office.
7. Klett, J.W. (2001). Pitch-Based Carbon Foam and Composites. U.S. Patent No. 6,261,485. Washington, DC: U.S. Patent and Trademark Office.
8. Beechem, T.E. (2005). Growth Mechanism and Properties of Novel Carbon Nanocomposite Foams. M.S. Thesis, University of Dayton, 45481.
9. Rosebrock, G.J. (2005). Understanding and Control of Multifunctional Graphitic Foam Properties. M.S. Thesis, University of Dayton, 45481.
10. Klett, J.W. (2002). Pitch-Based Carbon Foam and Composites. U.S. Patent No. 6,387,343. Washington, DC: U.S. Patent and Trademark Office.
11. Sarzynski, M.D. (2008). Developing & Tailoring Multi-Functional Carbon Foams for Multi-Field Response. Ph.D. Dissertation, Texas A&M University, College Station.
12. Yang, J., Shen, Z. and Hao, Z. (2004). Microwave Characteristics of Sandwich Composites with Mesophase Pitch Carbon Foams as Core. *Carbon*, **42**: 1882-1885.

13. Rodriguez, D.E. (2009). Investigation of a HA/PDLGA/Carbon Foam Material System for Orthopedic Fixation Plates Based on Time-Dependent Properties. Ph.D. Dissertation, Texas A&M University, College Station.
14. Weiming, G., Hanning, X., Eiichi, Y. and Yin, C. (2006) Oxidation Kinetics and Mechanisms of a 2D-C/C Composite. *Carbon*, **44**: 3269-3276.
15. Aly-Hassan, M.S., Hatta, H., Wakayama, S., Watanabe, M. and Miyagawa, K. (1996). Comparison of 2D and 3D Carbon/Carbon Composite with Respect to Damage and Fracture Resistance. *Carbon*, **34**:387-395.
16. Zmot, J.X., Bradt, R.C. and Walker, Jr. P.L. (1985). Effect of Air Oxidation at 873K on The Mechanical Properties of a Carbon-Carbon Composite. *Carbon*, **23**(1):9-13.
17. Croker, P. and McEnaney, B. (1991). Oxidation and Fracture of Woven 2D Carbon-Carbon Composite. *Carbon*, **29**:881-885.
18. Lahaye, J., Louys, F. and Ehrburger, P. (1990). The Reactivity of Carbon-Carbon Composites. *Carbon*, **28**:137-141.
19. Mcos M.P., Dorvaux J.M., Lavigne, O. and Renollet Y. (2000). C/C Composite Oxidation Model I. Morphological Experimental Investigations. *Carbon*, **38**:77-92.
20. Li, T.H. and Zheng, X.L. (1995). Oxidation Behavior of Matrix-Modified Carbon-Carbon Composites at High Temperature. *Carbon*, **33**:469-472.
21. Jacobson, N.S. and Curry, D.M. (2006). Oxidation Microstructure Studies of Reinforced Carbon/Carbon Composites. *Carbon*, **44**:1142-1150.
22. Lamouroux, F. and Camus, G. (1994). Oxidation Effect on the Mechanical Properties of 2D Woven C/SiC Composites. *Journal of the European Ceramic Society*, **14**: 177-188.
23. Li, T.H. and Zheng, X.L. (1995). Oxidation Behavior of Matrix-Modified Carbon-Carbon Composite at High Temperature. *Carbon*, **33**(4): 469-472.
24. Dharni, T.L., Mandocha, L.M. and Bahl, O.P. (1991). Oxidation Behavior of Pitch Based Carbon Fibers. *Carbon*, **29**:21-60.

25. Luo, R.Y., Cheng, J.W. and Wang, T.M. (2002). Oxidation Behavior and Protection of Carbon/Carbon Composites Prepared Using Rapid Directional Diffused CVI Techniques. *Carbon*, **40**(11):1965-1972.
26. Crocker, P. and McEnaney, B. (1991). Oxidation and Fracture of a Woven 2D Carbon-Carbon Composite. *Carbon*, **29**: 881-889.
27. Lachaud, J., Aspa, Y. and Vignoles, G.L. (2008). Analytical Modeling of the Steady State Ablation of a 3D C/C Composite. *International Journal of Heat and Mass transfer*, **51**:2614-2627.
28. Lamouroux, F. and Camus, G. (1994). Oxidation Effects on the Mechanical Properties of 2D woven C/SiC Composites. *Journal of the European Ceramic Society*, **14**:177-188.
29. Lachaud, J., Bertrand, N., Vignoles, G.L., Bourget, G., Rebillat, F. and Weisbecker, P. (2007). A Theoretical/Experimental Approach to the Intrinsic Oxidation Reactivities of C/C Composites and of Their Components. *Carbon*, **45**:2768-2776.
30. Zhang, W.G., Cheng, H.M., Xie, T.S., Shen, Z.H., Zhou, B.L., Sano, H., Uchiyama Y. and Kobayashi, K. (1998). Oxidation Kinetics and Mechanism of Ceramic-Carbon Composite I. Modeling for the Nonreactive Ceramic Layer Type. *Carbon*, **36**:991-995.
31. Gibson, L.J. and Ashby, M.F. *Cellular Solids: Structures and Properties*. 1997, 2<sup>nd</sup> edn. Cambridge University Press, UK.
32. Christensen, R.M. (1986). Mechanics of Low Density Materials. *Journal of the Mechanics and Physics of Solids*, **34**(6): 563-578.
33. Warren, W.E. and Kraynik, A.M. (1997). Linear Elastic Behavior of a Low-Density Kelvin Foam with Open Cells. *Journal of Applied Mechanics*, **64**: 787-794.
34. Warren, W.E. and Kraynik, A.M. (1998). The Linear Elastic Properties of Open Cell Foams. *Journal of Applied Mechanics*, **55**: 341-34.
35. Li, K., Gao, X.-L. and Roy, A.K. (2003). Micromechanics Model for Three-Dimensional Open-Cell Foams Using a Tetrakaidecahedral Single Cell and

- Castigliano's Second Theorem, *Composites Science and Technology*, **63**: 1769-1781.
36. Li, K., Gao, X.-L. and Roy, A.K. (2005). Micromechanical Analysis of Three-Dimensional Open-Cell Foams Using the Matrix Method for Spatial Frames. *Composites Part B*, **36**: 249-262.
  37. Andrew, J. E., James D.C. and Triplicane A.P. (1995). Oxidation Kinetics of a Continuous Carbon Phase in a Nonreactive Matrix. *Journal of the American Ceramic Society*, **78**(4):972-980.
  38. Thomas J.M. and Walker P.L. (1965). *Chemistry and Physics of Carbon*, vol.1. Dekker, New York.
  39. Stephen R.T. (2000); *An Introduction to Combustion: Concept and Application*. McGraw-Hill Companies, Inc., New York.
  40. Glime, W.H., Cawley, J.D. (1995). Oxidation of Carbon Fibers and Films in Ceramic Matrix Composites: a Weak Link Process. *Carbon*, **33**(8):1053-1060.
  41. Klett, J.W. and Burchell, T.D. (2000). Pitch-Based Carbon Foam Heat Sink with Phase Change Material. U.S. Patent No. 6,037,032. Washington, DC: U.S. Patent and Trademark Office.
  42. Wang, Y.Q., Zhou, B.L., and Wang, Z.M. (1995). Oxidation Protection of Carbon Fibers by Coatings. *Carbon*, **33**(4):427-433.
  43. Wilhelam, J. (1952); *Diffusion in Solids, Liquids, Gases*. Academic Press Inc., New York.
  44. Cussler, E.L.. (2009); *Diffusion Mass Transfer in Fluid Systems*, 3<sup>rd</sup> edn, Cambridge University Press, New York.
  45. Product Data Sheet: CFOAM, <http://www.cfoam.com/data.htm> (accessed December 2008).
  46. Callistger, W.D. (2005); *Materials Science and Engineering an Introduction*, 6<sup>th</sup> edn, John Wiley & Sons, Inc., New York.
  47. Incropera, F.P. and DeWitt, D.P. (2002) *Fundamental of Heat and Mass Transfer*, 5<sup>th</sup> edn, John Wiley & Sons, Inc., New York.

48. Dhami, T.L., Manocha, L.M. and Bahl, O.P. (1991). Oxidation Behavior of Pitch Based Carbon Fibers. *Carbon*, **29**:51-60.
49. ERG Materials and Aerospace Corporation. Duocel Reticulated Vitreous Carbon Foam, <http://www.ergaerospace.com> (accessed December 2007).
50. Ultramet. Open cell Carbon Foam, <http://www.ultramet.com> (accessed December 2007).



## APPENDIX A

### BINARY DIFFUSION COEFFICIENT

Chapman-Enskog's description of binary mixture of gases is based on the molecular motion in gases [36]. This analysis depends on the assumption that molecular interactions involve collisions between two molecules at a time. The binary diffusion coefficient is expressed as,

$$D_{i-N_2} = 0.001853 \left( \frac{1}{M_i} + \frac{1}{M_{N_2}} \right)^{1/2} T^{3/2} \left( \frac{1}{P \sigma_{i-N_2}^2 \Omega} \right) \quad (\text{A-1})$$

where

$M_i$ : Mass of the subscripted molecule (*g/mol*)

$T$ : Absolute temperature (*K*)

$P$ : Pressure (*atm*)

$\sigma_{i-N_2}$ : Average diameter of two species (*Å*)

$\Omega$ : Collision integral (

The collision integral defined as follows,

$$\Omega = \frac{A}{(T^*)^B} + \frac{C}{\exp(DT^*)} + \frac{E}{\exp(FT^*)} + \frac{G}{\exp(HT^*)} \quad (\text{A-2})$$

where

A=1.060636, B=0.15610,

C=0.19300, D=0.47635,

E=1.03587, F=1.52996,

$$G=1.76474, \quad H=3.89411,$$

The dimensionless temperature  $T^*$  is defined by

$$T^* = \frac{T}{\sqrt{\frac{\epsilon_A}{k_B}} \sqrt{\frac{\epsilon_B}{k_B}}} \quad (\text{A-3})$$

where

$k_B$ : Boltzmann constant ( $J/K$ )

$\epsilon_i$  : the characteristic Lennard-Jones energy ( $J$ )

<i>Pressure</i>	<i>MW<sub>N2</sub></i>	<i>MW<sub>O2</sub></i>	<i>σ<sub>N2</sub></i>	<i>σ<sub>O2</sub></i>	<i>ε<sub>N2</sub>/k<sub>B</sub></i>	<i>ε<sub>O2</sub>/k<sub>B</sub></i>
1 atm	28.0 g/mol	32.0 g/mol	3.8 Å	3.5 Å	71.4 K	106.7 K

With the constants of table calculated diffusion coefficient of oxygen in air

Temperature	873K	973K	1073K
D (m <sup>2</sup> /s)	1.27e-4	1.52e-4	1.78e-4

## APPENDIX B

### UMAT CODE (600°C)

C-----

C     Variables, as per ABAQUS User's Manual, V6.5:

C     STRESS: Array passed in as stress tensor at beginning of increment

C     STATEV: Array containing the solution dependent state variables

C     DDSDDDE: Jacobian matrix of constitutive model

C     DDSDDT: Variation of stress increment w.r.t temp.

C     DRPLDE: Variation

C     STRAN(NTENS): Array containing total strain components at beginning of increment

C     DSTRAN(NTENS): Array of strain increments

C     TIME(1): Value of step time at beginning of current increment

C     TIME(2): Value of total time at beginning of current increment

C     DTIME: Time increment

C     CMNAME: Name given on \*MATERIAL option

C     NSTATV: No. of soln. state vars. associated w/ this material

C     NPROPS: No. of material constants (given in \*USER MATERIAL)

C     PROPS(NPROPS): Array of material constants

C     COORDS(3): Array containing the current coords. of this point

C     DROTS(3,3): Rotation increment matrix

C     NOEL: Element no.

C     KSTEP: Step number

C     KINC: Increment number

C     TEMP: Temperature

C-----

\*USER SUBROUTINES

SUBROUTINE UMAT(STRESS,STATEV,DDSDDDE,SSE,SPD,SCD,  
1 RPL,DDSDDT,DRPLDE,DRPLDT,

```

2 STRAN,DSTRAN,TIME,DTIME,TEMP,DTEMP,PRED,DPRED,CMNAME,
3 NDI,NSHR,NTENS,NSTATEV,PROPS,NPROPS,COORDS,DROT,PNEWDT,
4 CELENT,DFGRD0,DFGRD1,NOEL,NPT,LAYER,KSPT,KSTEP,KINC)

```

C

```
C    INCLUDE 'ABA_PARAM.INC'
```

C

```
IMPLICIT REAL*8(A-M,O-Z)
```

```
    CHARACTER*8 CMNAME
```

```
    DIMENSION STRESS(NTENS),STATEV(NSTATEV),
```

```
1 DDSDD(NTENS,NTENS),DDSDDT(NTENS),DRPLDE(NTENS),
```

```
2 STRAN(NTENS),DSTRAN(NTENS),TIME(2),PRED(1),DPRED(1),
```

```
3 PROPS(NPROPS),COORDS(3),DROT(3,3),DFGRD0(3,3),DFGRD1(3,3)
```

C

```
PARAMETER (ONE=1.0D0, TWO=2.0D0)
```

```
    exp2=2.718281828
```

```
t_all=TIME(2)
```

```
    H=PROPS(1)
```

```
    ANU=PROPS(2)
```

```
    k1=1.52
```

```
    a1=0.0973
```

```
    b1=0.0000168
```

```
    a2=0.0619
```

```
    b2=0.0000252
```

```
    a3=0.0326
```

```
    b3=0.0000368
```

```
    a4=0.0117
```

```
    b4=0.0000584
```

```
    a5=0.00227
```

```
    b5=0.00009
```

```

c1=1.543/100000000
a0=0.0002
m=1723055.58368817
C -----
C   verification of time dependent input of E
C   write(*,*) E,t_all
C -----
C   Parameters for element identifications
C   If (noel.gt.1. .and. noel.le.10000.) then
C     If (t_all.le.12100.) then
C       E=k1*H*(m**3*(0.91*(a0-c1*a1/b1*(exp2**(t_all*b1)-1))))**2)**2
C     else if (t_all.gt.12100.) then
C       E=0.00000000000000000001
C     end if
C   else If (noel.gt.10001. .and. noel.le.20000.) then
C     If (t_all.le.16900.) then
C       E=k1*H*(m**3*(0.91*(a0-c1*a2/b2*(exp2**(t_all*b2)-1))))**2)**2
C     else if (t_all.gt.16900.) then
C       E=0.00000000000000000001
C     end if
C   else If (noel.gt.20001. .and. noel.le.30000.) then
C     If (t_all.le.24500.) then
C       E=k1*H*(m**3*(0.91*(a0-c1*a3/b3*(exp2**(t_all*b3)-1))))**2)**2
C       else if (t_all.gt.24500.) then
C         E=0.00000000000000000001
C       end if
C   else If (noel.gt.30001. .and. noel.le.40000.) then
C     If (t_all.le.34500.) then
C       E=k1*H*(m**3*(0.91*(a0-c1*a4/b4*(exp2**(t_all*b4)-1))))**2)**2

```

```

else if (t_all.gt.34500.) then
E=0.000000000000000001
end if
else If (noel.gt.40001 .and. noel.le.50000.) then
If (t_all.le.43610.) then
E=k1*H*(m*3*(0.91*(a0-c1*a5/b5*(exp2**(t_all*b5)-1))))**2)**2
else if (t_all.gt.43610.) then
E=0.000000000000000001
end if
end if

```

C -----

```

C      define the material matrix DDSDDDE
ALAMDA=ANU*E/(ONE+ANU)/(ONE-TWO*ANU)
AMU=E/TWO/(ONE+ANU)
DO I=1,NTENS
DO J=1,NTENS
DDSDDE(I,J)=0.0D0
ENDDO
ENDDO
DDSDDE(1,1)=ALAMDA+TWO*AMU
DDSDDE(2,2)=DDSDDE(1,1)
DDSDDE(3,3)=DDSDDE(1,1)
DDSDDE(4,4)=AMU
DDSDDE(5,5)=AMU
DDSDDE(6,6)=AMU
DDSDDE(1,2)=ALAMDA
DDSDDE(1,3)=ALAMDA
DDSDDE(2,3)=ALAMDA
DDSDDE(2,1)=DDSDDE(1,2)

```

```

      DDSDDDE(3,1)=DDSDDE(1,3)
      DDSDDDE(3,2)=DDSDDE(2,3)
C      write(*,*) DDSDDDE(2,2), DDSDDDE(1,1)
C      -----
C      Update the stress and incremental stress with the modified material matrix
      DO I=1,NTENS
        DO J=1,NTENS
          STRESS(I)=STRESS(I)+DDSDDE(I,J)*DSTRAN(J)
        ENDDO
C      write(*,*) stress(2), DDSDDDE(2,2)
      ENDDO
      RETURN
      END

```

## VITA

Seung Min Lee received his Bachelor of Science degree in architectural engineering from Korea Military Academy (KMA) in March 1996. After serving in military as a platoon leader and company commander, he worked with Professor Dai Gil Lee on the experimental and computational analysis of composite structures (composite toecap, composite hemispherical bearing on heavy duty vehicles) in Korea Advanced Institute of Science and Technology (KAIST). After receiving his Master of Science degree in mechanical engineering in February 2005, he joined Division of Ammunition Resupply Vehicle Development in Force Development Management Group ROK Army Headquarters.

He began his doctoral research with Professor Ochoa at Texas A&M University in September 2007 on the experimental and computational assessment on oxidation of carbon foam and received his Ph.D. in mechanical engineering in May 2010.

Seung Min Lee can be reached at min7375@gmail.com or through Dr. Ozden O. Ochoa, Department of Mechanical Engineering, Texas A&M University, College Station, TX 77843-3123.